



Numerical simulation of shallow water equations and related models

Harry Putu Gunawan

► To cite this version:

Harry Putu Gunawan. Numerical simulation of shallow water equations and related models. General Mathematics [math.GM]. Université Paris-Est, 2015. English. NNT: 2015PEST1010 . tel-01216642v2

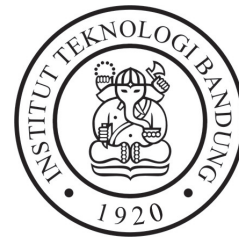
HAL Id: tel-01216642

<https://theses.hal.science/tel-01216642v2>

Submitted on 10 Feb 2016

HAL is a multi-disciplinary open access archive for the deposit and dissemination of scientific research documents, whether they are published or not. The documents may come from teaching and research institutions in France or abroad, or from public or private research centers.

L'archive ouverte pluridisciplinaire **HAL**, est destinée au dépôt et à la diffusion de documents scientifiques de niveau recherche, publiés ou non, émanant des établissements d'enseignement et de recherche français ou étrangers, des laboratoires publics ou privés.



THÈSE

Présentée pour obtenir le grade de

DOCTEUR de
L'Université Paris-Est

École doctorale :MSTIC

MATHÉMATIQUES APPLIQUÉES
Par

Putu Harry Gunawan

THESIS

Presented for the degree of

DOCTOR of
Institut Teknologi Bandung

Faculty: FMIPA

APPLIED MATHEMATICS
By

Numerical simulation of shallow water equations and related models

MEMBER OF COMMITTEE:

M. Robert EYMARD	Director of thesis I	UPEM
Mme. Sri Redjeki PUDJAPRASETYA	Director of thesis I	ITB
M. Wono Setya BUDHI	Director of thesis II	ITB
M. François BOUCHUT	Examiner	UPEM
M. David DOYEN	Examiner	UPEM
Mme. Edwige GODLEWSKI	Examiner & Reviewer	UPMC
M. Leo Hari WIRYANTO	Examiner & Reviewer	ITB
M. Sudi MUNGKASI	Examiner & Reviewer	Sanata Dharma University

Date of defense: 29 January 2015

UNIVERSITÉ
— PARIS-EST

THÈSE
présentée pour obtenir le grade de
DOCTEUR DE
L'Université Paris-Est
École doctorale :MSTIC

MATHÉMATIQUES APPLIQUÉES

PAR :

Putu Harry Gunawan

**Numerical simulation of shallow
water equations and related models**

MEMBER OF COMMITTEE:

M. Robert EYMARD	Director of thesis I	UPEM
Mme. Sri Redjeki PUDJAPRASETYA	Director of thesis I	ITB
M. Wono Setya BUDHI	Director of thesis II	ITB
M. François BOUCHUT	Examiner	UPEM
M. David DOYEN	Examiner	UPEM
Mme. Edwige GODLEWSKI	Examiner & Reviewer	UPMC
M. Leo Hari WIRYANTO	Examiner & Reviewer	ITB
M. Sudi MUNGKASI	Examiner & Reviewer	Sanata Dharma University

Date de soutenance : 29 January 2015

Numerical simulation of shallow water equations and related models

THESIS

Submitted to Institut Teknologi Bandung and L'Université Paris-Est

in fulfilment of the requirements double degree program

for the degree of

DOCTOR

BY :

Putu Harry Gunawan

NIM: 30111002

Department of Mathematics

SUPERVISORS:

Prof. Sri Redjeki PUDJAPRASETYA	Director of thesis I	ITB
Prof. Robert EYMARD	Director of thesis I	UPEM
Prof. Wono Setya BUDHI	Director of thesis II	ITB



INSTITUT TEKNOLOGI BANDUNG

2015

Acknowledgements

Foremost, I would like to express my sincere gratitude to my supervisors Prof. Robert Eymard, Prof. Sri Redjeki Pudjaprasetya and Prof. Wono Setya Budhi for the continuous support of my Ph.D study and research, for their patience, motivation, enthusiasm, and immense knowledge. their guidance helped me in all the time of research and writing of this thesis. I could not have imagined having good supervisors and mentors for my Ph.D study in double degree program between Institut Teknologi Bandung, Indonesia and Université Paris-est, France.

Besides my supervisors, I would like to thank the rest of my thesis committee: Prof. François Bouchut, Prof. Edwidge Godlewski, Prof. Leo Hari Wiryanto, Dr. David Doyen, and Dr. Sudi Mungkasi, for their encouragement, insightful comments, and hard questions. Moreover I would like to thanks to the chairman of the defense Prof. Janson Naiborhu and also as the chairman of study program of Mathematics ITB.

Also my special thanks goes to Dr. David Doyen as a mentor, for his patience, motivation, enthusiasm, and immense knowledge when we were working together in Paris-est. I am very lucky have a good mentor for my Ph.D study. I hope that further we can working together not only as a mentor but also as a good friend.

I thank my fellow labmates in LAMA Group: Xavier Lhébrard, for the stimulating discussions and tennis mentor, Pierre Feron, for all the fun we have had in lab (Watching tennis and singing PINK song's), and the others Sebastian Donoso, Paolo P, Pierre Y, Bertrand Cloez (with his wife Sanae El Mdaghri), Ali, Arnaoud, and our three beautiful angels (Marwa B, Marie-Noémie, Rania Z) for their friendship and their warmth. Moreover I would like to say thanks for their help when I was have some troubles with administration: to Mme. Sylvie Cach, Mme. Christiane Lafargue, and Mme. Audrey Patout.

My thanks also goes to my fellow labmates in ITB: for Anaconda room, Dr. Sitompul, Mr. Eric, Mr. Taufan, Mr. Jafar, Mr. Dadang. For the others: Lena, Mr. Cece, Mr. Kabil, Mr. Firman, Novry, Mr. Sugih, Mme Kasbah and etc. And also I would like to say thanks for my friends from DDIP program: Mme Yuly, Mme Ummy, Yudish, Narita, Christian, Seramika, and Mme Hesti. Additionally, I would like to say to DIKTI (Ministry of Higher Education of Indonesia) and BGF (Bourse de Gouvernement Francaise) for the financial support.

Last but not the least, I would like to thank my family: my big family, my mother Luh Wandri, my father I Gede Sujana, and my brothers Made Krisna Harryadi, Nyoman Roby Manik Saputra dan Ketut Tommy Suhari. I believe that from their support, I can finish my Ph.D study on time.

Contents

Resumé	vii
Abstract	ix
Abstrak	xi
General introduction	xiii
0.1 Motivation	xiii
0.2 Purpose	xv
0.3 Outline and contributions	xvii
I Staggered grid scheme for shallow water equations	1
1 An explicit staggered finite volume scheme for the shallow water equations	3
1.1 Introduction	3
1.2 Description of the upwind staggered scheme	5
1.2.1 One-dimensional scheme	5
1.2.2 Two-dimensional scheme	8
1.2.3 Second-order accurate schemes	11
1.2.4 Friction term	12
1.3 Consistency with the entropy inequality	13
1.3.1 Entropy	13
1.3.2 Semi-discrete entropy balance	14
1.3.3 Discrete balances	16
1.3.4 Consistency theorem	18
1.4 Standard numerical tests	20
1.4.1 Accuracy test	21
1.4.2 Dam break on a wet bed	22

1.4.3	Transcritical flow	24
1.4.4	Oscillations in a parabola	25
1.4.5	Dam break on dry bed with friction	26
1.4.6	Vacuum occurrence over a discontinuous topography	27
1.4.7	The steady state at rest	27
1.4.8	Oscillations in a paraboloid	29
1.5	Conclusion	31
2	Staggered conservative scheme for rotating shallow water equations on geostrophic flows	33
2.1	Introduction	33
2.2	Staggered conservative scheme for 2D rotating SWE	35
2.2.1	Motion under Coriolis force	36
2.2.2	Staggered conservative scheme	37
2.3	Numerical implementations	39
2.3.1	Rossby wave	40
2.3.2	Oscillation in a radially-symmetric paraboloid	41
2.3.3	Coastal Kelvin wave	43
2.3.4	Equatorial Kelvin waves	45
2.4	Conclusion	49
3	Numerical study of staggered scheme for viscous Saint-Venant equa- tions	51
3.1	Introduction	51
3.2	Numerical scheme	52
3.3	Numerical tests	53
3.3.1	Dam-break on a wet bed	53
3.3.2	Dam-break on a dry bed	56
3.4	Conclusion	58
II	Related Models	59
4	Explicit staggered grid scheme for the Exner - shallow water equa- tions	61
4.1	Introduction	61

4.2	The Exner - shallow water model	63
4.3	Description of the numerical schemes	65
4.3.1	1D staggered finite volume scheme	65
4.4	Numerical tests	67
4.4.1	Analytical solution	67
4.4.2	One-dimensional erodible dam break	69
4.4.3	Subcritical steady state over a moveable bump	73
4.4.4	Transcritical flow over a granular bump	73
4.5	Conclusion	75
5	Shear shallow water flows model by Richard-Gavrilyuk Model	77
5.1	Introduction	77
5.2	Mathematical analysis of the model	79
5.3	Numerical scheme	81
5.3.1	Suliciu/HLLC solver for the conservative part	83
5.4	Numerical simulations	84
5.4.1	Dam break	84
5.4.2	Transcritical flow	88
5.4.3	Roll waves	90
5.4.4	Runup of solitary wave	100
5.5	Conclusion	107
Summary and perspective	109	
III Appendixes	111	
A Appendix A	113	
Appendix A	113	
A.1	Analytical solution	113
A.1.1	Dam break	113
A.1.2	Oscillation in Paraboloid	115
B Appendix B	117	

Appendix B	117
B.1 Consistency of the scheme	120
B.1.1 Mass balance Equation	121
B.1.2 Momentum balance equations	122
B.2 Consistency of the Entropy balance	126
Bibliography	133

Resumé

Cette thèse porte sur l'approximation numérique des équations de Saint-Venant et de quelques problèmes qui leur sont reliés.

Dans la première partie, nous analysons les propriétés mathématiques et les applications des schémas numériques sur grilles décalées. La robustesse de ces schémas est prouvée sur des applications telles que les équations de Saint-Venant dans un domaine en rotation, en vue des écoulements géostrophiques, ainsi que l'extension de ces équations au cas visqueux.

Dans la seconde partie, nous présentons des modèles basés sur les équations de Saint-Venant. Nous commençons par étudier le couplage avec l'équation d'Exner, qui porte sur le transport des sédiments. Nous observons des propriétés de convergence numérique vers la solution exacte dans un cas de solution analytique, et nous constatons un bon accord avec des données expérimentales dans le cas de la rupture de barrage avec fond érodable. Nous continuons par l'étude d'un schéma numérique, basé sur une méthode de volumes finis colocalisés (HLLC) pour l'approximation du modèle de Richard-Gavrilyuk. Ce modèle étend les équations de Saint-Venant au cas des écoulements avec cisaillement. Des tests numériques montrent la validité du schéma.

Mots-clé : *équation de Saint-Venant avec topographie, frottement, volumes finis, grilles décalées, bilan d'entropie, équation d'Exner, modèle de Richard-Gavrilyuk.*

RESUMÉ

Abstract

This thesis is devoted to the numerical approximation of the shallow water equations and of some related models.

In the first part, we analyze the mathematical properties and the applications of the staggered grid scheme. The robustness of this scheme is validated on various applications such as the rotating shallow water equations for geostrophic flows model and viscous shallow water equations.

In the second part, we consider some related models. Firstly focusing on the coupling between the Exner equation and the shallow water equations, modelling bedload sediment transport, we observe in a particular case the numerical convergence of the scheme to the exact solution, as well as a good agreement with the experimental data in the dam-break with erodible bottom test. Secondly, we present a numerical scheme based on the finite volume collocated scheme (HLLC) in order to approximate the Richard-Gavrilyuk model. This model is an extension of the shallow water model, fit for modelling the shear shallow water flows. Some numerical tests provide a validation of the scheme.

Keywords: *shallow water equations with topography, friction, finite volumes, staggered grids, entropy balance, Exner equation, Richard-Gavrilyuk model.*

ABSTRACT

Abstrak

Tujuan dari tesis ini adalah untuk mempelajari skema numerik untuk *shallow water equations* (persamaan air dangkal) dan model terkait.

Bagian pertama, kita mempelajari analisis dari properti matematika skema staggered grid beserta aplikasinya. Beberapa standar tes numerik menunjukkan kehandalan (robustness) dari skema tersebut. Sebagai tambahan, skema staggered juga ditunjukkan sebagai skema yang simpel dan mudah untuk beberapa aplikasi seperti rotating shallow water equations untuk model geostrophic flows dan viscous shallow water equations.

Pada bagian kedua, kita tinjau pemodelan terkait terhadap standard shallow water equations. Pertama kita fokuskan terhadap model gabung persamaan Exner dan shallow water, yang merupakan model untuk bedload sediment transport. Laju dari konvergensi skema numerik terhadap solusi eksak diperlihatkan sangat terpenuhi. Dan selain itu, perbandingan hasil skema numerik terhadap data eksperimen pada tes dam-break dengan dasar bergerak menunjukkan hasil yang sangat baik. Kedua, disini kita mencoba membangun sebuah skema numerik berdasarkan collocated grid volume berhingga dengan menggunakan HLLC (Harten-Lax-van Leer-Contact) solver untuk menghampiri model Richard-Gavrilyuk. Model ini merupakan pengembangan dari shallow water flow dengan beberapa tambahan variabel. Model ini sangat tepat untuk memodelkan aliran shear shallow water. Beberapa tes numerik ditunjukkan untuk memvalidasi kekuatan dari skema numerik.

Kata kunci: *persamaan air dangkal beserta topografi, friksi, volume hingga, staggered grids, entropy balance, persamaan Exner, model Richard-Gavrilyuk.*

ABSTRAK

General introduction

In this introductory chapter, we present motivation, purpose, outline and contributions.

0.1 Motivation

The shallow water equations (also called Saint-Venant's equations) are the usual model to describe fluid flow in the rivers, channels, estuaries or coastal areas. Apart from the application in shallow water areas, they are also used to describe oceanic or atmospheric circulation or debris flows. In oceanic phenomena this model is commonly adopted for simulating tsunami.

The main assumption of the shallow water model is that the horizontal length scale is much greater than the depth scale. Thus, one can get rid of the vertical dimension by averaging the mass and momentum conservation equations over the depth. In one dimension of space, the shallow water equations read

$$\partial_t h + \partial_x(hu) = 0, \quad (1)$$

$$\partial_t(hu) + \partial_x \left(hu^2 + 1/2gh^2 \right) + gh\partial_x z = 0, \quad (2)$$

where h is the water height, u is the velocity, g is the gravitational constant, and z is the topography of the bottom (see Figure 1).

The shallow water equations (1-2) are a nonlinear hyperbolic system of conservation laws (with a source term due to the topography). For such a problem, where shocks can form in the solution, finite volume methods have proved to be very effective. In this method, two approaches are classically available. Generally in the collocated approach, all the unknowns of the system are approximated on the same mesh and the numerical fluxes are computed with an approximate Riemann solver (see [3, 7, 45, 30] for description this method). However, this method is not straightforward and not easy to implement. For instance, the computation of the solution with data vacuum is still difficult. The problem occurs when two values

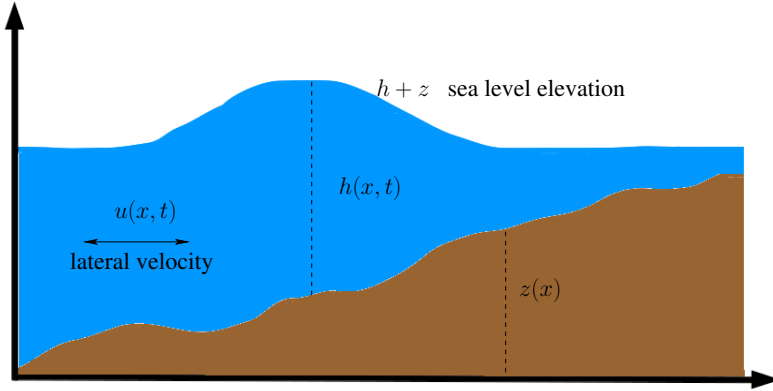


Figure 1: One-dimensional shallow water model.

which are zero and nonzero are given, then the timestep tends to 0 restricted by the Courant-Friedrichs-Levy (CFL) condition (see F. Bouchut [7] for more detail). In order to cure this defect, F. Bouchut [7] proposed a numerical flux which is called Suliciu relaxation adapted to vacuum. This numerical flux has a property which is proved a positive entropy satisfying approximate Riemann solver for shallow water equation that handle the vacuum. But again, we can say that the property is not easy to get and is complicated. Moreover, as recorded in [41], the extension to 3D model for collocated method is not simple at all.

In contrast to the collocated method, staggered finite volume discretizations for solving nonlinear hyperbolic system of conservation laws have been investigated in the past few years [1, 41, 42, 35]. Here, the staggered approach the different unknowns of the system are approximated on staggered meshes. The numerical fluxes can then be computed in a simpler way, avoiding the use of an approximate Riemann solver. Note that staggered discretizations have been used for a long time for systems of partial differential equations such as the Maxwell equations, the Navier-Stokes equations or the nonconservative shallow water equations [1]. Seemingly, the staggered finite volume method is similar to finite difference method. However as recorded in [35], the staggered scheme approximates the conservation equation in discrete form on a fixed cell (control volume), meanwhile in finite difference methods, the derivatives at a point are approximated by truncated Taylor series.

Generally, a robust and well-balanced scheme for shallow water equations should satisfy some mathematical properties such as preserve the nonnegativity of water height h , well-balanced, i.e. it preserves the discrete steady state, consistent with the

shallow water equations and satisfy a discrete entropy inequality. A complete stability and convergence analysis of a finite volume scheme for a nonlinear hyperbolic system is out of reach. However, a number of properties of the scheme related to the stability and the convergence can be studied: preservation of invariant domains, entropy inequalities, preservation of some particular steady states (well-balanced property). Unfortunately, the literatures to study the staggered finite volume method for shallow water equations satisfy those properties are limited. Particularly, the study of staggered finite volume method in entropy satisfying is not available. Therefore through this thesis, we will try to investigate, design and analyze such properties of a staggered finite volume scheme for the shallow water equations with topography.

0.2 Purpose

The aims of this thesis are:

1. to design and analyze a staggered finite volume scheme for the shallow water equations with topography,
2. to show and simulate the applicability of staggered finite volume scheme to various flow phenomena in one and two dimensions,
3. to elaborate and study the staggered or collocated finite volume scheme for the related models of shallow water equations, the coupled system Exner-shallow water equations and the Richard-Gavrilyuk model.

In the first aim, we design one and two dimensional staggered finite volume discretizations on first and second-order accuracy in space and time. In one dimensional case, we study a number of properties of the staggered scheme related to the stability and the convergence such as, the positivity of water height h , well-balanced property, and satisfying entropy inequality. Our goal here that we prove the staggered scheme satisfy certain entropy inequality to obtain the stability and convergence towards correct solution. In this case, the relevant entropy refers to the accumulation energy of solution [46]. Here, first we establish an entropy balance for a semi-discrete version of the staggered scheme. It appears that the entropy decreases with time. Then, we establish an entropy balance for the fully discrete scheme. The explicit time discretization introduces some entropy production terms in the balance so that

GENERAL INTRODUCTION

the entropy does not necessarily decreases at each time step. However, by passing to the limit in the discrete entropy balance, we are able to prove that the scheme is consistent with the global entropy inequality. The proof of mathematical properties of the staggered scheme for shallow water equations above are analogous to those for the barotropic Euler equations, as recorded in [26, 32]. The only difference is the presence of topography terms in the discrete momentum equation and the discrete entropy balance. Moreover, the robustness and the accuracy of the scheme will also be assessed through various test-cases: dam break on a wet bed, oscillations in a parabola, transcritical flow with shock, dam break on a dry bed with friction, vacuum occurrence over a discontinuous topography.

Due to robustness of the staggered finite volume scheme in first aim, in the second aim we study the two-dimensional staggered scheme for rotating shallow water equations on geostrophic flows and the one-dimensional staggered scheme for viscous shallow water or Saint-Venant equations (SVE) derived by Gerbeau and Perthame [23]. The resulting scheme is implemented for simulating various rotating phenomena, such as, Rossby wave, oscillation in a paraboloid, coastal and equatorial Kelvin waves. In viscous shallow water equations, some comparison results from other schemes are elaborated in dam-break problem. They show a good agreement with results calculated using kinetic scheme and direct Navier-Stokes approach.

In the third aim, we study the staggered and collocated numerical scheme for related models of shallow water equations. The first related model is a coupled system of the Exner - shallow water equations for bedload sediment modelling by [4, 11]. Here, we design and implement the staggered grid scheme for this coupled system. Some numerical tests show good convergence properties to an analytical solution and match pretty well experimental data in the case of dam break with erodible bottom. The cases of subcritical steady flow over a bump and transcritical flow over a bump are presented, showing the robustness of the scheme. The second related model is the Richard-Gavrilyuk model for studying the shear shallow water modelling which has been proposed recently by G. Richard and S. Gavrilyuk [38, 37]. The shear shallow water model provides a more realistic description of some flow phenomena, such as the classical hydraulic jump or the roll waves. Formally, this model is similar to the full gas dynamics system. But, this model can be considered as an extension of the standard shallow water model, involving some additional unknowns, the roller enstrophy Φ , and two additional parameters, the wall enstrophy

ϕ_0 and the roller drag coefficient C_r . For Richard-Gavrilyuk model, we implement the collocated method, since staggered scheme is not straightforward. Here we propose the collocated scheme with HLLC (Harten-Lax-van Leer-Contact) solver by [7]. And we present various numerical simulations of Richard-Gavrilyuk model together with those calculated using standard shallow water equations model. For the case of dam-break, the Richard-Gavrilyuk model show more relevant results physically.

0.3 Outline and contributions

The contents of this thesis are organized into two parts and five chapters. Some of the chapters are based on articles which are published or submitted:

1. Chapter 1: It has been published in proceeding as: D. Doyen and P. H. Gunawan. *"An Explicit Staggered Finite Volume Scheme for the Shallow Water Equations"*. In: Finite Volumes for Complex Applications VII-Methods and Theoretical Aspects. Springer, 2014, pp. 227–235. doi: 10.1007/978-3-319-05684-5_21.
2. Chapter 2: It has been submitted as: P. H. Gunawan and S. R. Pudjaprasetya. *"Staggered conservative scheme for rotating shallow water equations on geostrophic flows"*, 2014.
3. Chapter 3: It has been published as: Putu Harry Gunawan. *"Numerical study of staggered scheme for viscous Saint-Venant equations"*. In: Applied Mathematical Sciences, Vol. 8, 2014, no. 108, 5349-5359, <http://dx.doi.org/10.12988/ams.2014.47580>.
4. Chapter 4: It has been submitted as: P. H. Gunawan, R. Eymard and S. R. Pudjaprasetya. *"Explicit staggered grid scheme for the Exner - shallow water equations"*, 2014.

Part I is about the explicit staggered grid finite volume scheme for shallow water equations. This part consists of three chapters discussing analysis and application aspects of the scheme in one- and two-dimensional cases.

In Chapter 1, the design and analysis of the explicit staggered finite volume scheme for shallow water equations with topography are introduced. A number of

properties of the scheme related to the stability and the convergence have been studied: preservation of invariant domains, entropy inequalities, preservation of some particular steady states (well-balanced property). Moreover, the robustness and the accuracy of the scheme will also be assessed through various test-cases: dam break with non-flat topography, lake oscillations, etc.

In Chapter 2, the application for rotating shallow water equations on geostrophic flows are given. The two-dimensional full model of shallow water equations including Coriolis force as the source term are considered. Formulation in conservative forms are as follows

$$\partial_t h + \partial_x(hu) + \partial_y(hv) = 0, \quad (3)$$

$$\partial_t(hu) + \partial_x\left(hu^2 + \frac{1}{2}gh^2\right) + \partial_y(huv) + gh\partial_x z - fhv = 0, \quad (4)$$

$$\partial_t(hv) + \partial_x(huv) + \partial_y\left(hv^2 + \frac{1}{2}gh^2\right) + gh\partial_y z + fhu = 0, \quad (5)$$

where u, v are the fluid particle velocities in $x-$ and $y-$ directions, respectively and f the Coriolis parameter. Approximation of the momentum balances are calculated by means of splitting, meaning that first we solve the equations without Coriolis terms. Then, the next step is correction to account for the Coriolis terms. Here, the Coriolis terms is calculated using the Crank-Nicolson method.

In Chapter 3, the staggered grid scheme for viscous Saint-Venant equations is presented. The equations of one-dimensional viscous SVE are given as

$$\partial_t h + \partial_x(hu) = 0, \quad (6)$$

$$\partial_t(hu) + \partial_x\left(hu^2 + \frac{1}{2}gh^2\right) + gh\partial_x z = -\kappa_{vsv}(h)u + 4\mu\partial_x(h\partial_x u), \quad (7)$$

$$\kappa_{vsv}(h) = \frac{\kappa}{1 + \frac{\kappa h}{3\mu}}, \quad (8)$$

where the constants κ and μ are the friction and viscosity coefficients respectively. Some comparison results with other schemes are elaborated in dam-break test case. They show a good agreement with results from kinetic scheme and direct Navier-Stokes approach.

Part II discusses the related models of shallow water equations, such as the coupled system Exner-shallow water equations and the Richard-Gavrilyuk model.

In Chapter 4, the staggered numerical scheme is shown to be directly applicable and simple for approximating the Exner - shallow water equations, for bedload sediment modelling. The coupled shallow water – Exner equations are given in the one dimensional case by

$$\partial_t h + \partial_x(hu) = 0, \quad (9)$$

$$\partial_t(hu) + \partial_x\left(hu^2 + \frac{1}{2}gh^2\right) + gh\partial_x(z - H) + ghS_f = 0, \quad (10)$$

$$\partial_t z + \xi\partial_x Q_s = 0, \quad (11)$$

where z is the bed elevation, Q_s the sediment discharge (or bedload) and H the depth of fixed bedrock layer to the reference level (see Figure 2). The coefficient ξ is computed by $\xi = (1 - \phi)^{-1}$, where ϕ is the bed sediment porosity. Moreover, the source term S_f , which is a friction term, depends on the type of flow.

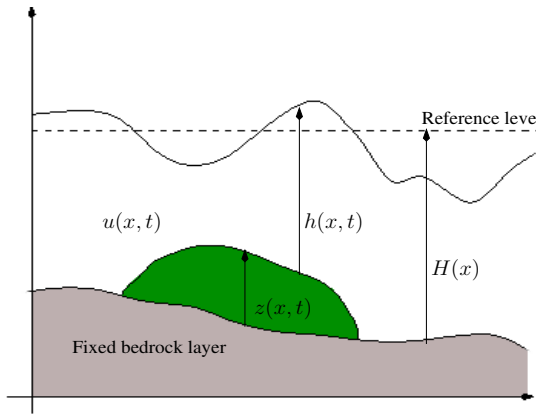


Figure 2: The one-dimensional sketch of shallow water with a sediment layer.

Numerical tests show good convergence properties to the analytical solution and match pretty well experimental data in the case of dam break with erodible bottom. The cases of subcritical steady flow over a bump and transcritical flow over a bump are presented, showing the robustness of the scheme.

Chapter 5 provides the Richard-Gavrilyuk model which is an extension of the standard shallow water model, involving an additional unknown, the roller enstrophy, and two additional parameters, the wall enstrophy and the roller drag coefficient. This model read as

$$\partial_t h + \partial_x(hu) = 0, \quad (12)$$

$$\partial_t(hu) + \partial_x(hu^2 + p) = -gh\partial_x z - C_f u|u|, \quad (13)$$

$$\partial_t(h(u^2/2 + e)) + \partial_x((h(u^2/2 + e) + p)u) = \left(-gh\partial_x z - \left(C_f + \frac{\Phi}{\phi_0 + \Phi} C_r \right) u|u| \right) u, \quad (14)$$

where

$$p = \frac{1}{2}gh^2 + (\phi_0 + \Phi)h^3, \quad (15)$$

$$e = \frac{1}{2}gh + \frac{1}{2}(\phi_0 + \Phi)h^2. \quad (16)$$

This model is suitable to describe shear flow phenomena. Hence, the numerical scheme to approximate the model is constructed and some applications are also presented. In the end of this thesis, the conclusion and perspectives are drawn.

PART I

Staggered grid scheme for shallow water equations

An explicit staggered finite volume scheme for the shallow water equations¹

We propose an explicit finite volume scheme for the shallow water equations. The different unknowns of the system are approximated on staggered meshes. The numerical fluxes are computed with upwind and centered discretizations. We prove a number of properties of the scheme: positivity preserving, well-balanced, consistent with the global entropy inequality. We compare it with collocated schemes, using approximate Riemann solvers, on various problems.

1.1 Introduction

The shallow water equations, or Saint-Venant's equations, are a usual model to describe fluid flow in rivers, channels, estuaries or coastal areas. The main assumption of the shallow water model is that the horizontal length scale is much greater than the depth scale. Thus, one can get rid of the vertical dimension by averaging the mass and momentum conservation equations over the depth. In the one-dimensional case, they read

$$\partial_t h + \partial_x(hu) = 0, \quad (1.1)$$

$$\partial_t(hu) + \partial_x \left(hu^2 + \frac{1}{2}gh^2 \right) + gh\partial_x z = 0, \quad (1.2)$$

¹This chapter has been published in proceeding as: D. Doyen and P. H. Gunawan. “An Explicit Staggered Finite Volume Scheme for the Shallow Water Equations”. In: Finite Volumes for Complex Applications VII-Methods and Theoretical Aspects. Springer, 2014, pp. 227–235. doi: 10.1007/978-3-319-05684-5_21.

CHAPTER 1

where t denotes the time variable, x denotes the space variable, h is the water height, u is the velocity, g is the gravitational constant, and z is the topography of the bottom.

The shallow water equations are a nonlinear hyperbolic system of conservation laws (with a source term due to the topography). For such a problem, where shocks can form in the solution, finite volume methods have proved to be very effective. Generally, all the unknowns of the system are approximated on the same mesh and the numerical fluxes are computed with an approximate Riemann solver. We refer to the monographs of F. Bouchut [7] and E. F. Toro [45] for a thorough description and analysis of this approach. Staggered finite volume discretizations for solving nonlinear hyperbolic system of conservation laws have been investigated more recently (see, e.g., [25, 26, 41]). In contrast to the collocated discretization described above, the different unknowns of the system are approximated on staggered meshes. The numerical fluxes can then be computed simply componentwise, using upwind or centered approximations.

In the present chapter, we propose an explicit staggered finite volume scheme for the shallow water equations. The scheme is identical to the one in [26] when the topography is flat. We prove a number of properties of the scheme: preservation of the water height positivity, preservation of some particular discrete steady states (well-balanced property), consistency with the entropy inequality. The preservation of the water height positivity is physically relevant and is crucial for the stability, the occurrence of negative quantities leading rapidly to the computation failure. We obtain this positivity for the staggered scheme under a CFL-like condition. The steady states of the shallow water equations are the states (h, u) such that $hu = cst$ and $\frac{1}{2}u^2 + g(h + z) = cst$. In particular, the steady states at rest, that is the steady states such that $u = 0$, satisfy $h+z = cst$. The preservation of these steady states at rest at the discrete level is important since many practical problems are perturbations of such states. With approximate Riemann solvers, this preservation is quite involved [7], whereas it is straightforward in the staggered framework (on uniform grids). The entropy η for the shallow water equations is the sum of the kinetic energy, the potential energy and a term stemming from the topography:

$$\eta(h, hu, z) := \frac{1}{2}hu^2 + \frac{1}{2}gh^2 + ghz. \quad (1.3)$$

The entropy inequality reads

$$\partial_t \eta(h, hu, z) + \partial_x G(h, hu, z) \leq 0, \quad (1.4)$$

where the entropy flux G is defined by

$$G(h, hu, z) := \left(\frac{1}{2} hu^2 + gh^2 + ghz \right) u \quad (1.5)$$

Note that the entropy inequality (1.4) holds for smooth and non-smooth solutions. However to accommodate the discontinuous solutions of h or u , the derivatives involved in the entropy inequality are considered in the weak sense. The staggered scheme does not satisfy a discrete entropy inequality. However, we prove that it is consistent with the global entropy inequality, which guarantees that the discontinuities computed by the scheme are admissible discontinuities.

Finally, we test the staggered scheme on various problems: accuracy test, dam break on a wet bed, oscillations in a parabola, transcritical flow with shock, dam break on a dry bed with friction, vacuum occurrence over a discontinuous topography, oscillations in a paraboloid.

The chapter is organized as follows. Section 1.2 describes the staggered scheme and its first properties. Section 1.3 presents the entropy consistency theorem and Section 4 the numerical tests. A brief comparison between the staggered and collocated schemes is made in conclusion.

1.2 Description of the upwind staggered scheme

1.2.1 One-dimensional scheme

We consider the one-dimensional shallow water equations (1.1)-(1.2) on the space domain $\Omega := (0, L)$ and the time interval $(0, T)$. Periodic boundary conditions are prescribed. The time interval is divided into N_t time steps of length Δt and, for all $n \in \{0, \dots, N_t\}$, $t^n := n\Delta t$. The domain Ω is divided into N_x cells of length Δx . The left end, the center and the right end of the i -th cell are denoted by $x_{i-\frac{1}{2}}$, x_i and $x_{i+\frac{1}{2}}$, respectively. The water height h and the topography z are discretized at the center of the cells, whereas the velocity u is discretized at the interfaces between the cells. The approximation of h at point x_i and at time t^n is denoted by h_i^n . The

CHAPTER 1

approximation of z at point x_i is denoted by z_i . The approximation of u at point $x_{i+\frac{1}{2}}$ and at time t^n is denoted by $u_{i+\frac{1}{2}}^n$. The space indices of the objects and quantities defined above must be understood modulo N_x (e.g. $u_{\frac{1}{2}}^n = u_{N_x+\frac{1}{2}}^n$ or $h_0^n = h_{N_x}^n$). This space discretization is represented in Figure 1.1. Let us set $\mathcal{M} := \{1, \dots, N_x\}$.

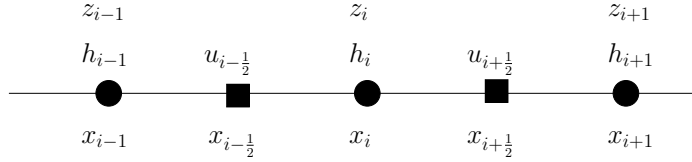


Figure 1.1: One-dimensional staggered grid.

The mass conservation equation is discretized with an explicit upwind scheme. For all $i \in \mathcal{M}$,

$$h_i^{n+1} - h_i^n + \frac{\Delta t}{\Delta x} (q_{i+\frac{1}{2}}^n - q_{i-\frac{1}{2}}^n) = 0, \quad (1.6)$$

where

$$q_{i+\frac{1}{2}}^n := \hat{h}_{i+\frac{1}{2}}^n u_{i+\frac{1}{2}}^n, \quad \hat{h}_{i+\frac{1}{2}}^n := \begin{cases} h_i^n & \text{if } u_{i+\frac{1}{2}}^n \geq 0 \\ h_{i+1}^n & \text{if } u_{i+\frac{1}{2}}^n < 0 \end{cases}. \quad (1.7)$$

The momentum balance equation is discretized with explicit upwind fluxes for the convection term and implicit centered fluxes for the pressure term and topography term. For all $i \in \mathcal{M}$,

$$\begin{aligned} h_{i+\frac{1}{2}}^{n+1} u_{i+\frac{1}{2}}^{n+1} - h_{i+\frac{1}{2}}^n u_{i+\frac{1}{2}}^n + \frac{\Delta t}{\Delta x} & \left[q_{i+1}^n \hat{u}_{i+1}^n - q_i^n \hat{u}_i^n + \frac{1}{2} g \left[(h_{i+1}^{n+1})^2 - (h_i^{n+1})^2 \right] \right. \\ & \left. + g h_{i+\frac{1}{2}}^{n+1} (z_{i+1} - z_i) \right] = 0, \end{aligned} \quad (1.8)$$

where

$$\begin{aligned} h_{i+\frac{1}{2}}^n &:= \frac{1}{2} (h_i^n + h_{i+1}^n), \\ q_i^n &:= \frac{1}{2} (q_{i-\frac{1}{2}}^n + q_{i+\frac{1}{2}}^n), \quad \hat{u}_i^n := \begin{cases} u_{i-\frac{1}{2}}^n & \text{if } q_i^n \geq 0 \\ u_{i+\frac{1}{2}}^n & \text{if } q_i^n < 0 \end{cases}. \end{aligned}$$

The computation of the discrete unknowns at each time step is completely explicit. First the discrete water heights $\{h_i^{n+1}\}$ are computed with (1.6), then the discrete velocities $\{u_{i+\frac{1}{2}}^{n+1}\}$ are computed with (1.8) (if $h_{i+\frac{1}{2}}^{n+1} = 0$, by convention, $u_{i+\frac{1}{2}}^{n+1}$ is set to zero). We see immediately that this scheme conserves the mass and, for a flat

CHAPTER 1

topography, the total momentum. It is easy to verify that the water height remains nonnegative at time t^{n+1} under the CFL-like condition

$$\Delta t \leq \frac{\Delta x}{(-u_{i-\frac{1}{2}}^n)^+ + (u_{i+\frac{1}{2}}^n)^+}, \quad \forall i \in \mathcal{M}, \quad (1.9)$$

where, for any $a \in \mathbb{R}$, $(a)^+ := \max(a, 0)$. At each time step, the Courant number is defined by

$$\nu := \frac{\Delta t}{\Delta x} \max_{i \in \mathcal{M}} \left(\frac{|q_{i+\frac{1}{2}}^n + q_{i-\frac{1}{2}}^n|}{2h_i^n} + \sqrt{gh_i^n} \right). \quad (1.10)$$

The numerical simulations show that the staggered scheme is stable under the CFL condition $\nu < 1$.

Lemma 1 (Steady states at rest). *Consider the discretization of shallow water equation using the explicit staggered numerical scheme (1.6-1.8). If $u_{i+\frac{1}{2}}^n = 0$ and $h_i^n + z_i = cst$ for all $i \in \{0, \dots, N\}$, then $u_{i+\frac{1}{2}}^{n+1} = 0$ and $h_i^{n+1} + z_i = cst$. Thus, the numerical scheme (1.6-1.8) is a well-balanced scheme i.e. preserves the steady states of a lake at rest.*

Proof. Let first look at in the discretization of mass balance (1.6). If $u_{i+\frac{1}{2}}^n = 0$ for all $i \in \{0, \dots, N\}$ we have,

$$h_i^{n+1} = h_i^n \quad \forall i \in \{0, \dots, N\}. \quad (1.11)$$

The topography z_i is not depend on time, and if $h_i^n + z_i = cst$, thus

$$h_i^{n+1} + z_i = h_i^n + z_i = cst \quad \forall i \in \{0, \dots, N\}. \quad (1.12)$$

Next, we look into the discretization of momentum balance (1.8). With $u_{i+\frac{1}{2}}^n = 0$ for all $i \in \{0, \dots, N\}$, we get

$$\begin{aligned} h_{i+\frac{1}{2}}^{n+1} u_{i+\frac{1}{2}}^{n+1} + \frac{\Delta t}{\Delta x} \left[\frac{1}{2} g \left[(h_{i+1}^{n+1})^2 - (h_i^{n+1})^2 \right] + gh_{i+\frac{1}{2}}^{n+1} (z_{i+1} - z_i) \right] &= 0, \\ h_{i+\frac{1}{2}}^{n+1} u_{i+\frac{1}{2}}^{n+1} + \frac{\Delta t}{\Delta x} \left(g \left[(h_{i+1}^{n+1} - h_i^{n+1}) \frac{(h_{i+1}^{n+1} + h_i^{n+1})}{2} \right] + gh_{i+\frac{1}{2}}^{n+1} (z_{i+1} - z_i) \right) &= 0, \end{aligned}$$

thanks to the definition of water height at the interface between the cells $h_{i+\frac{1}{2}}^{n+1} :=$

$(h_{i+1}^{n+1} + h_i^{n+1})/2$, then we have

$$\begin{aligned} \frac{(h_{i+1}^{n+1} + h_i^{n+1})}{2} u_{i+\frac{1}{2}}^{n+1} + \frac{g\Delta t}{\Delta x} \frac{(h_{i+1}^{n+1} + h_i^{n+1})}{2} \left((h_{i+1}^{n+1} - h_i^{n+1}) + (z_{i+1} - z_i) \right) &= 0, \\ u_{i+\frac{1}{2}}^{n+1} + \frac{g\Delta t}{\Delta x} \left((h_{i+1}^{n+1} + z_{i+1}) - (h_i^{n+1} + z_i) \right) &= 0. \end{aligned}$$

Since we have $h_i^{n+1} + z_i = cst$ for all $i \in \{0, \dots, N\}$ from (1.12), thus we get $u_{i+\frac{1}{2}}^{n+1} = 0$. Therefore the proof is done. \square

Remark 1.2.1. *It is essential to make an implicit discretization of the pressure term in (1.8). With an explicit discretization $[(h_{i+1}^n)^2 - (h_i^n)^2]$ instead of $[(h_{i+1}^{n+1})^2 - (h_i^{n+1})^2]$, the scheme would not be consistent with the entropy inequality. As a consequence, non-entropic shocks might occur in the numerical simulations (see Figure 1.6).*

1.2.2 Two-dimensional scheme

The two-dimensional shallow water equations read

$$\partial_t h + \partial_x(hu) + \partial_y(hv) = 0, \quad (1.13)$$

$$\partial_t(hu) + \partial_x \left(hu^2 + \frac{1}{2}gh^2 \right) + \partial_y(huv) + gh\partial_x z = 0, \quad (1.14)$$

$$\partial_t(hv) + \partial_x(huv) + \partial_y \left(hv^2 + \frac{1}{2}gh^2 \right) + gh\partial_y z = 0, \quad (1.15)$$

where t denotes the time variable, x and y denote the two Cartesian space coordinates, h is the water height, u is the velocity in the x -direction, v is the velocity in the y -direction, g is the gravitational constant, and z is the topography of the bottom.

We consider the two-dimensional shallow water equations on the rectangular space domain $\Omega := (0, L_x) \times (0, L_y)$ and the time interval $(0, T)$. Periodic boundary conditions are prescribed. The domain is meshed with a rectilinear grid of $N_x \times N_y$ cells. We set $\mathcal{M} := \{1, \dots, N_x\} \times \{1, \dots, N_y\}$. The cell of coordinates (i, j) is denoted by $K_{i,j}$. The center of the cell $K_{i,j}$ is denoted by $x_{i,j}$. The center of the bottom edge, top edge, left edge and right edge are denoted by $x_{i,j-\frac{1}{2}}$, $x_{i,j+\frac{1}{2}}$, $x_{i-\frac{1}{2},j}$ and $x_{i+\frac{1}{2},j}$, respectively. The water height h and the topography z are discretized at the center of the cells. The velocity in the x -direction is discretized at the center of the edges normal to the x -direction, while the velocity in the y -direction is discretized at the

CHAPTER 1

center of the edges normal to the y -direction. The approximation of h at point $x_{i,j}$ and at time t^n is denoted by $h_{i,j}^n$. The approximation of z at point $x_{i,j}$ is denoted by $z_{i,j}$. The approximation of u at point $x_{i+\frac{1}{2},j}$ and time t^n is denoted by $u_{i+\frac{1}{2},j}^n$, while the approximation of v at point $x_{i,j+\frac{1}{2}}$ and at time t^n is denoted by $v_{i,j+\frac{1}{2}}^n$. The space indices of the objects and quantities defined above must be understood modulo N_x for the first index and modulo N_y for the second index (e.g. $u_{\frac{1}{2},j}^n = u_{N_x+\frac{1}{2},j}^n$ or $h_{i,0}^n = h_{i,N_y}^n$). The staggered grid is represented in Figure 1.2.

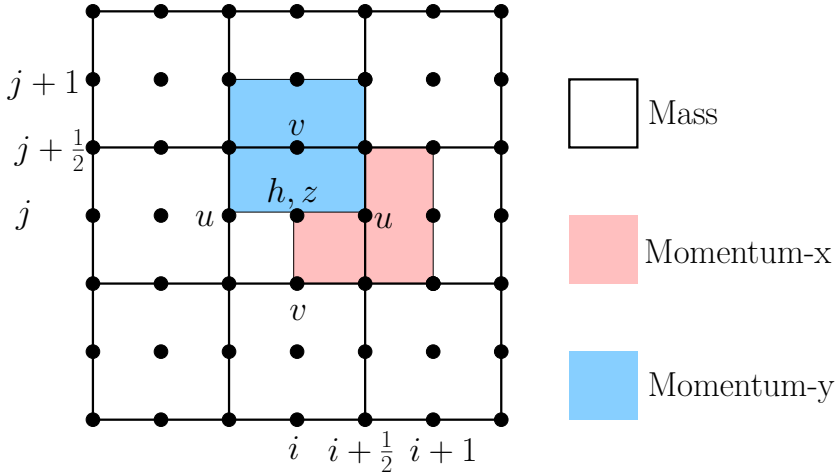


Figure 1.2: Two-dimensional (Arakawa C-grid). The white cell is represented the control volume of mass conservation, while the pink and the blue cells are represented the control volume of momentum balance in x and y -direction respectively.

Let us now describe the scheme at time t^{n+1} . The mass conservation equation (1.13) is discretized with an explicit upwind scheme. For all $(i, j) \in \mathcal{M}$,

$$h_{i,j}^{n+1} - h_{i,j}^n + \frac{\Delta t}{\Delta x} [p_{i+\frac{1}{2},j}^n - p_{i-\frac{1}{2},j}^n] + \frac{\Delta t}{\Delta y} [q_{i,j+\frac{1}{2}}^n - q_{i,j-\frac{1}{2}}^n] = 0, \quad (1.16)$$

where

$$p_{i+\frac{1}{2},j}^n = \hat{h}_{i+\frac{1}{2},j}^n u_{i+\frac{1}{2},j}^n, \quad \hat{h}_{i+\frac{1}{2},j}^n = \begin{cases} h_{i,j}^n & \text{if } u_{i+\frac{1}{2},j}^n \geq 0 \\ h_{i+1,j}^n & \text{if } u_{i+\frac{1}{2},j}^n < 0 \end{cases}, \quad (1.17)$$

$$q_{i,j+\frac{1}{2}}^n = \hat{h}_{i,j+\frac{1}{2}}^n v_{i,j+\frac{1}{2}}^n, \quad \hat{h}_{i,j+\frac{1}{2}}^n = \begin{cases} h_{i,j}^n & \text{if } v_{i,j+\frac{1}{2}}^n \geq 0 \\ h_{i,j+1}^n & \text{if } v_{i,j+\frac{1}{2}}^n < 0 \end{cases}. \quad (1.18)$$

The momentum balance equation in the x -direction (1.14) is discretized with explicit upwind fluxes for the convective terms and implicit centered fluxes for the pressure

term and topography term. For all $(i, j) \in \mathcal{M}$,

$$\begin{aligned} h_{i+\frac{1}{2},j}^{n+1} u_{i+\frac{1}{2},j}^{n+1} - h_{i+\frac{1}{2},j}^n u_{i+\frac{1}{2},j}^n + \frac{\Delta t}{\Delta y} & \left[q_{i+\frac{1}{2},j+\frac{1}{2}}^n \hat{u}_{i+\frac{1}{2},j+\frac{1}{2}}^n - q_{i+\frac{1}{2},j-\frac{1}{2}}^n \hat{u}_{i+\frac{1}{2},j-\frac{1}{2}}^n \right] \\ & + \frac{\Delta t}{\Delta x} \left[(p_{i+1,j}^n \hat{u}_{i+1,j}^n - p_{i,j}^n \hat{u}_{i,j}^n) + \frac{1}{2} g((h_{i+1,j}^{n+1})^2 - (h_{i,j}^{n+1})^2) \right] \\ & + \frac{\Delta t}{\Delta x} g h_{i+\frac{1}{2},j}^{n+1} (z_{i+1,j} - z_{i,j}) = 0, \quad (1.19) \end{aligned}$$

where

$$h_{i+\frac{1}{2},j}^n := \frac{h_{i,j}^n + h_{i+1,j}^n}{2}, \quad (1.20)$$

$$p_{i,j}^n := \frac{p_{i+\frac{1}{2},j}^n + p_{i-\frac{1}{2},j}^n}{2}, \quad \hat{u}_{i,j}^n := \begin{cases} u_{i-\frac{1}{2},j} & \text{if } p_{i,j}^n \geq 0 \\ u_{i+\frac{1}{2},j} & \text{if } p_{i,j}^n < 0 \end{cases}, \quad (1.21)$$

$$q_{i+\frac{1}{2},j+\frac{1}{2}}^n := \frac{q_{i+1,j+\frac{1}{2}}^n + q_{i,j+\frac{1}{2}}^n}{2}, \quad \hat{u}_{i+\frac{1}{2},j+\frac{1}{2}}^n := \begin{cases} u_{i+\frac{1}{2},j} & \text{if } q_{i+\frac{1}{2},j+\frac{1}{2}}^n \geq 0 \\ u_{i+\frac{1}{2},j+1} & \text{if } q_{i+\frac{1}{2},j+\frac{1}{2}}^n < 0 \end{cases}. \quad (1.22)$$

The momentum balance equation in the y -direction (1.15) is discretized according to similar principles. For all $(i, j) \in \mathcal{M}$,

$$\begin{aligned} h_{i,j+\frac{1}{2}}^{n+1} v_{i,j+\frac{1}{2}}^{n+1} - h_{i,j+\frac{1}{2}}^n v_{i,j+\frac{1}{2}}^n + \frac{\Delta t}{\Delta x} & \left[p_{i+\frac{1}{2},j+\frac{1}{2}}^n \hat{v}_{i+\frac{1}{2},j+\frac{1}{2}}^n - p_{i+\frac{1}{2},j-\frac{1}{2}}^n \hat{v}_{i+1/2,j-1/2}^n \right] \\ & + \frac{\Delta t}{\Delta y} \left[(q_{i,j+1}^n \hat{v}_{i,j+1}^n - q_{i,j}^n \hat{v}_{i,j}^n) + \frac{1}{2} g((h_{i,j+1}^{n+1})^2 - (h_{i,j}^{n+1})^2) \right] \\ & + \frac{\Delta t}{\Delta y} g h_{i,j+\frac{1}{2}}^{n+1} (z_{i,j+1} - z_{i,j}) = 0, \quad (1.23) \end{aligned}$$

where

$$h_{i,j+\frac{1}{2}}^n := \frac{h_{i,j}^n + h_{i,j+1}^n}{2}, \quad (1.24)$$

$$q_{i,j}^n := \frac{q_{i,j+\frac{1}{2}}^n + q_{i,j-\frac{1}{2}}^n}{2}, \quad \hat{v}_{i,j}^n := \begin{cases} v_{i,j-\frac{1}{2}} & \text{if } q_{i,j}^n \geq 0 \\ v_{i,j+\frac{1}{2}} & \text{if } q_{i,j}^n < 0 \end{cases}, \quad (1.25)$$

$$p_{i+\frac{1}{2},j+\frac{1}{2}}^n := \frac{p_{i+\frac{1}{2},j+1}^n + p_{i+\frac{1}{2},j}^n}{2}, \quad \hat{v}_{i+\frac{1}{2},j+\frac{1}{2}}^n := \begin{cases} v_{i,j+\frac{1}{2}} & \text{if } p_{i+\frac{1}{2},j+\frac{1}{2}}^n \geq 0 \\ v_{i+1,j+\frac{1}{2}} & \text{if } p_{i+\frac{1}{2},j+\frac{1}{2}}^n < 0 \end{cases}. \quad (1.26)$$

As the one-dimensional scheme, the two-dimensional scheme is conservative, well-balanced, positivity-preserving under a CFL-like condition, and at most first-order accurate. Here, this condition is

$$\Delta t \leq \frac{\Delta x}{(-u_{i-\frac{1}{2},j}^n)^+ + (u_{i+\frac{1}{2},j}^n)^+ + (-v_{i,j-\frac{1}{2}}^n)^+ + (v_{i,j+\frac{1}{2}}^n)^+}. \quad (1.27)$$

At each time step, the Courant number is defined by

$$\nu := \frac{\Delta t}{\Delta x} \max_{(i,j) \in \mathcal{M}} \left(\frac{|q_{i,j+\frac{1}{2}}^n + q_{i,j-\frac{1}{2}}^n|}{2h_{i,j}^n} + \sqrt{gh_{i,j}^n}, \frac{|p_{i+\frac{1}{2},j}^n + p_{i-\frac{1}{2},j}^n|}{2h_{i,j}^n} + \sqrt{gh_{i,j}^n} \right). \quad (1.28)$$

Remark 1.2.2. This two-dimensional staggered grid is also known as the Marker-And-Cell (MAC) grid or the Arakawa C-grid.

Remark 1.2.3. Staggered on unstructured meshes [25, 26, 29, 18, 6, 19]. However, the use of staggered schemes on unstructured meshes increases significantly the number of discrete unknowns.

1.2.3 Second-order accurate schemes

The staggered schemes can be modified in a very simple way in order to achieve second-order accuracy in space and time. For sake of brevity, we only describe the modifications for the one-dimensional scheme (1.6)-(1.8). The two-dimensional case can be treated along the same principles.

We first correct the upwind fluxes with a linear reconstruction and slope-limiter to avoid oscillations. For instance, with the minmod limiter, the new definitions of $\hat{h}_{i+\frac{1}{2}}^n$ and \hat{u}_i^n are

$$\hat{h}_{i+\frac{1}{2}}^n := \begin{cases} h_i^n + \frac{\Delta x}{2} \text{minmod} \left(\frac{h_{i+1}^n - h_i^n}{\Delta x}, \frac{h_i^n - h_{i-1}^n}{\Delta x} \right) & \text{if } u_{i+\frac{1}{2}}^n \geq 0 \\ h_{i+1}^n - \frac{\Delta x}{2} \text{minmod} \left(\frac{h_{i+2}^n - h_{i+1}^n}{\Delta x}, \frac{h_{i+1}^n - h_i^n}{\Delta x} \right) & \text{if } u_{i+\frac{1}{2}}^n < 0 \end{cases} \quad (1.29)$$

$$\hat{u}_i^n := \begin{cases} u_{i-\frac{1}{2}}^n + \frac{\Delta x}{2} \text{minmod} \left(\frac{u_{i+\frac{1}{2}}^n - u_{i-\frac{1}{2}}^n}{\Delta x}, \frac{u_{i-\frac{1}{2}}^n - u_{i-\frac{3}{2}}^n}{\Delta x} \right) & \text{if } q_i^n \geq 0 \\ u_{i+\frac{1}{2}}^n - \frac{\Delta x}{2} \text{minmod} \left(\frac{u_{i+\frac{3}{2}}^n - u_{i+\frac{1}{2}}^n}{\Delta x}, \frac{u_{i+\frac{1}{2}}^n - u_{i-\frac{1}{2}}^n}{\Delta x} \right) & \text{if } q_i^n < 0 \end{cases} \quad (1.30)$$

where

$$\text{minmod}(x, y) := \begin{cases} \min(x, y) & \text{if } x, y \geq 0, \\ \max(x, y) & \text{if } x, y \leq 0, \\ 0 & \text{otherwise.} \end{cases}$$

Then we replace the Euler-like time discretization by a two-stage time discretization. In order to describe this discretization, let us define the operator Φ such that the equation

$$(h_i^{n+1}, u_{i+\frac{1}{2}}^{n+1})_{i \in \mathcal{M}} = (h_i^n, u_{i+\frac{1}{2}}^n)_{i \in \mathcal{M}} + \Delta t \Phi \left((h_i^n, u_{i+\frac{1}{2}}^n, h_i^{n+1})_{i \in \mathcal{M}} \right).$$

is equivalent to (1.6)-(1.8) with the corrections (1.29)-(1.30). The second-order accurate scheme is thus defined as

$$\begin{aligned} (h_i^{n+1}, u_{i+\frac{1}{2}}^{n+1})_{i \in \mathcal{M}} &= (h_i^n, u_{i+\frac{1}{2}}^n)_{i \in \mathcal{M}} + \frac{\Delta t}{2} \Phi \left((h_i^n, u_{i+\frac{1}{2}}^n, h_i^n)_{i \in \mathcal{M}} \right) \\ &\quad + \frac{\Delta t}{2} \Phi \left((\tilde{h}_i^{n+1}, \tilde{u}_{i+\frac{1}{2}}^{n+1}, h_i^{n+1})_{i \in \mathcal{M}} \right), \end{aligned}$$

where

$$(\tilde{h}_i^{n+1}, \tilde{u}_{i+\frac{1}{2}}^{n+1})_{i \in \mathcal{M}} = (h_i^n, u_{i+\frac{1}{2}}^n)_{i \in \mathcal{M}} + \Delta t \Phi \left((h_i^n, u_{i+\frac{1}{2}}^n, \tilde{h}_i^{n+1})_{i \in \mathcal{M}} \right).$$

1.2.4 Friction term

Source terms are often added to the momentum equation to model friction phenomena. For instance the momentum equation with Darcy-Weisbach friction reads

$$\partial_t(hu) + \partial_x \left(hu^2 + \frac{1}{2}gh^2 \right) + gh\partial_x z + \frac{f}{8}u|u| = 0, \quad (1.31)$$

where f is a friction coefficient. With Manning friction, it reads

$$\partial_t(hu) + \partial_x \left(hu^2 + \frac{1}{2}gh^2 \right) + gh\partial_x z + Cu|u|/h^{1/3} = 0, \quad (1.32)$$

where C is a given coefficient.

The numerical treatment of the above friction term is straightforward in the staggered framework.

$$\begin{aligned} h_{i+\frac{1}{2}}^{n+1} u_{i+\frac{1}{2}}^{n+1} - h_{i+\frac{1}{2}}^n u_{i+\frac{1}{2}}^n + \frac{\Delta t}{\Delta x} \left[q_{i+1}^n \hat{u}_{i+1}^n - q_i^n \hat{u}_i^n + \frac{1}{2} g \left[(h_{i+1}^{n+1})^2 - (h_i^{n+1})^2 \right] \right. \\ \left. + gh_{i+\frac{1}{2}}^{n+1} (z_{i+1} - z_i) \right] + \Delta t \frac{f}{8} |u_{i+\frac{1}{2}}^n| u_{i+\frac{1}{2}}^{n+1} = 0. \quad (1.33) \end{aligned}$$

$$\begin{aligned} h_{i+\frac{1}{2}}^{n+1} u_{i+\frac{1}{2}}^{n+1} - h_{i+\frac{1}{2}}^n u_{i+\frac{1}{2}}^n + \frac{\Delta t}{\Delta x} \left[q_{i+1}^n \hat{u}_{i+1}^n - q_i^n \hat{u}_i^n + \frac{1}{2} g \left[(h_{i+1}^{n+1})^2 - (h_i^{n+1})^2 \right] \right. \\ \left. + gh_{i+\frac{1}{2}}^{n+1} (z_{i+1} - z_i) \right] + \Delta t C u_{i+\frac{1}{2}}^{n+1} |u_{i+\frac{1}{2}}^n| / (h_{i+\frac{1}{2}}^{n+1})^{1/3} = 0. \quad (1.34) \end{aligned}$$

1.3 Consistency with the entropy inequality

In this section, we study the entropy balance of the one-dimensional first-order staggered scheme. First, we establish an entropy balance for a semi-discrete version of the staggered scheme. It appears that the entropy decreases with time. Then, we establish an entropy balance for the fully discrete scheme. The explicit time discretization introduces some entropy production terms in the balance so that the entropy does not necessarily decreases at each time step. However, by passing to the limit in the discrete entropy balance, we are able to prove that the scheme is consistent with the global entropy inequality.

For any $a \in \mathbb{R}$, we set $a^- := \min(a, 0)$ and $a^+ := \max(a, 0)$.

1.3.1 Entropy

The entropy η for the shallow water equations is the sum of the kinetic energy, the potential energy and a term stemming from the topography:

$$\eta(h, hu) := \frac{1}{2} hu^2 + \frac{1}{2} gh^2 + ghz. \quad (1.35)$$

The entropy inequality reads

$$\partial_t \eta(h, hu) + \partial_x G(h, hu) \leq 0, \quad (1.36)$$

where the entropy flux G is defined by

$$G(h, hu) := \left(\frac{1}{2} hu^2 + gh^2 + ghz \right) u \quad (1.37)$$

1.3.2 Semi-discrete entropy balance

Consider the semi-discrete version (continuous in time) of the scheme (1.6)-(1.8):

$$d_t h_i + \frac{1}{\Delta x} \left(q_{i+\frac{1}{2}} - q_{i-\frac{1}{2}} \right) = 0, \quad (1.38)$$

$$\begin{aligned} d_t (h_{i+\frac{1}{2}} u_{i+\frac{1}{2}}) + \frac{1}{\Delta x} & (q_{i+1} \hat{u}_{i+1} - q_i \hat{u}_i \\ & + \frac{1}{2} g \left((h_{i+1})^2 - (h_i)^2 \right) + gh_{i+\frac{1}{2}} (z_{i+1} - z_i)) = 0 \end{aligned} \quad (1.39)$$

where

$$q_{i+\frac{1}{2}} := \hat{h}_{i+\frac{1}{2}} u_{i+\frac{1}{2}}, \quad \hat{h}_{i+\frac{1}{2}} := \begin{cases} h_i & \text{if } u_{i+\frac{1}{2}} \geq 0, \\ h_{i+1} & \text{if } u_{i+\frac{1}{2}} < 0, \end{cases} \quad (1.40)$$

$$h_{i+\frac{1}{2}} := \frac{1}{2} (h_i + h_{i+1}), \quad (1.41)$$

$$q_i := \frac{1}{2} \left(q_{i-\frac{1}{2}} + q_{i+\frac{1}{2}} \right), \quad \hat{u}_i := \begin{cases} u_{i-\frac{1}{2}} & \text{if } q_i \geq 0 \\ u_{i+\frac{1}{2}} & \text{if } q_i < 0 \end{cases}. \quad (1.42)$$

In this Section, we will prove that semi-discrete staggered scheme (1.38)-(1.42) satisfies the semi-discrete entropy balance 1.36. Here, we gives two propositions they are related to difference components of energy (kinetic and elastic potential). The kinetic and elastic potential energy balances are given in Proposition 1 and Proposition 2 respectively.

Proposition 1. *The solution of the semi-discrete scheme (1.38)-(1.42) satisfies, for all $i \in \mathcal{M}$ and all $t \in [0, T]$, the balance*

$$\begin{aligned} \frac{1}{2} \Delta x d_t \left[h_{i+\frac{1}{2}} (u_{i+\frac{1}{2}})^2 \right] + \frac{1}{2} & \left[q_{i+1} (\hat{u}_{i+1})^2 - q_i (\hat{u}_i)^2 \right] \\ & + \frac{1}{2} g \left[(h_{i+1})^2 - (h_i)^2 \right] u_{i+\frac{1}{2}} + gh_{i+\frac{1}{2}} u_{i+\frac{1}{2}} (z_{i+1} - z_i) \leq 0 \end{aligned} \quad (1.43)$$

CHAPTER 1

Proof. From (1.38), we derive immediately

$$d_t h_{i+\frac{1}{2}} + \frac{1}{\Delta x} (q_{i+1} - q_i) = 0. \quad (1.44)$$

Multiplying (1.39) by $\Delta x u_{i+\frac{1}{2}}$ and (1.44) by $-\Delta x (u_{i+\frac{1}{2}})^2$, then adding these two equations, we find

$$\begin{aligned} & \frac{1}{2} \Delta x d_t \left(h_{i+\frac{1}{2}} (u_{i+\frac{1}{2}})^2 \right) - \frac{1}{2} \Delta x (u_{i+\frac{1}{2}})^2 d_t \left(h_{i+\frac{1}{2}} \right) + \left(q_{i+1} \left(\hat{u}_{i+1} - u_{i+\frac{1}{2}} \right) - q_i \left(\hat{u}_i - u_{i+\frac{1}{2}} \right) \right) u_{i+\frac{1}{2}} \\ & + \frac{1}{2} g u_{i+\frac{1}{2}} \left((h_{i+1})^2 - (h_i)^2 \right) + g h_{i+\frac{1}{2}} u_{i+\frac{1}{2}} (z_{i+1} - z_i) = 0. \end{aligned} \quad (1.45)$$

Elementary algebraic manipulations yield

$$\begin{aligned} q_{i+1} \left(\hat{u}_{i+1} - u_{i+\frac{1}{2}} \right) u_{i+\frac{1}{2}} &= \frac{1}{2} q_{i+1} \left((\hat{u}_{i+1})^2 - (u_{i+\frac{1}{2}})^2 \right) - \frac{1}{2} q_{i+1} \left(\hat{u}_{i+1} - u_{i+\frac{1}{2}} \right)^2 \\ &= \frac{1}{2} q_{i+1} \left((\hat{u}_{i+1})^2 - (u_{i+\frac{1}{2}})^2 \right) - \frac{1}{2} (q_{i+1})^- \left(u_{i+\frac{3}{2}} - u_{i+\frac{1}{2}} \right)^2, \end{aligned} \quad (1.46)$$

and, similarly,

$$q_i \left(\hat{u}_i - u_{i+\frac{1}{2}} \right) u_{i+\frac{1}{2}} = \frac{1}{2} q_i \left((\hat{u}_i)^2 - (u_{i+\frac{1}{2}})^2 \right) - \frac{1}{2} (q_i)^+ \left(u_{i-\frac{1}{2}} - u_{i+\frac{1}{2}} \right)^2. \quad (1.47)$$

Inserting the relations (1.46) and (1.47) in (1.45), then recalling (1.44), we deduce the balance (1.43). \square

Proposition 2. *The solution of the semi-discrete scheme (1.38)-(1.42) satisfies, for all $i \in \mathcal{M}$ and all $t \in [0, T]$, the balance*

$$\begin{aligned} \Delta x d_t \left[\frac{1}{2} g(h_i)^2 \right] + \left[\frac{1}{2} g(\hat{h}_{i+\frac{1}{2}})^2 u_{i+\frac{1}{2}} - \frac{1}{2} g(\hat{h}_{i-\frac{1}{2}})^2 u_{i-\frac{1}{2}} \right] \\ + \frac{1}{2} g(h_i)^2 \left(u_{i+\frac{1}{2}} - u_{i-\frac{1}{2}} \right) \leq 0. \end{aligned} \quad (1.48)$$

Proof. Multiplying (1.38) by $g h_i$, we find

$$\Delta x d_t \left(\frac{1}{2} g(h_i)^2 \right) + g h_i \left(q_{i+\frac{1}{2}} - q_{i-\frac{1}{2}} \right) = 0. \quad (1.49)$$

A straightforward algebraic manipulation yields

$$\begin{aligned} gh_i q_{i+\frac{1}{2}} &= gh_i \hat{h}_{i+\frac{1}{2}} u_{i+\frac{1}{2}} = \frac{1}{2} g \left[(\hat{h}_{i+\frac{1}{2}})^2 + (h_i)^2 - (\hat{h}_{i+\frac{1}{2}} - h_i)^2 \right] u_{i+\frac{1}{2}} \\ &= \frac{1}{2} g \left[(\hat{h}_{i+\frac{1}{2}})^2 - (h_i)^2 \right] u_{i+\frac{1}{2}} - \frac{1}{2} g (h_{i+1} - h_i)^2 (u_{i+\frac{1}{2}})^-. \end{aligned} \quad (1.50)$$

and, similarly,

$$gh_i q_{i-\frac{1}{2}} = \frac{1}{2} g \left[(\hat{h}_{i-\frac{1}{2}})^2 - (h_i)^2 \right] u_{i-\frac{1}{2}} - \frac{1}{2} g (h_{i-1} - h_i)^2 (u_{i-\frac{1}{2}})^+. \quad (1.51)$$

Inserting the relations (1.50) and (1.51) in (1.49), we deduce the balance (1.48). \square

1.3.3 Discrete balances

In order to see the ability of the scheme to satisfy the global discrete entropy balance, here we establish the discrete balance. Propositions 3 and 4 are given for the discrete kinetic and potential energy balance respectively.

Proposition 3. *The discrete solution of the scheme (1.6)-(1.8) satisfies, for all $i \in \mathcal{M}$ and all $n \in \{0, \dots, N_t\}$, the balance*

$$\begin{aligned} \frac{1}{2} \frac{\Delta x}{\Delta t} \left(h_{i+\frac{1}{2}}^{n+1} (u_{i+\frac{1}{2}}^{n+1})^2 - h_{i+\frac{1}{2}}^n (u_{i+\frac{1}{2}}^n)^2 \right) + \frac{1}{2} \left(q_{i+1}^n (\hat{u}_{i+1}^n)^2 - q_i^n (\hat{u}_i^n)^2 \right) \\ + \frac{1}{2} g \left((h_{i+1}^{n+1})^2 - (h_i^{n+1})^2 \right) u_{i+\frac{1}{2}}^{n+1} + gh_{i+\frac{1}{2}}^{n+1} u_{i+\frac{1}{2}}^{n+1} (z_{i+1} - z_i) = -R_{i+\frac{1}{2}}^{n+1} \end{aligned} \quad (1.52)$$

with

$$\begin{aligned} R_{i+\frac{1}{2}}^{n+1} := \frac{1}{2} \frac{\Delta x}{\Delta t} h_{i+\frac{1}{2}}^{n+1} \left(u_{i+\frac{1}{2}}^{n+1} - u_{i+\frac{1}{2}}^n \right)^2 + \frac{1}{2} \left((q_{i+1}^n)^- (u_{i+\frac{3}{2}}^n - u_{i+\frac{1}{2}}^n)^2 - (q_i^n)^+ (u_{i-\frac{1}{2}}^n - u_{i+\frac{1}{2}}^n)^2 \right) \\ - \left[(q_{i+1}^n)^- (u_{i+\frac{3}{2}}^n - u_{i+\frac{1}{2}}^n) - (q_i^n)^+ (u_{i-\frac{1}{2}}^n - u_{i+\frac{1}{2}}^n) \right] \left(u_{i+\frac{1}{2}}^{n+1} - u_{i+\frac{1}{2}}^n \right) \end{aligned} \quad (1.53)$$

Proof. From (1.6), we derive immediately

$$h_{i+\frac{1}{2}}^{n+1} - h_{i+\frac{1}{2}}^n + \frac{\Delta t}{\Delta x} (q_{i+1}^n - q_i^n) = 0. \quad (1.54)$$

We multiply (1.8) by $\Delta x / \Delta t$ $u_{i+\frac{1}{2}}^{n+1}$ and (1.54) by $\Delta x / \Delta t$ $u_{i+\frac{1}{2}}^{n+1} u_{i+\frac{1}{2}}^n$, then we subtract

these two equations, which yields

$$\begin{aligned} \frac{\Delta x}{\Delta t} h_{i+\frac{1}{2}}^{n+1} u_{i+\frac{1}{2}}^{n+1} \left(u_{i+\frac{1}{2}}^{n+1} - u_{i+\frac{1}{2}}^n \right) + \left(q_{i+1}^n \left(\hat{u}_{i+1}^n - u_{i+\frac{1}{2}}^n \right) - q_i^n \left(\hat{u}_i^n - u_{i+\frac{1}{2}}^n \right) \right) u_{i+\frac{1}{2}}^{n+1} \\ + \frac{1}{2} g u_{i+\frac{1}{2}}^{n+1} \left((h_{i+1}^{n+1})^2 - (h_i^{n+1})^2 \right) + g h_{i+\frac{1}{2}}^{n+1} u_{i+\frac{1}{2}}^{n+1} (z_{i+1} - z_i) = 0. \quad (1.55) \end{aligned}$$

Using the identities

$$\frac{\Delta x}{\Delta t} h_{i+\frac{1}{2}}^{n+1} u_{i+\frac{1}{2}}^{n+1} \left(u_{i+\frac{1}{2}}^{n+1} - u_{i+\frac{1}{2}}^n \right) = \frac{\Delta x}{2\Delta t} h_{i+\frac{1}{2}}^{n+1} \left((u_{i+\frac{1}{2}}^{n+1})^2 - (u_{i+\frac{1}{2}}^n)^2 \right) + \frac{\Delta x}{2\Delta t} h_{i+\frac{1}{2}}^{n+1} \left(u_{i+\frac{1}{2}}^{n+1} - u_{i+\frac{1}{2}}^n \right)^2, \quad (1.56)$$

$$\begin{aligned} q_{i+1}^n \left(\hat{u}_{i+1}^n - u_{i+\frac{1}{2}}^n \right) u_{i+\frac{1}{2}}^{n+1} &= \frac{1}{2} q_{i+1}^n \left((\hat{u}_{i+1}^n)^2 - (u_{i+\frac{1}{2}}^n)^2 \right) + \frac{1}{2} (q_{i+1}^n)^- \left(u_{i+\frac{3}{2}}^n - u_{i+\frac{1}{2}}^n \right)^2 \\ &\quad + (q_{i+1}^n)^- \left(u_{i+\frac{3}{2}}^n - u_{i+\frac{1}{2}}^n \right) \left(u_{i+\frac{1}{2}}^{n+1} - u_{i+\frac{1}{2}}^n \right) \quad (1.57) \end{aligned}$$

and

$$\begin{aligned} q_i^n \left(\hat{u}_i^n - u_{i+\frac{1}{2}}^n \right) u_{i+\frac{1}{2}}^{n+1} &= \frac{1}{2} q_i^n \left((\hat{u}_i^n)^2 - (u_{i+\frac{1}{2}}^n)^2 \right) + \frac{1}{2} (q_i^n)^+ \left(u_{i-\frac{1}{2}}^n - u_{i+\frac{1}{2}}^n \right)^2 \\ &\quad + (q_i^n)^+ \left(u_{i-\frac{1}{2}}^n - u_{i+\frac{1}{2}}^n \right) \left(u_{i+\frac{1}{2}}^{n+1} - u_{i+\frac{1}{2}}^n \right) \quad (1.58) \end{aligned}$$

in (1.55) we find

$$\begin{aligned} \frac{\Delta x}{2\Delta t} h_{i+\frac{1}{2}}^{n+1} \left((u_{i+\frac{1}{2}}^{n+1})^2 - (u_{i+\frac{1}{2}}^n)^2 \right) + \frac{1}{2} q_{i+1}^n \left((\hat{u}_{i+1}^n)^2 - (u_{i+\frac{1}{2}}^n)^2 \right) - \frac{1}{2} q_i^n \left((\hat{u}_i^n)^2 - (u_{i+\frac{1}{2}}^n)^2 \right) \\ + \frac{1}{2} g \left((h_{i+1}^{n+1})^2 - (h_i^{n+1})^2 \right) u_{i+\frac{1}{2}}^{n+1} + g h_{i+\frac{1}{2}}^{n+1} u_{i+\frac{1}{2}}^{n+1} (z_{i+1} - z_i) = -R_{i+\frac{1}{2}}^{n+1} \quad (1.59) \end{aligned}$$

where $R_{i+\frac{1}{2}}^{n+1}$ is defined by (1.53). Finally we deduce de desired equation (1.52) using

$$\left(h_{i+\frac{1}{2}}^{n+1} - h_{i+\frac{1}{2}}^n \right) (u_{i+\frac{1}{2}}^n)^2 + \frac{\Delta t}{\Delta x} \left(q_{i+1}^n - q_i^n \right) (u_{i+\frac{1}{2}}^n)^2 = 0. \quad (1.60)$$

which is simply (1.54) times $(u_{i+\frac{1}{2}}^n)^2$. \square

Proposition 4. *The discrete solution of the scheme (1.6)-(1.8) satisfies, for all*

$i \in \mathcal{M}$ and all $n \in \{0, \dots, N_t\}$, the balance

$$\begin{aligned} \frac{\Delta x}{\Delta t} \left(\frac{1}{2} g(h_i^{n+1})^2 - \frac{1}{2} g(h_i^n)^2 \right) + \left(\frac{1}{2} g(\hat{h}_{i+\frac{1}{2}}^n)^2 u_{i+\frac{1}{2}}^n - \frac{1}{2} g(\hat{h}_{i-\frac{1}{2}}^n)^2 u_{i-\frac{1}{2}}^n \right) \\ + \frac{1}{2} g(h_i^n)^2 (u_{i+\frac{1}{2}}^n - u_{i-\frac{1}{2}}^n) = -R_i^{n+1} \quad (1.61) \end{aligned}$$

with

$$\begin{aligned} R_i^{n+1} := & \frac{1}{2} g \frac{\Delta x}{\Delta t} (h_i^{n+1} - h_i^n)^2 + \\ & \frac{1}{2} (h_{i+1}^n - h_i^n)^2 (u_{i+\frac{1}{2}}^n)^- - \frac{1}{2} (h_{i-1}^n - h_i^n)^2 (u_{i-\frac{1}{2}}^n)^+ + g (h_i^{n+1} - h_i^n) (q_{i+\frac{1}{2}}^n - q_{i-\frac{1}{2}}^n) \quad (1.62) \end{aligned}$$

Proof. Multiplying (1.6) by gh_i^{n+1} , we find

$$\frac{\Delta x}{\Delta t} gh_i^{n+1} (h_i^{n+1} - h_i^n) + gh_i^n (q_{i+\frac{1}{2}}^n - q_{i-\frac{1}{2}}^n) + g (h_i^{n+1} - h_i^n) (q_{i+\frac{1}{2}}^n - q_{i-\frac{1}{2}}^n) = 0.$$

Using the identity

$$\frac{\Delta x}{\Delta t} gh_i^{n+1} (h_i^{n+1} - h_i^n) = \frac{\Delta x}{\Delta t} \left(\frac{1}{2} g(h_i^{n+1})^2 - \frac{1}{2} g(h_i^n)^2 \right) + \frac{\Delta x}{2\Delta t} (h_i^{n+1} - h_i^n)^2,$$

and relations similar to (1.50) and (1.51), we turn into the balance (1.61). \square

As recorded in [32, 26], $R_{i+\frac{1}{2}}^{n+1}$ can be proved as non-negative under the CFL condition. The other hand, unfortunately, we can not able to prove that $R_i^{n+1} \geq 0$ in any case, therefore a discrete counterpart of the global entropy estimate (1.36) is not satisfied. However, by passing to the limit in the discrete entropy balance (see Chapter 1.3.4), we are able to prove that the scheme is consistent with the global entropy inequality.

1.3.4 Consistency theorem

Let $Q_T := (0, T) \times \Omega$. We consider a sequence of discretizations indexed by $k \in \mathbb{N}$. In the k -th discretization, the domain Ω is divided in $N_x^{(k)}$ intervals of length $\Delta x^{(k)}$ and the time interval $[0, T]$ in $N_t^{(k)}$ steps of length $\Delta t^{(k)}$. We assume that the meshsize $\Delta x^{(k)}$ and the time step $\Delta t^{(k)}$ tend to zero when k tend to infinity. We define the

CHAPTER 1

approximate solutions $h^{(k)} : Q_T \rightarrow \mathbb{R}$ and $u^{(k)} : Q_T \rightarrow \mathbb{R}$ such that

$$\begin{aligned} h^{(k)}(t, x) &= h_i^n && \text{if } t \in [t^n, t^{n+1}), x \in [x_{i-\frac{1}{2}}, x_{i+\frac{1}{2}}) \\ u^{(k)}(t, x) &= u_{i+\frac{1}{2}}^n && \text{if } t \in [t^n, t^{n+1}), x \in [x_i, x_{i+1}) \\ \tilde{h}^{(k)}(t, x) &= h_i^{n+1} && \text{if } t \in (t^n, t^{n+1}], x \in [x_{i-\frac{1}{2}}, x_{i+\frac{1}{2}}) \\ \tilde{u}^{(k)}(t, x) &= u_{i+\frac{1}{2}}^{n+1} && \text{if } t \in (t^n, t^{n+1}], x \in [x_i, x_{i+1}) \end{aligned}$$

Let us define the discrete norms

$$\|h^{(k)}\|_{k,BV_x} := \sum_{n=0}^{N_t^{(k)}} \sum_{i=1}^{N_x^{(k)}-1} \Delta t^{(k)} |h_{i+1}^n - h_i^n| \quad (1.63)$$

$$\|h^{(k)}\|_{k,BV_t} := \sum_{n=0}^{N_t^{(k)}-1} \sum_{i=1}^{N_x^{(k)}} \Delta x^{(k)} |h_i^{n+1} - h_i^n| \quad (1.64)$$

Assumption 1. *There exist constants C , independant of the discretization, such that*

$$0 < h^{(k)} \leq C, \quad |u^{(k)}| \leq C, \quad (1.65)$$

and

$$\|h^{(k)}\|_{k,BV_x} + \|u^{(k)}\|_{k,BV_x} \leq C. \quad (1.66)$$

Assumption 2. *There exist a constant C , independant of the discretization, such that*

$$\|h^{(k)}\|_{k,BV_t} \leq C. \quad (1.67)$$

Assumption 3. *The sequence $(\Delta x^{(k)}, \Delta t^{(k)})_{k \in \mathbb{N}}$ is such that*

$$\lim_{k \rightarrow +\infty} \frac{\Delta t^{(k)}}{\Delta x^{(k)}} = 0. \quad (1.68)$$

Theorem 1. *If the sequence $(h^{(k)}, u^{(k)}, \tilde{h}^{(k)}, \tilde{u}^{(k)})$ and $z \in C^1(\bar{\Omega})$ satisfies the estimates of Assumptions 1, 2 and 3, and converges in $L^p(Q_T) \times L^p(Q_T)$, with $p \in [1, +\infty)$, then its limit (h, u) satisfy*

$$\int_{Q_T} \left(\eta(h, hu) \partial_t \varphi + G(h, hu) \partial_x \varphi \right) dx dt + \int_{Q_T} ghu \partial_x z \varphi dx dt \geq 0, \quad (1.69)$$

with $\eta(h, hu) = \frac{1}{2}hu^2 + \frac{1}{2}gh^2$, $G(h, hu) = \left(\frac{1}{2}hu^2 + gh^2\right)u$, and for all nonnegative test functions $\varphi \in C_c^\infty(Q_T)$.

Proof. The proof consists in passing to the limit in the discrete mass equation, the discrete momentum equation, and the discrete entropy balance (see Appendix (B.2)). The only difference with the proof of [26, 32] is the presence of topography terms in the discrete momentum equation and the discrete entropy balance. \square

1.4 Standard numerical tests

We test the staggered scheme on various problems involving shocks, non-flat topography, dry-wet transition, friction, steady state at rest or discontinuous topography. All the problems are one-dimensional, except the last one, which is two-dimensional.

In most of the problems, the numerical results of the staggered scheme are compared to a reference solution (the exact solution or an approximation of the exact solution) in order to assess the accuracy of the staggered scheme. The error between the numerical solutions and the reference solution is computed and a convergence rate is deduced. The error is measured in L^1 -norm at the final time of the simulation. Let T be the final time of the simulation. Let (\bar{h}, \bar{u}) be the piecewise continuous reconstruction on the space-time domain of a numerical solution and $(h_{\text{ref}}, u_{\text{ref}})$ be the reference solution, then the error is

$$\|Err\|_{L^1(\Omega)} = \int_{\Omega} |\bar{h}(T, x) - h_{\text{ref}}(T, x)| dx + \int_{\Omega} |\bar{h}(T, x)\bar{u}(T, x) - h_{\text{ref}}(T, x)u_{\text{ref}}(T, x)| dx, \quad (1.70)$$

where, in practice, the integrals are computed using suitable quadrature formulas. The numerical convergence rate τ_{12} between two different number of cells is computed by

$$\tau_{12} = \frac{\log(\|Err_2\|_{L^1(\Omega)} / \|Err_1\|_{L^1(\Omega)})}{\log(\text{cells}_1 / \text{cells}_2)}. \quad (1.71)$$

where, $\|Err_1\|_{L^1(\Omega)}$ and $\|Err_2\|_{L^1(\Omega)}$ are the L^1 -norm error of cells_1 and cells_2 respectively.

The numerical results of the staggered scheme are also compared in some cases with those of two reference collocated schemes. These two reference schemes are the Suliciu scheme (also called HLLC scheme) and the kinetic scheme. They are based

on approximate Riemann solvers. We refer to [7] for a thorough description.

All the simulations are performed at the limit CFL condition (the CFL condition for the Suliciu and kinetic schemes is stated in [7]).

1.4.1 Accuracy test

This first problem, taken from [7], is designed to assess the accuracy of the scheme with a non-flat topography. The domain is $\Omega = [0, 40]$ and the topography is

$$z(x) = \begin{cases} 0.48 \left(1 - \left(\frac{x-20}{4}\right)^2\right) & \text{if } |x - 20| \leq 4, \\ 0 & \text{otherwise.} \end{cases}$$

The initial water height is $h_{\text{ini}}(x) = 4$ and the initial velocity is $u_{\text{ini}}(x) = 10/4$. The final time of simulation is $T = 1$. There is no analytical solution to this problem, therefore a reference solution is computed with the Suliciu scheme on a very fine grid.

Figure 1.3 shows the water height and the velocity profile each schemes with 50 points grid.

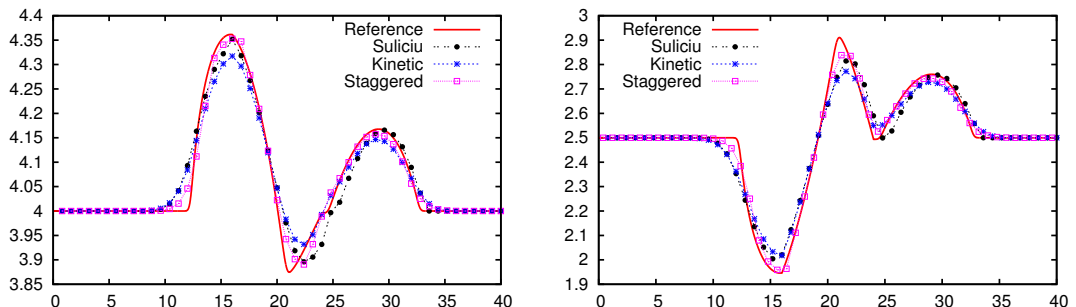


Figure 1.3: Accuracy test. Water level (left) and velocity (right) at final time. The number of cells is 50.

Table 1.1 shows the comparison of first order L^1 -norm error between staggered and collocated schemes. We can see clearly that in Table 1.1 all schemes are have a good convergence rate τ (is computed by (1.71)) in various grids number where it tends to 1 since computed in first order. In this numerical test, the discrete L^1 -norm errors of Suliciu scheme are shown smaller than the other schemes. Indeed, here we use a reference solution is computed with second order Suliciu scheme in space

Cells	Staggered		Suliciu		Kinetic	
	$\ Err\ _{L^1(\Omega)}$	τ	$\ Err\ _{L^1(\Omega)}$	τ	$\ Err\ _{L^1(\Omega)}$	τ
100	2.112E-0	/	2.003E-0	/	2.705E-0	/
200	1.174E-0	0.85	1.085E-0	0.88	1.522E-0	0.83
400	6.432E-1	0.87	5.744E-1	0.92	8.346E-1	0.86
800	3.493E-1	0.88	3.017E-1	0.93	4.553E-1	0.87

Table 1.1: Accuracy test. Error and convergence rate of first-order scheme.

Cells	Staggered		Suliciu		Kinetic	
	$\ Err\ _{L^1(\Omega)}$	τ	$\ Err\ _{L^1(\Omega)}$	τ	$\ Err\ _{L^1(\Omega)}$	τ
100	9.582E-1	/	1.250E-0	/	1.240E-0	/
200	3.708E-1	1.37	4.790E-1	1.38	4.950E-1	1.32
400	1.515E-1	1.30	1.900E-1	1.33	2.000E-1	1.31
800	5.581E-2	1.44	7.330E-2	1.37	8.400E-2	1.25

Table 1.2: Accuracy test. Error and convergence rate of second-order minmod.

and time. However, the error and the convergence rate are satisfied for all schemes. Here, we can observe also that, the staggered grid scheme is as accurate as the collocated schemes. Additionally, Table 1.2 shows the second order L^1 -norm error for all schemes. Moreover, in Table 1.2, staggered scheme shows as well as a nice convergence rate in second order accuracy. It has increasing accuracy number which is greater than 1 associate with the increasing number of points. In this simulation, we used the CFL number is equal to 1 for first order computations and equal to half of the one for second order computation.

1.4.2 Dam break on a wet bed

The domain is $\Omega = [0, 1]$ and the topography is flat. The initial velocity is zero and the initial water height is

$$h_{\text{ini}}(x) = \begin{cases} 1 & \text{if } x \leq 0.5, \\ 0.2 & \text{otherwise.} \end{cases}$$

The solution of this problem consists of a shock and a rarefaction wave. Its analytical expression can be found in [15] or in Appendix A.1.1 for instance. The numerical solution obtained with the staggered scheme is in very good agreement with the exact solution (see Figure 1.4 and 1.5). The staggered scheme yields a

sharper shock than the kinetic and Suliciu schemes. However, a small overshoot in the water height and the velocity can be observed upstream from the shock for the staggered scheme. This overshoot does not occur in the kinetic and Suliciu schemes. Table 1.3 collects the L^1 -error between the analytical solution and the numerical solutions at time $t = 0.1$ for various meshsizes (keeping a CFL equal to 1). The numerical convergence rate of the staggered scheme in L^1 -norm is slightly less than 0.8 for h and about 0.8 for u . These convergence rates are comparable to those obtained with the kinetic and Suliciu schemes.

The staggered scheme with an explicit pressure, discussed in Remark 1.2.1, has also been tested on the dam break problem. The non-entropic character of this variant is confirmed by the simulations; see the occurrence of a non-entropic shock at the left end of the rarefaction wave in Figure 1.6.

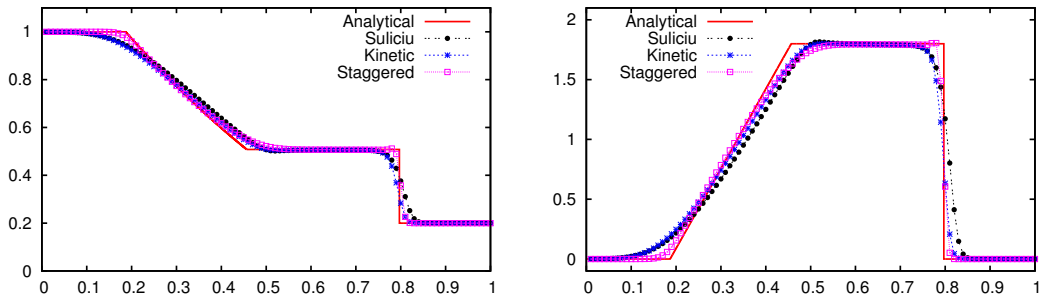


Figure 1.4: Dam break on a wet bed. Water height (left) and velocity (right) at time $t = 0.1$. The number of cells is 100.

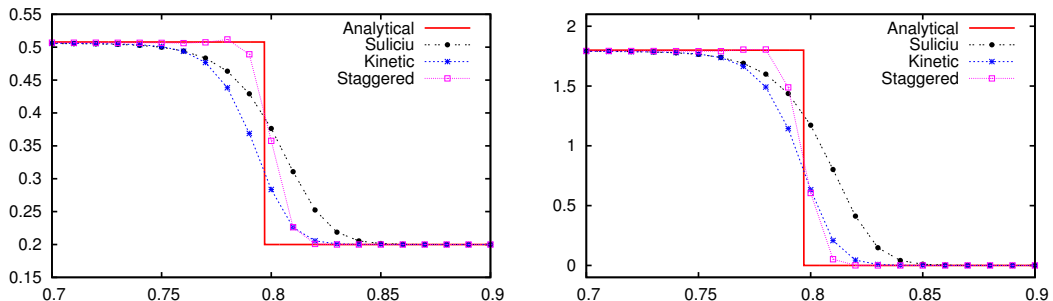


Figure 1.5: Dam break on a wet bed. Water height (left) and velocity (right) around the shock at time $t = 0.1$. The number of cells is 100.

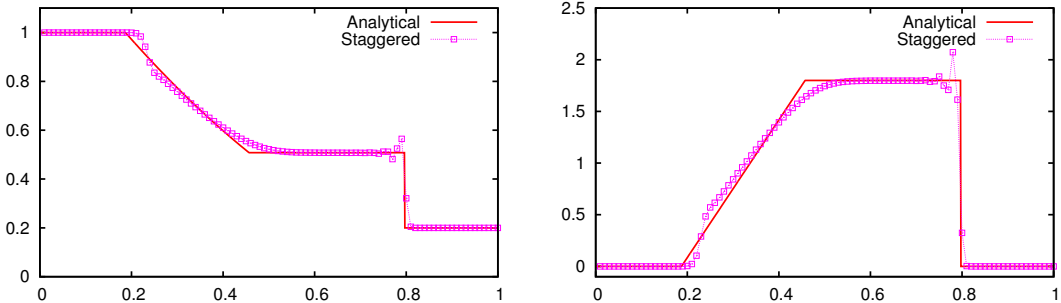


Figure 1.6: Dam break on a wet bed. Water height (left) and velocity (right) at time $t = 0.1$. The number of cells is 100.

Cells	Staggered		Suliciu		Kinetic	
	$\ Err\ _{L^1(\Omega)}$	τ	$\ Err\ _{L^1(\Omega)}$	τ	$\ Err\ _{L^1(\Omega)}$	τ
100	2.209E-2	/	5.476E-2	/	5.693E-2	/
200	1.316E-2	0.75	3.152E-2	0.79	3.290E-2	0.79
400	7.244E-3	0.86	1.828E-2	0.78	1.927E-2	0.77
800	4.274E-3	0.76	1.059E-2	0.78	1.123E-2	0.78

Table 1.3: Dam break on a wet bed. Error and convergence rate.

1.4.3 Transcritical flow

This problem simulates a flow over a bump. The domain is $\Omega = [0, 25]$ and the topography is

$$z(x) = \begin{cases} 0.2 - 0.05(x - 10)^2 & \text{if } 8 < x < 12, \\ 0 & \text{otherwise.} \end{cases}$$

The initial conditions are $h_{\text{ini}} = 0.33 - z(x)$ and $u_{\text{ini}} = 0.18/0.33$. At the upstream end of the domain, the discharge is enforced ($hu(x = 0, t) = 0.18$), while, at the downstream end, the water height is prescribed ($u(25, t) = 0.33$). After a time long enough ($t \geq 100$), the flow reaches a steady state. Upstream from the top of the bump, the flow is subcritical; downstream, it becomes supercritical, then, after a hydraulic jump, it is subcritical again. The staggered scheme reproduces quite accurately the final steady state and captures well the location of the shock. (see Figure 1.7). The kinetic and Suliciu schemes seem to yield a slightly better shock profile than the staggered scheme. The numerical convergence rate of the staggered scheme in L^1 -norm is close to 1 for both h and u , which is comparable to the kinetic and Suliciu schemes (see Table 1.4).

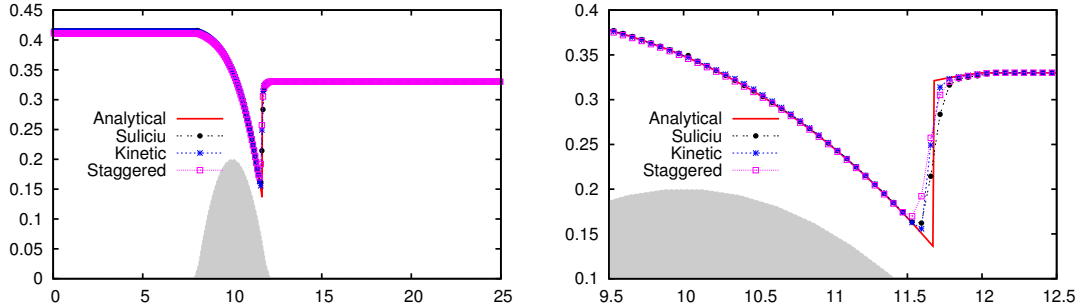


Figure 1.7: Transcritical flow with shock. Water level $h + z$ at time $t = 200$. The right figure is a zoom of the left figure. The number of cells is 200.

Cells	Staggered		Suliciu		Kinetic	
	$\ Err\ _{L^1(\Omega)}$	τ	$\ Err\ _{L^1(\Omega)}$	τ	$\ Err\ _{L^1(\Omega)}$	τ
100	1.476E-1	/	0.922E-1	/	0.797E-1	/
200	7.440E-2	0.98	4.997E-2	0.88	4.047E-2	0.97
400	3.758E-2	0.98	2.572E-2	0.95	2.038E-2	0.98
800	1.899E-2	0.98	1.322E-2	0.95	1.019E-2	0.99

Table 1.4: Transcritical with shock. Error and convergence rate.

1.4.4 Oscillations in a parabola

To study the ability of our scheme to compute vacuum or dry bed, here we elaborate the oscillation of fluid in a parabola introduced in [44, 14] or in Appendix A.1.2. The domain of this simulation is $\Omega = [-2, 2]$ and the topography is a parabola $z(x) = 0.5(x^2 - 1)$. The initial velocity is zero and the initial water height is

$$h_{\text{ini}}(x) = \begin{cases} -z(x + 0.5) & \text{if } -1.5 < x < 0.5, \\ 0 & \text{otherwise.} \end{cases}$$

The solution is periodic in time: the water oscillates in the parabola, the surface remaining planar. The analytical expression of the solution can be found in [14]. The numerical simulations show that the staggered scheme is able to treat accurately dry-wet transitions (see Figure 1.8). For this problem, the staggered scheme is even more accurate than the collocated schemes. The numerical convergence rate of the staggered scheme in L^1 -norm is very close to 1 for both h and hu and seems slightly better than the kinetic and Suliciu schemes (see Table 1.5). The CFL number is used is 1 in this simulation.

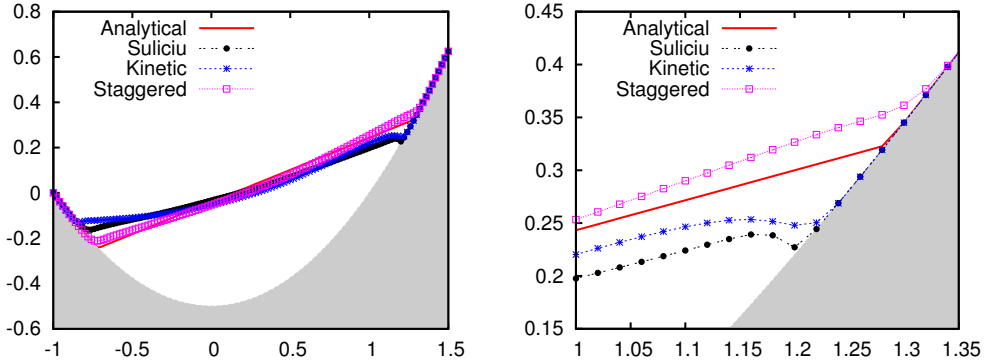


Figure 1.8: Oscillations in a parabola. Water level $h + z$ at time $t = 2.7$. The right figure is a zoom of the left figure. The number of cells is 200.

Cells	Staggered		Suliciu		Kinetic	
	$\ Err\ _{L^1(\Omega)}$	τ	$\ Err\ _{L^1(\Omega)}$	τ	$\ Err\ _{L^1(\Omega)}$	τ
100	1.303E-1	/	3.699E-1	/	4.989E-1	/
200	7.133E-2	0.87	2.108E-1	0.81	3.244E-1	0.62
400	3.753E-2	0.92	1.138E-1	0.89	1.967E-1	0.72
800	1.914E-2	0.97	5.982E-2	0.92	1.116E-1	0.81

Table 1.5: Oscillations in a parabola. Error and convergence rate.

1.4.5 Dam break on dry bed with friction

This problem simulates a dam break with friction (more precisely Darcy-Weisbach friction). The domain is $\Omega = [0, 2000]$. The initial velocity is zero and the water height is

$$h_{\text{ini}}(x) = \begin{cases} 6 & \text{if } x \leq L/2, \\ 0 & \text{otherwise.} \end{cases}$$

The friction coefficient is $f = 8g/40^2$. Various analytical approximations of the exact solution can be computed for this problem. The reference solution considered herein is the Dressler approximation (described in [15]). The results of this test are shown in the Figure 1.9 at final time $t = 40$. This approximation locates accurately the dry-wet transition but does not reproduce perfectly the profile of the wave tip. Here, we used the CFL number is equal to 1.

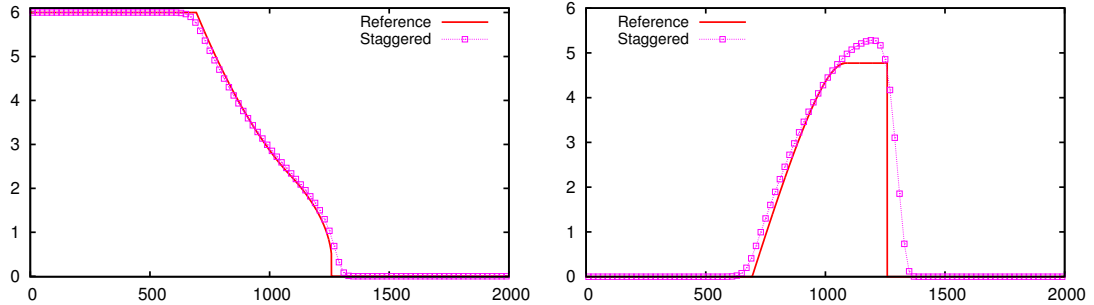


Figure 1.9: Dam break on dry bed with friction. Water height (left) and velocity (right) at time $t = 40$. The number of cells is 100.

1.4.6 Vacuum occurrence over a discontinuous topography

This test, taken from Gallouët et al.,[22], involves a discontinuous topography. The domain is $\Omega = [0, 25]$ and the topography is

$$z(x) = \begin{cases} 1 & \text{if } 25/3 < x < 12.5, \\ 0 & \text{otherwise.} \end{cases}$$

The initial water height is $h_{\text{ini}}(x) = 10 - z(x)$ and the initial velocity is such that

$$hu_{\text{ini}}(x) = \begin{cases} -350 & \text{if } x < 50/3, \\ 350 & \text{if } x \geq 50/3. \end{cases}$$

Neumann boundary conditions are prescribed at each boundaries and the CFL number is used is 1. Results from collocated and staggered scheme are shown in Figure 1.10. They show similar configuration at final time $t = 0.25$. Moreover, we can see that the schemes produce the wave over the jumps of topography which allocates with the results in [22, 7].

1.4.7 The steady state at rest

This test is taken from Perthame and Simeoni [33] concerning the steady state at rest, in order to show the steady state is preserved thus satisfy the well-balanced property. Here two numerical tests are given on a parabolic bump and a discontinuous step topography. The domain of this test is $\Omega = [-10 : 10]$. First, the initial

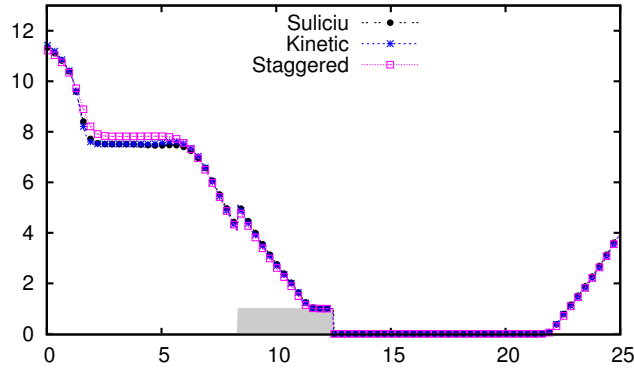


Figure 1.10: Vacuum occurrence over a discontinuous topography. Water level $h + z$ at time $t = 0.25$. The number of cells is 100.

condition of a bump topography is given as

$$z_{\text{ini}}(x) = \max(0, 0.2 - 0.05x^2),$$

moreover the initial conditions for velocity and water level are $u_{\text{ini}}(x) = 0$ and $(h + z)_{\text{ini}}(x) = 1$ respectively. The results using a parabolic bump topography are shown in Figure 1.11. We can see here clearly that, the water level is constant (equal to 1) for a long time simulation and the velocity also remains zero. Therefore, the steady state at rest is satisfied.

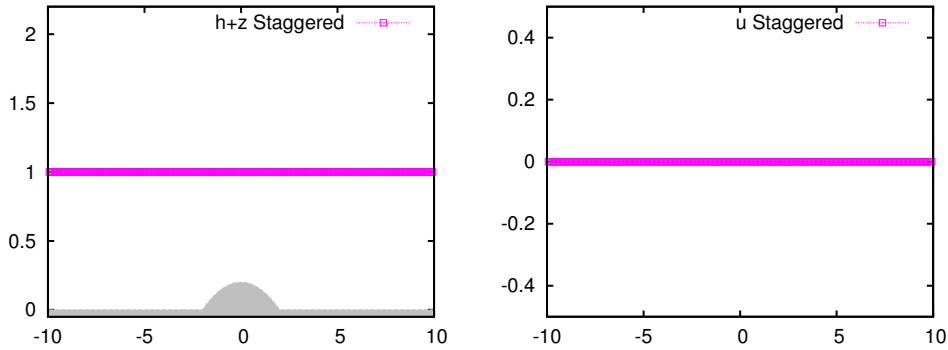


Figure 1.11: The steady state at rest over a bump. Water level (left) and velocity (right) at final time. The number of cells is 300.

Although using a discontinuous step of topography, the steady state at rest is also preserved. The results in water level and velocity profile are shown in Figure

1.12. The discontinuous step is given as

$$z_{\text{ini}}(x) = \begin{cases} 0, & \text{for } x \leq 0, \\ 0.3 & \text{for } x > 0. \end{cases}$$

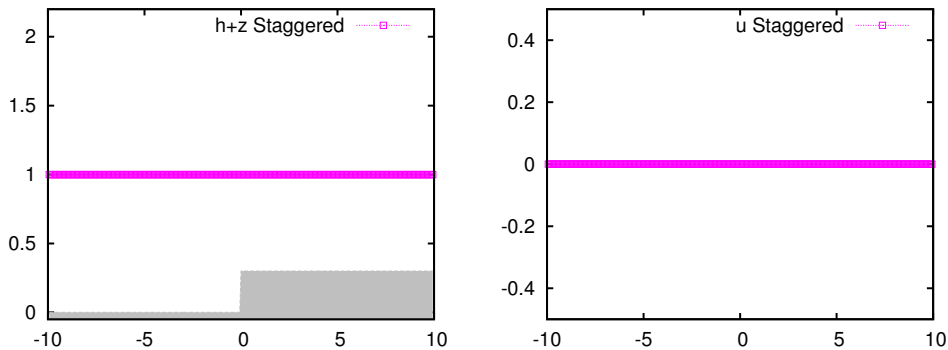


Figure 1.12: The steady state at rest over a discontinuous step. Water level (left) and velocity (right) at final time. The number of cells is 300.

Here, we used the number of cells is 300, the final time step is $T = 100$ and the Courant number is 1 for both simulations. These numerical tests, confirm that our scheme is well-balanced scheme i.e. preserves the steady state of a lake at rest.

1.4.8 Oscillations in a paraboloid

To asses our scheme into higher dimensional case, here we present a two-dimensional version of the oscillations in a parabola [14]. The domain is $\Omega = [0, L] \times [0, L]$, and the topography is given as the shape of a paraboloid:

$$z(x, y) = -h_0 \left(1 - \frac{(x - L/2)^2 + (y - L/2)^2}{a^2} \right), \quad \forall x, y \in \Omega,$$

where h_0 is the water depth at central point and a is the distance from the central point to the zero elevation of the shoreline. The analytical periodic solutions of this

test are given by,

$$h(x, y, t) = \max \left(0, \frac{\eta h_0}{a^2} \left(2 \left(x - \frac{L}{2} \right) \cos(\omega t) + 2 \left(y - \frac{L}{2} \right) \sin(\omega t) - \eta \right) - z(x, y) \right),$$

$$u(x, y, t) = -\eta \omega \sin(\omega t),$$

$$v(x, y, t) = \eta \omega \cos(\omega t),$$

where the frequency ω is defined as $\omega = \sqrt{2gh_0}/a$.

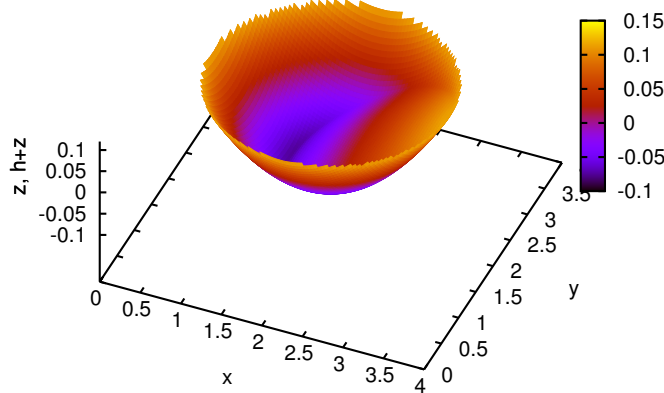


Figure 1.13: Oscillations in a paraboloid. Water level $h + z$ at time $t = 3\frac{2\pi}{\omega}$. The number of cells is 100×100 .

In this simulation, we used $t = 0$ at the analytical solutions as the initial conditions. The other parameters are given as $a = 1$, $h_0 = 0.1$, $\eta = 0.5$ and $L = 4$. The result of water level can be seen in Figure 1.13. This simulation can be imagined as the rotation of water inside a glass. Table 1.6 shows the first order of L^1 -norm error in some various grids at final time $t = 3\frac{2\pi}{\omega}$. It shows a good numerical convergence rate of the scheme by the increasing of accuracy numbers less than one. From Table 1.6, we also can conclude that staggered scheme is a robust scheme in two-dimensional as well as in one-dimensional case. The CFL number is used is 1 in this simulation.

Cells	Staggered	
	$\ Err\ _{L^1(\Omega)}$	τ
10×10	4.067E-1	/
20×20	1.943E-1	0.53
40×40	6.866E-2	0.75
80×80	2.444E-2	0.75

Table 1.6: Oscillations in paraboloid. Error and convergence rate.

1.5 Conclusion

The staggered scheme is an alternative to the collocated schemes for solving the shallow water equations. The numerical tests demonstrate that the staggered scheme is as accurate and robust as the collocated schemes. The staggered scheme presents the same mathematical guarantees as the collocated schemes. In particular, the staggered scheme is consistent with the entropy inequality. The componentwise computation of numerical fluxes is simpler than the approximate Riemann solvers and the well-balanced discretization of the topography source term is straightforward.

CHAPTER 1

Staggered conservative scheme for rotating shallow water equations on geostrophic flows²

This chapter is devoted to the description of a staggered conservative scheme for the rotating shallow water equations in one and two-dimension. The shallow water equations is approximated using the momentum conservative scheme, and the Coriolis terms is calculated using the Crank-Nicolson method. The resulting scheme is implemented for simulating various rotating phenomena, such as, Rossby wave, oscillation in a paraboloid, coastal and equatorial Kelvin waves. Comparison with exact solution or other conservative method give good agreement. Moreover, our numerical experiments satisfy entropy stability. Except from adjustment for the initial and boundary conditions, no special treatment are required for all simulations above. And these indicate the robustness of our staggered conservative scheme.

2.1 Introduction

We all live on a rotating earth. Motions of wind and currents we observe in daily life are motions on a rotating earth. Naturally, governing equations of geophysical fluid motion are written in a rotating frame of reference. A frame that rotates according to earth rotation. Basically, if the equations are written in this rotating frame, there are additional terms from the Coriolis force, which is a fictitious force. Due to Coriolis effect, wind moves spiral to the right (clockwise) in the Northern Hemisphere, and spiral to the left (anti-clockwise) in the Southern part, see Figure 2.1. And in the equator area there is no Coriolis effect. Most oceanic and atmospheric phenomena

²This chapter has been submitted as: P. H. Gunawan and S. R. Pudjaprasetya. "Staggered conservative scheme for rotating shallow water equations on geostrophic flows", 2014

occur over length scales much larger than vertical depth, and therefore shallow water description is adequate. The shallow water equations (SWE) with additional Coriolis terms is called rotating shallow water equations. These Coriolis terms are important effects for motions occurring over large distances and long periods of time, such as large-scale movement of air in the atmosphere or water in the ocean.

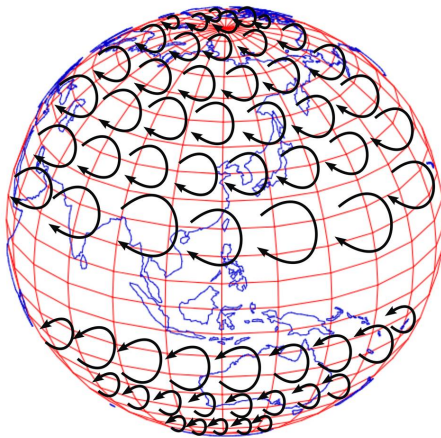


Figure 2.1: Illustration of the Coriolis force.

Commonly, in finite volume methods applied to shallow water equations, all unknowns are approximated on the same mesh (collocated grid) and the numerical fluxes are computed using an approximate Riemann solver. For the description and analysis of this approach, see for instance [7]; [30] and [45]. Different from the collocated finite volume, here we implement the staggered finite volume method to approximate the rotating shallow water equations (2.1) - (2.3). This scheme is chosen because it is efficient, relatively simple, and robust, see [16, 41, 34] for thorough discussions about this method. Moreover, thorough study in [16] has shown the staggered scheme produce nicely comparable results with the collocation method counterparts.

Organization of this chapter is as follows. In Section 2.2 we discuss the accurate scheme for calculating the Coriolis terms, followed with description of the staggered scheme for the 2D SWE. In Section 2.3, the scheme is implemented for various problems, such as, the classical Rossby wave and Kelvin wave simulation in coastal and equatorial area. Finally we summarize the results in Section 2.4.

2.2 Staggered conservative scheme for 2D rotating SWE

Under the influence of earth rotation and shallow water assumption, the motion of 2D fluid is appropriately modelled by SWE with an additional Coriolis force terms. Formulation of 2D SWE in conservative forms are as follows

$$\partial_t h + \partial_x(hu) + \partial_y(hv) = 0, \quad (2.1)$$

$$\partial_t(hu) + \partial_x\left(hu^2 + \frac{1}{2}gh^2\right) + \partial_y(huv) + gh\partial_x z - fhv = 0, \quad (2.2)$$

$$\partial_t(hv) + \partial_x(huv) + \partial_y\left(hv^2 + \frac{1}{2}gh^2\right) + gh\partial_y z + fhu = 0, \quad (2.3)$$

where h is the total water depth, u, v the fluid particle velocities in $x-$ and $y-$ directions, respectively. Further, $z(x, y)$ denotes the bottom topography, f the Coriolis parameter, and g the gravity acceleration.

Bouchut in Zeitlin [51], derives the entropy condition for the rotating SWE (2.1-2.3)

$$\partial_t\eta(h, hu, hv, z) + \partial_x G_x(h, hu, hv, z) + \partial_y G_y(h, hu, hv, z) \leq 0, \quad (2.4)$$

with the convex entropy

$$\eta(h, hu, hv, z) := \frac{1}{2}hu^2 + \frac{1}{2}hv^2 + \frac{1}{2}gh^2 + ghz, \quad (2.5)$$

and the associated entropy fluxes,

$$G_x(h, hu, hv, z) := \left(\frac{1}{2}hu^2 + \frac{1}{2}hv^2 + gh^2\right)u + ghzu, \quad (2.6)$$

$$G_y(h, hu, hv, z) := \left(\frac{1}{2}hu^2 + \frac{1}{2}hv^2 + gh^2\right)v + ghzv. \quad (2.7)$$

Since η is convex, integrating (2.4) in x and y gives

$$\frac{d}{dt} \left(\int \int \eta \, dx dy \right) \leq 0. \quad (2.8)$$

Entropy condition (2.8) will be used later to check the property of our numerical scheme.

In this section we formulate a staggered conservative scheme for the rotating

shallow water equations (2.1-2.3). We first discuss an accurate scheme to describe the motion of a free particle under Coriolis force. Then, we discuss the staggered momentum conservative scheme to approximate the 2D SWE.

2.2.1 Motion under Coriolis force

In the absence of other forces except Coriolis, a particle on earth experiences an inertial oscillation governed by the equations for velocity components

$$\partial_t u - fv = 0, \quad (2.9)$$

$$\partial_t v + fu = 0, \quad (2.10)$$

with $f = 2\Omega_r \sin \phi$ is the Coriolis parameter, $\Omega_r = 2\pi/T$ the rotation rate, T the rotation period, and ϕ the geographical latitude.

Implementing θ -scheme to approximate equations (2.9,2.10) yield

$$\begin{aligned} u^{n+1} &= u^n + \Delta t f \left((1-\theta)v^n + \theta v^{n+1} \right), \\ v^{n+1} &= v^n - \Delta t f \left((1-\theta)u^n + \theta u^{n+1} \right), \end{aligned} \quad (2.11)$$

for $n = 0, 1, \dots$ as time step index. When $\theta = 0$ the scheme (2.11) is explicit, $\theta = 1$ the scheme is implicit, and $\theta = 1/2$ the scheme is known as trapezoidal or Crank-Nicolson scheme. From eigenvalues analysis of the amplification matrix corresponds to (2.11), we obtain: explicit scheme is unstable, implicit and Crank-Nicolson scheme are unconditionally stable. Moreover, amplification matrix corresponds to the Crank-Nicolson scheme has eigenvalues with norm one, which means this scheme is free from numerical damping error. Once the velocity field $(u(t), v(t))$ is obtained, particle trajectory $(x(t), y(t))$ can be calculated from

$$\frac{dx}{dt} = u, \quad \frac{dy}{dt} = v$$

using forward Euler.

A particle initially at a position $x = 0$ and $y = 5$ km is obstructed by an initial speed $u = 0.5$ m/s and $v = 0.5$ m/s. We shall see its trajectory under a rotating frame at rate of -1.454×10^{-5} s⁻¹, that corresponds to clockwise rotation with a

period of 24 hours (see [28]). The computational simulation for the implicit and Crank-Nicolson scheme are shown in Figure 2.2.

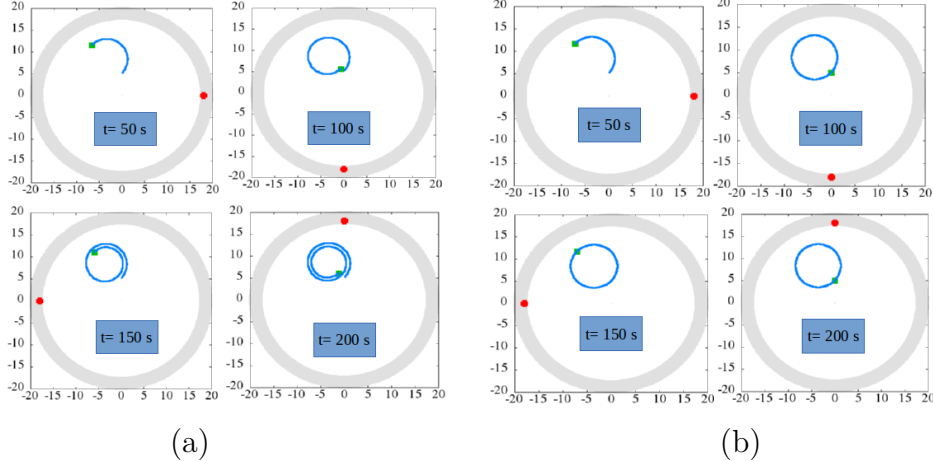


Figure 2.2: The parcel trajectory in a rotating frame. (a) Trajectory from the implicit Euler scheme. (b) Trajectory from Crank-Nicolson scheme. The red point denotes the reference location in the fixed frame of reference.

Results from the implicit scheme are given in Figure 2.2(a). Even though the scheme is stable, we observe a trajectory spiralling inward and a gradual decrease in speed, which is certainly incorrect. On the contrary, the Crank-Nicolson results as in Figure 2.2(b) show the correct results, which is a circular trajectory. Therefore, in further computations the Coriolis terms are calculated using Crank-Nicolson, with the explicit formula obtained from (2.11) for $\theta = 1/2$ as follows

$$\begin{aligned} u^{n+1} &= \left((1 - 0.25\alpha^2)u^n + \alpha v^n \right) / (1 + 0.25\alpha^2), \\ v^{n+1} &= \left((1 - 0.25\alpha^2)v^n - \alpha u^n \right) / (1 + 0.25\alpha^2), \end{aligned} \quad (2.12)$$

with $\alpha = f\Delta t$.

2.2.2 Staggered conservative scheme

In this section, the 2D staggered conservative scheme for rotating shallow water equations is formulated. The scheme is based on the momentum conservative approximation for 2D SWE as in Chapter 1, and combine with Crank-Nicolson scheme for calculating the Coriolis effect. Consider a rectangular space domain $\Omega := [0, L_x] \times [0, L_y]$ with solid wall boundaries. The domain is meshed with a recti-

CHAPTER 2

linear grid of $N_x \times N_y$ cells and here the cell of coordinates (x_i, y_j) is denoted by $K_{i,j}$. We set $\mathcal{M} := \{1, \dots, N_x\} \times \{1, \dots, N_y\}$. Let $\mathcal{E}_{int}^x := \{1, \dots, N_x - 1\} \times \{1, \dots, N_y\}$, $\mathcal{E}_b^x := \{0, N_x\} \times \{1, \dots, N_y\}$, $\mathcal{E}^x := \mathcal{E}_{int}^x \cup \mathcal{E}_b^x$, and $\tilde{\mathcal{E}}_{int}^x := \{1, \dots, N_x - 1\} \times \{0, \dots, N_y\}$. Let $\mathcal{E}_{int}^y := \{1, \dots, N_x\} \times \{1, \dots, N_y - 1\}$, $\mathcal{E}_b^y := \{1, \dots, N_x\} \times \{0, N_y\}$, $\mathcal{E}^y := \mathcal{E}_{int}^y \cup \mathcal{E}_b^y$, and $\tilde{\mathcal{E}}_{int}^y := \{0, \dots, N_x\} \times \{1, \dots, N_y - 1\}$. Water height h and topography z are calculated at cells $K_{i,j}$. For any time step t^n , approximation of h and z at point x_i, y_j are denoted as $h_{i,j}^n$ and $z_{i,j}^n$, respectively. Consider Figure 1.2, velocity u is discretized at the center of vertical edges at point $x_{i+\frac{1}{2}}, y_j$, while velocity v is discretized at the center of horizontal edges at point $x_i, y_{j+\frac{1}{2}}$, with notations $u_{i+\frac{1}{2},j}^n$ and $v_{i,j+\frac{1}{2}}^n$.

The approximation of mass conservation (2.1) at a cell $K_{i,j}$ is as follows Eq. (1.16). Approximation (1.16) is in fact the exact mass conservation in cell $K(i, j)$. When (1.16) is applied to the whole domain, to all $(i, j) \in \mathcal{M}$, the resulting approximation will conserve mass.

Approximation of the momentum balance (2.2, 2.3) are calculated by means of splitting, meaning that first we solve (2.2, 2.3) without the Coriolis terms,

$$\partial_t(hu) + \partial_x \left(hu^2 + \frac{1}{2}gh^2 \right) + \partial_y(huv) + gh\partial_x z = 0, \quad (2.13)$$

$$\partial_t(hv) + \partial_x(huv) + \partial_y \left(hv^2 + \frac{1}{2}gh^2 \right) + gh\partial_y z = 0, \quad (2.14)$$

and subsequently solve

$$d_t(hu) = +fhv, \quad (2.15)$$

$$d_t(hv) = -fhu. \quad (2.16)$$

The momentum balance (2.13) is approximated as in Eqs. (2.17),

$$\begin{aligned} h_{i+\frac{1}{2},j}^* u_{i+\frac{1}{2},j}^* - h_{i+\frac{1}{2},j}^n u_{i+\frac{1}{2},j}^n &+ \frac{\Delta t}{\Delta y} \left[q_{i+\frac{1}{2},j+\frac{1}{2}}^n \hat{u}_{i+\frac{1}{2},j+\frac{1}{2}}^n - q_{i+\frac{1}{2},j-\frac{1}{2}}^n \hat{u}_{i+\frac{1}{2},j-\frac{1}{2}}^n \right] \\ &+ \frac{\Delta t}{\Delta x} \left[(p_{i+1,j}^n \hat{u}_{i+1,j}^n - p_{i,j}^n \hat{u}_{i,j}^n) + \frac{1}{2}g((h_{i+1,j}^{n+1})^2 - (h_{i,j}^{n+1})^2) \right] \\ &+ \frac{\Delta t}{\Delta x} gh_{i+\frac{1}{2},j}^{n+1} (z_{i+1,j} - z_{i,j}) = 0, \quad \forall (i, j) \in \mathcal{E}_{int}^x, \end{aligned} \quad (2.17)$$

where $h_{i+\frac{1}{2},j}^n$, $p_{i,j}^n$, and $q_{i+\frac{1}{2},j+\frac{1}{2}}^n$ are defined as in (1.20), (1.21), and (1.22) respectively. In (2.17) the result is written with * to indicate that before moving to the next time step, it needs correction from the Coriolis terms.

The momentum balance in y -direction (2.14) is approximated similarly

$$\begin{aligned} h_{i,j+\frac{1}{2}}^* v_{i,j+\frac{1}{2}}^* - h_{i,j+\frac{1}{2}}^n v_{i,j+\frac{1}{2}}^n + \frac{\Delta t}{\Delta x} & \left[p_{i+\frac{1}{2},j+\frac{1}{2}}^n \hat{v}_{i+\frac{1}{2},j+\frac{1}{2}}^n - p_{i+\frac{1}{2},j-\frac{1}{2}}^n \hat{v}_{i+1/2,j-1/2}^n \right] \\ & + \frac{\Delta t}{\Delta y} \left[(q_{i,j+1}^n \hat{v}_{i,j+1}^n - q_{i,j}^n \hat{v}_{i,j}^n) + \frac{1}{2} g((h_{i,j+1}^{n+1})^2 - (h_{i,j}^{n+1})^2) \right] \\ & + \frac{\Delta t}{\Delta y} g h_{i,j+\frac{1}{2}}^{n+1} (z_{i,j+1} - z_{i,j}) = 0, \quad \forall (i,j) \in \mathcal{E}_{int}^y, \end{aligned} \quad (2.18)$$

where $h_{i,j+\frac{1}{2}}^n$, $q_{i,j}^n$, and $p_{i+\frac{1}{2},j+\frac{1}{2}}^n$, are defined as in (1.24), (1.25), and (1.26) respectively.

The next time step is correction to account for the Coriolis terms. Applying the Crank-Nicolson scheme analogous to (2.12) yield

$$\begin{aligned} h_{i+\frac{1}{2},j}^{n+1} u_{i+\frac{1}{2},j}^{n+1} = & \left[h_{i+\frac{1}{2},j}^* u_{i+\frac{1}{2},j}^* - 0.25\alpha^2 h_{i+\frac{1}{2},j}^* u_{i+\frac{1}{2},j}^* \right. \\ & \left. + \alpha h_{i+\frac{1}{2},j}^* v_{i+\frac{1}{2},j}^* \right] / (1 + 0.25\alpha^2), \quad \forall i \in \mathcal{E}_{int}^x, \end{aligned} \quad (2.19)$$

$$\begin{aligned} h_{i,j+\frac{1}{2}}^{n+1} v_{i,j+\frac{1}{2}}^{n+1} = & \left[h_{i,j+\frac{1}{2}}^* v_{i,j+\frac{1}{2}}^* - 0.25\alpha^2 h_{i,j+\frac{1}{2}}^* v_{i,j+\frac{1}{2}}^* \right. \\ & \left. - \alpha h_{i,j+\frac{1}{2}}^* u_{i,j+\frac{1}{2}}^* \right] / (1 + 0.25\alpha^2), \quad \forall i \in \mathcal{E}_{int}^y \end{aligned} \quad (2.20)$$

The above scheme is first-order accurate, with the CFL condition as in (1.27).

Recapitulating, the computational procedure holds for any time step t_n is as follows:

- Calculate h^{n+1} using mass conservation (1.16).
- Calculate $(hu)^*$ and $(hv)^*$ from the momentum balance (2.17),(2.18).
- Calculate $(hu)^{n+1}$ and $(hv)^{n+1}$ as corrections for $(hu)^*$ and $(hv)^*$ using (2.19) and (2.20).

2.3 Numerical implementations

In this section, we present numerical tests of the staggered conservative scheme for the 2D rotating SWE. We present simulations of Rossby wave, oscillation in a paraboloid, and Kelvin wave in coastal and equatorial area.

2.3.1 Rossby wave

For this simulation we use the one-and-a-half dimensional case of the rotating shallow water equations read as

$$\partial_t h + \partial_x(hu) = 0, \quad (2.21)$$

$$\partial_t(hu) + \partial_x\left(hu^2 + \frac{1}{2}gh^2\right) + ghz_x = fhv, \quad (2.22)$$

$$\partial_t(hv) + \partial_x(huv) = -fhu, \quad (2.23)$$

where t and x denotes respectively the time and space variables, h the water height, u and v the velocity in horizontal direction, g the gravitational constant, $z(x)$ the topography of the bottom, and $f(x)$ the Coriolis parameter. This test case is designed for simulating wave-breaking and shock phenomena and their influence on the adjustment of unbalanced jets, as discussed in [8].

For simulation, we take the initial conditions as in [51] and [8]. The computational domain is $\Omega = [-30 : 30]$. The number of space meshes used are $N_x = 2000$ points and Neumann boundary condition are used for left and right boundaries. Initial condition for water height and horizontal velocities are given by

$$h_{\text{ini}}(x) = H = \text{const} = 1, \quad u_{\text{ini}}(x) = 0, \quad v_{\text{ini}}(x) = VN_L(x),$$

where

$$N_L(x) = \frac{(1 + \tanh(4x/L + 2)) \cdot (1 - \tanh(4x/L - 2))}{(1 + \tanh(2))^2},$$

with V and L are the maximum zonal velocity and the width of the jet.

We use the Coriolis parameter $f = \pi$, that corresponds to Rossby deformation radius $R_d = \sqrt{gH}/f \approx 1$. The profile of the jet velocity in normalized form $v_{\text{ini}}(x)/V = N_L(x)$ is shown in Figure 2.3 (a). The resulting dynamic depends on the two non-dimensional parameters: the Rossby number $Ro^\alpha = \frac{V}{fL}$, and the Burger number $Bu^\alpha = \frac{gH}{f^2L^2}$.

According to [8], the fully nonlinear adjustment corresponds to $Ro^\alpha \approx 1$ and the natural time-scale is defined as $T_f = \frac{2\pi}{f}$. For computations we use parameters $Ro^\alpha = 1$ and $Bu^\alpha = 0.25$, and the result is shown in Figure 2.3 (b). The surface

wave breaks into two due to imbalance of momentum. Moreover, two shock waves rapidly formed at both wave fronts as expected.

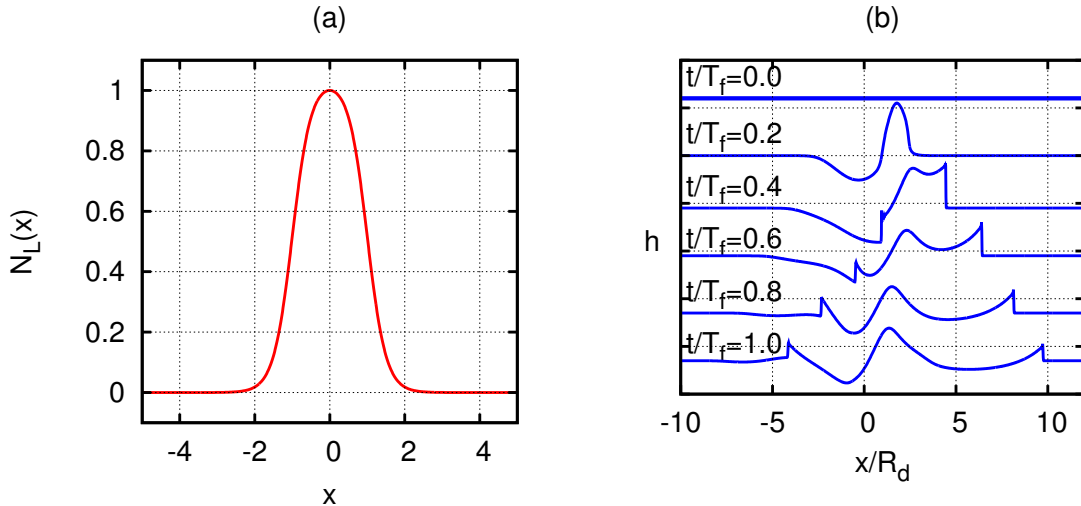


Figure 2.3: (a) The profile of $N_L(x)$. (b) The evolution of water height h in the Rossby adjustment for $Ro^\alpha = 1$ and $Bu^\alpha = 0.25$.

Comparison between the staggered and collocated grid are shown in Figure 2.4. Results from the staggered scheme and Suliciu scheme (or HLLC scheme which is used in [8]) are nicely confirmed. Hence, our staggered scheme is able to approximate the Coriolis term, and also to resolve waves with shock. However, our staggered scheme is much more simple and efficient.

2.3.2 Oscillation in a radially-symmetric paraboloid

Consider the staggered conservative scheme for the full equations (2.1-2.3). Here, the accuracy of our scheme is tested using the radially-symmetric paraboloid case that admit exact solution as recorded in [44]. In this test case, the water motion is periodic. Since the model is frictionless, this periodic motion will remain over infinitely long time.

On a computational domain $[0, 4] \times [0, 4]$, we adopt the paraboloid topography centered at (x_0, y_0) defined as

$$z(x, y) = -h_0(x - x_0)^2 - h_0(y - y_0)^2.$$

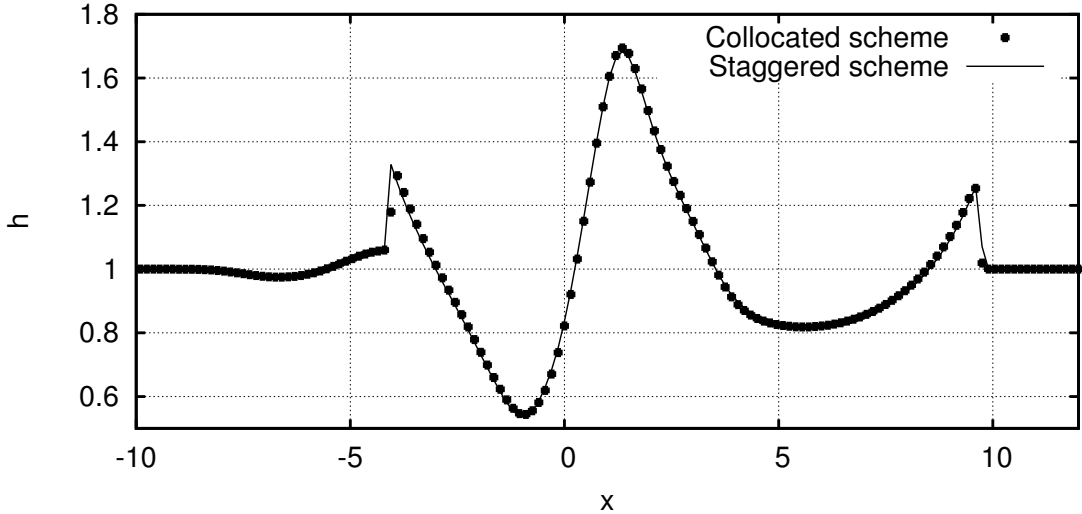


Figure 2.4: Water height h calculated using the staggered scheme and collocated finite volume in the Rossby adjustment for $Ro^\alpha = 1$ and $Bu^\alpha = 0.25$ at time $t/T_f = 1.0$.

And we implement the following initial conditions

$$\begin{aligned} h_{\text{ini}}(x, y) &= \max \left\{ 0, h_0 \left(-\frac{2A}{1-A} ((x-x_0)^2 - (y-y_0)^2) + \sqrt{\frac{1+A}{1-A}} - 1 \right) - z(x, y) \right\}, \\ u_{\text{ini}}(x, y) &= -\frac{f}{2(1-A)} (\sqrt{1-A^2} + A - 1) (y - y_0), \\ v_{\text{ini}}(x, y) &= \frac{f}{2(1-A)} (\sqrt{1-A^2} + A - 1) (x - x_0). \end{aligned}$$

For simulating this test case, our numerical scheme should be able to accommodate wet/dry transition correctly. Here, the wet/dry transition is accommodated simply by calculating hu and hv , only if $h > 0$ which means the corresponding cells still wet. When $h = 0$ then hu and hv are assigned to zero.

We conduct a computation using $\Delta x = \Delta y = 0.04$, $\Delta t = 0.005$ and we use $(x_0, y_0) = (2, 2)$, $g = 9.8$, with parameters $A = 0.22$, $h_0 = 0.1$, and Coriolis parameter $f = 0.05$. In Figure 2.5 the computational results are plotted together with analytical solutions from [44]. Clearly, they show a good agreement. Moreover, the numerical wave frequency confirm the analytical formula $\omega = \sqrt{2gh_0}$. Table of L^1 er-

rror and convergence rate of the staggered scheme are shown in Table 2.1 and Figure 2.6, respectively. From Figure 2.6, we can see that the staggered scheme converges to the analytical solution as the number of grid points increases.

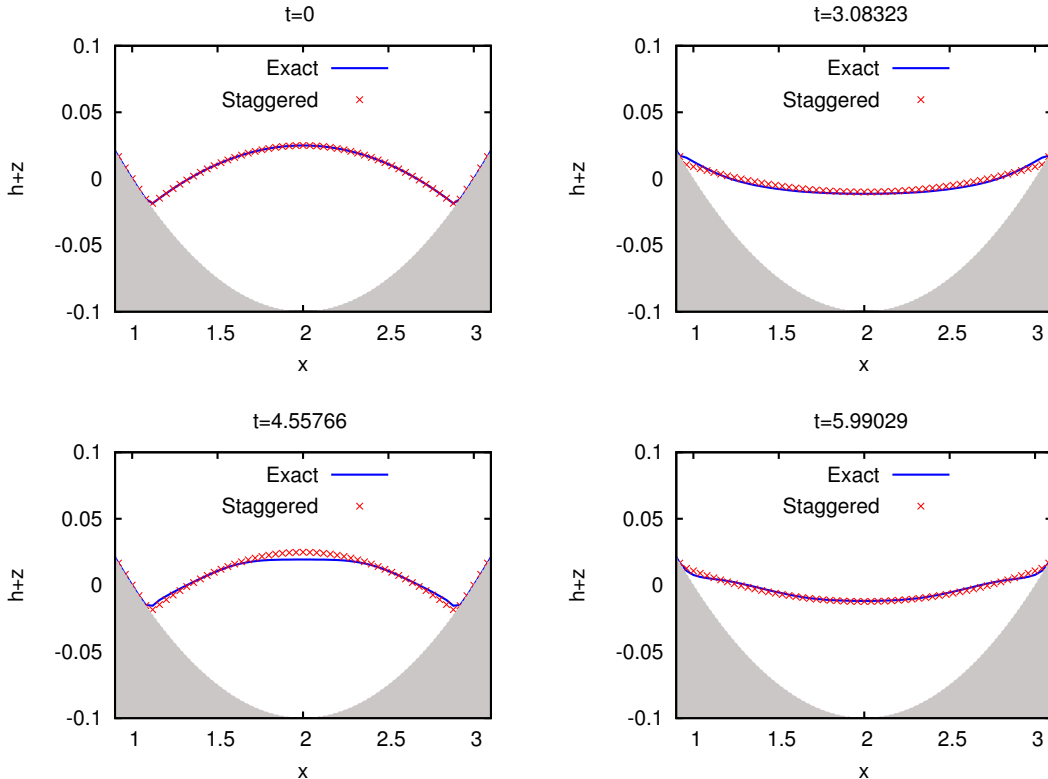


Figure 2.5: The cross-sectional water surface at subsequent times. The computational results (cross) and exact solutions (lines). The grey area indicates the paraboloid topography.

2.3.3 Coastal Kelvin wave

Next, we perform simulation of coastal Kelvin wave introduced in [28]. Consider the full equations (2.1)-(2.3) in a computational domain $\Omega = [0 : 400] \times [0 : 100]$ km. The grid spacing are $\Delta x = \Delta y = 2$ km in x and y -directions respectively. Initially, water height is $h_{\text{ini}}(x, y) = 10$ m with zero initial velocity. The Coriolis parameter is $f = +5 \times 10^{-4}$ s⁻¹, that corresponds to Rossby deformation radius $R_d \approx 20$ km. The final time of our simulation is $T = 10.6$ hours with $\Delta t = 2$ s. The wave paddle is located at $(x = 24, y = 4)$ km, that produce a monochromatic wave with

Cells	
$N_x \times N_y$	$\ Error\ _{L^1}$
50×50	3.477E-2
100×100	1.492E-2
200×200	6.780E-3
400×400	3.592E-3
800×800	2.046E-3

Table 2.1: The L^1 error in radially-symmetric paraboloid test at time $T = 3\frac{2\pi}{\omega}$.

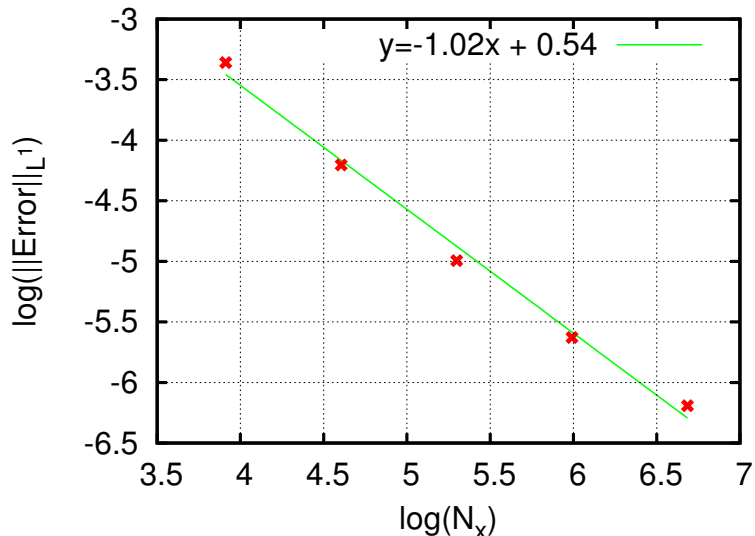


Figure 2.6: The convergence rate of the staggered scheme for several number of grid points $N_x (= N_y)$.

amplitude 1 m and period 2 hours. Hard wall boundary is implemented along $y = 0$ and transparent boundaries along $x = 0$, $x = L_x$ and $y = L_y$.

Figure 2.7 and 2.8 present the calculated surface waves in 3D view and contours plots, respectively. We clearly see the main feature of Kelvin wave. It is a non-dispersive wave, in which the wave retains its shape in the alongshore direction over time. Moreover, due to Coriolis force, the wave amplitude decay exponentially in the offshore direction, with the maximal amplitude attained along the shoreline.

Simulation results presented in 3D view and surface wave contours are shown in Figure 2.7 and Figure 2.8, respectively. In Figure 2.7 and 2.8, we clearly see the effect of Coriolis force. Both results in Figure 2.7 (b) and 2.8 (b) show that the coastal Kelvin wave reaches maximal amplitude along the coast. As we expect, these simulations display the feature of Kelvin wave, a non-dispersive wave, i.e. the wave retains its shape in the alongshore direction over time.

During simulation, we calculate the relative entropy $\frac{\eta}{\eta|_{t=0}}$ as a function of time, where η is given in (2.5). The resulting entropy curve as given in Figure 2.9 is nearly constant. This is to be expected since our simulation produce relatively smooth solutions. This observation indicates that our numerical scheme satisfies entropy stability.

2.3.4 Equatorial Kelvin waves

Cushman-Roisin and Beckers [13] describes perturbation wave in equatorial area produce some type of waves such as, Kelvin waves, mixed waves, and some planetary waves. These waves are symmetric with respect to the equator. The short wavelength Kelvin waves carry energy eastward direction, whereas the long wavelength planetary waves carry energy to westward direction. Since there is no Coriolis force along the equator, currents cannot be preserved in the geostrophic balance, and hence dynamical waves are different between tropical and non-tropical regions. Here, the beta-plane approximation to the Coriolis force is used, in which $f = \beta y$, where y is the distance from the equator, and β is the variation of the Coriolis parameter.

In this section, the numerical simulation of equatorial Kelvin wave will be presented. The domain of this simulation is $\Omega = [-25 : 25] \times [-25 : 25]$ km. The initial conditions of water height is a linear bell-shaped Kelvin wave (taken from [20]) and

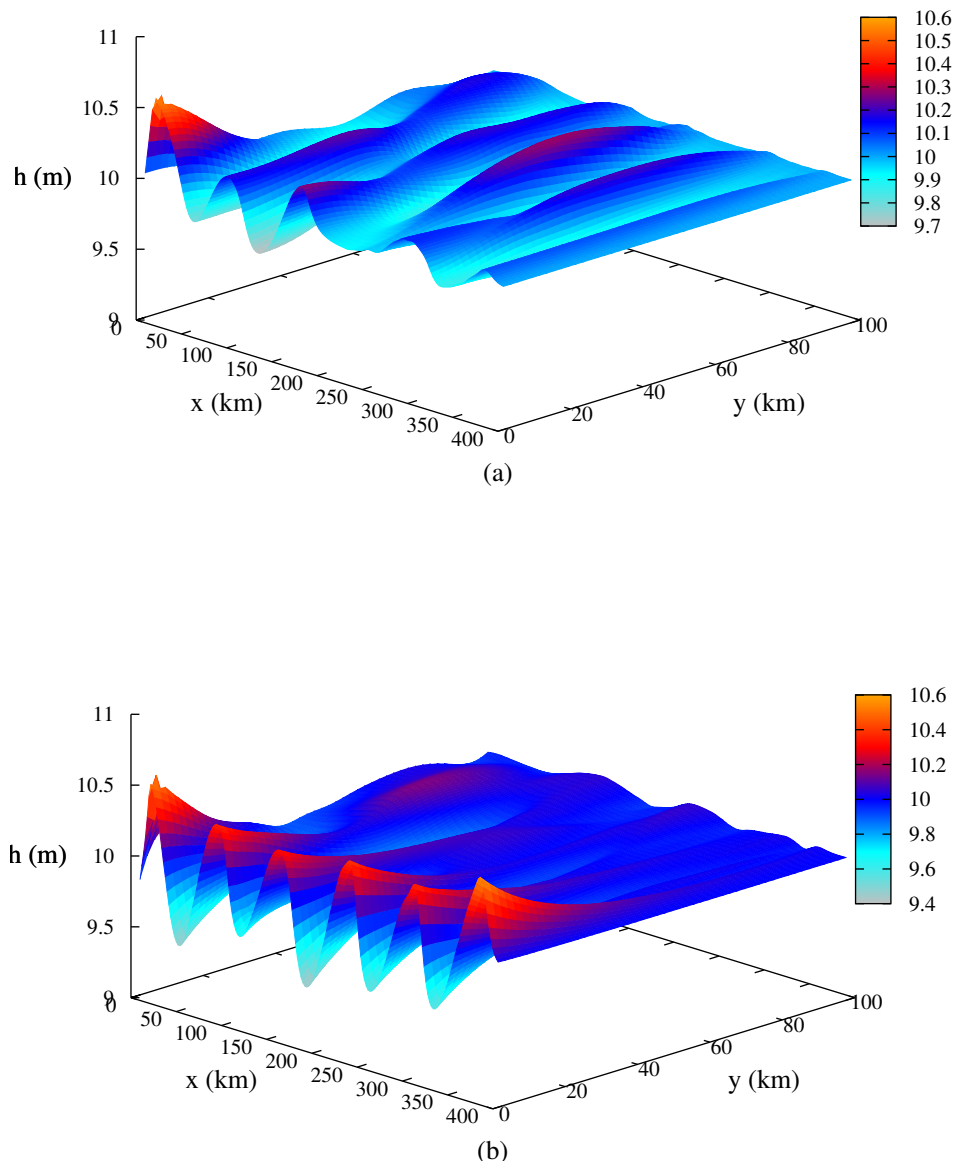


Figure 2.7: Wave trapped along the coast $y = 0$ at time $t = 10.6$ hours. (a) Numerical simulation without Coriolis force. (b) Numerical simulation with Coriolis force.

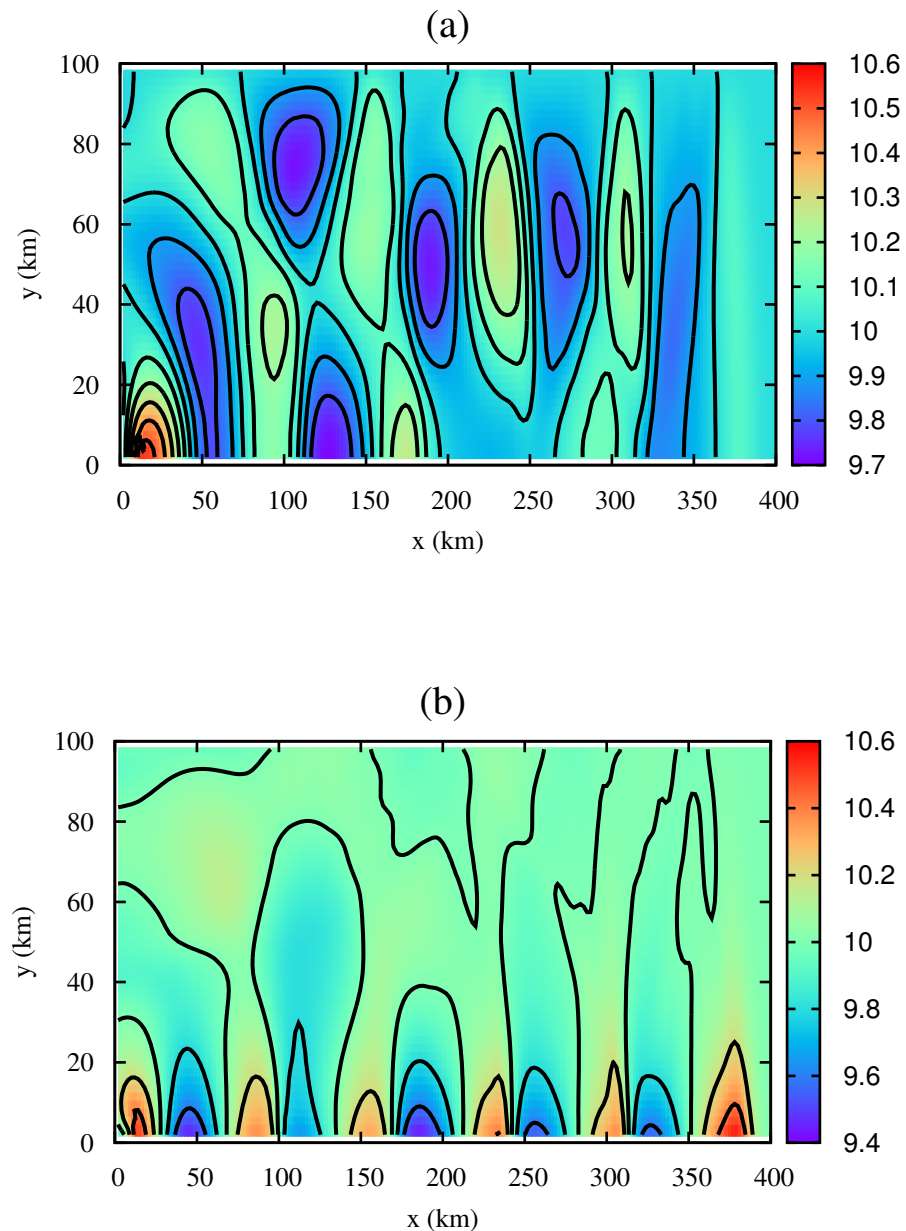


Figure 2.8: Surface wave contours at final time $t = 10.6$ hours. (a) Without Coriolis force and (b) with Coriolis force.

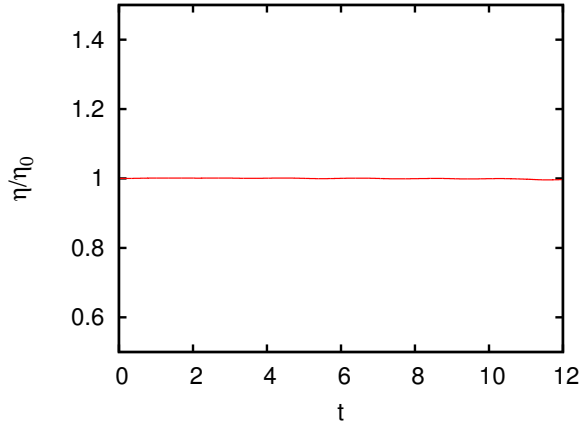


Figure 2.9: The relative entropy $\frac{\eta}{\eta|_{t=0}}$ as a function of time for Coastal Kelvin wave simulation.

velocity is set to be zero in all direction, to yield

$$h_{\text{ini}}(x, y) = 1 + A \exp \left(-\frac{y^2}{2} - \frac{x^2}{2q^2} \right),$$

$$u_{\text{ini}}(x, y) = 0, \quad v_{\text{ini}}(x, y) = 0,$$

where q is the aspect ratio of the equatorial length of the disturbance to its width. Parameters of this simulation are $q \approx 3$, $A = 0.2$, $\beta = 1.0$, $g = 1.0$ and boundary conditions are set to be solid wall.

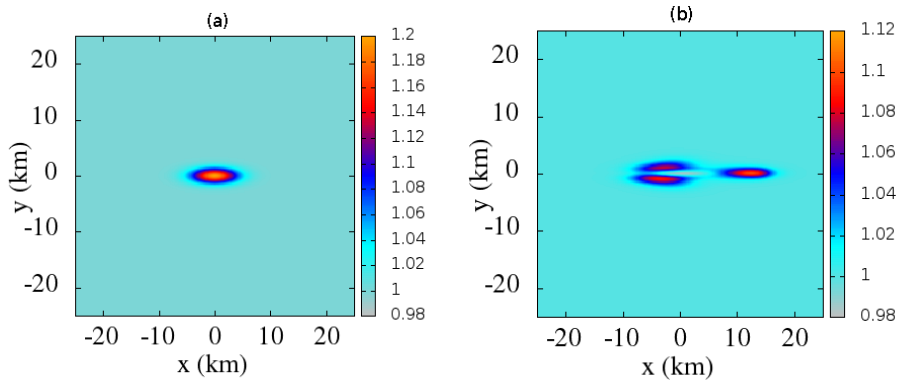


Figure 2.10: The equator Kelvin wave. (a) The water contour profile at time $t = 0$. (b) The water contour profile at time $t = 25$.

As we can see from Figure 2.10, the Coriolis force near the equator generates three

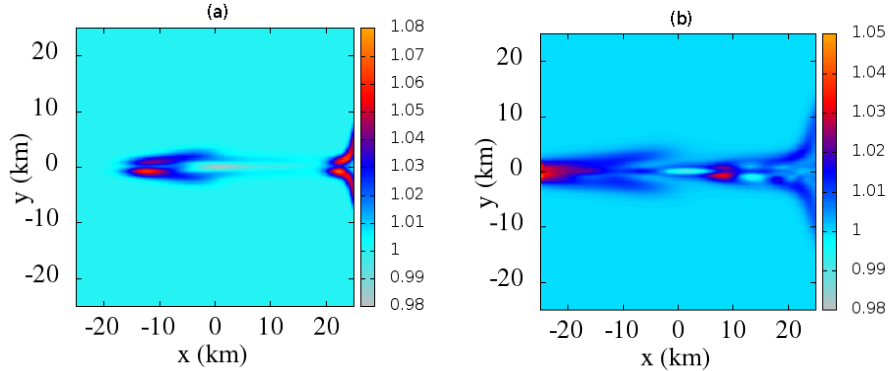


Figure 2.11: The continuation of equator Kelvin wave. (a) Surface contour profile at time $t = 74$. (b) Surface contour profile at time $t = 212$.

waves separated from the initial position. The larger Kelvin wave moves eastwards, and two smaller planetary waves move westwards. Our result shows similar profile as simulation by [13].

Further observation, when these waves have arrived at the boundaries there arise reflection waves. Figure 2.11 shows the contour profiles of wave reflections at two different times $t = 74$ and $t = 212$. In reality, this phenomena can be observed in several occasions such as, wave around island, equator current induced by winds, El Niño phenomena, etc. Similar with the previous simulation, the entropy curve for this equatorial Kelvin wave simulation is also constant, and again confirm the entropy stability of our staggered conservative scheme.

2.4 Conclusion

We have implemented the staggered momentum conservative scheme for solving the rotating 2D shallow water equations. Numerical simulation of Rossby wave has shown a good agreement with result from the conservative Suliciu method. For the test case of waves oscillating in a paraboloid topography, our simulation confirm the exact solution. In the simulations of coastal and equatorial Kelvin waves, the entropy is shown to be conserved. For all simulations above, no special treatment are needed, and this indicates the robustness of our staggered conservative scheme.

CHAPTER 2

Numerical study of staggered scheme for viscous Saint-Venant equations³

This chapter describes a numerical scheme for approximate the viscous Saint-Venant equations. This scheme is called staggered grid scheme which is a robust, simple and straightforward scheme for viscous Saint-Venant equations. Some numerical simulations have been elaborated to validate the accuracy of the scheme, such as the calculation of the convergence rate L^1 -norm error of the scheme, the comparison of viscous and classical Saint-Venant equations, comparison of staggered scheme with kinetic scheme and direct Navier-Stokes approach in dam-break problem and simulation of dry-wet problem. The results show good accuracy and in a good agreement with another scheme in another paper.

3.1 Introduction

The Saint-Venant equations (SVE) or known as shallow water equations are a set of hyperbolic partial differential equations which consist of two equations, mass conservation and momentum conservation. This equation is very important to describe some fluid flow phenomenon such as, the water flow in channels or rivers, the sediment flow in estuaries, the gas flow in the atmosphere and etc (see [48]).

In this chapter, we are interested to study the numerical scheme for viscous SVE in the laminar flow water model. This model was derived by Gerbeau and Perthame [23] which includes a friction and viscosity. The equations of one-dimensional viscous

³This chapter has been published as: Putu Harry Gunawan. "Numerical study of staggered scheme for viscous Saint-Venant equations". In: Applied Mathematical Sciences, Vol. 8, 2014, no. 108, 5349-5359, <http://dx.doi.org/10.12988/ams.2014.47580>.

SVE are given as

$$\partial_t h + \partial_x(hu) = 0, \quad (3.1)$$

$$\partial_t(hu) + \partial_x\left(hu^2 + \frac{1}{2}gh^2\right) + gh\partial_x z = -\kappa_{vsv}(h)u + 4\mu\partial_x(h\partial_x u), \quad (3.2)$$

$$\kappa_{vsv}(h) = \frac{\kappa}{1 + \frac{\kappa h}{3\mu}}, \quad (3.3)$$

where h , u and z are the water height, the lateral velocity and the topography respectively. The gravitational force is define by g , and the constants κ and μ are the friction and viscosity coefficient respectively.

In order to approximate equations (3.1 - 3.3), some methods have been proposed. For instance, in [23] they used the finite volume kinetic scheme introduced by [2]. However, here we are interested using the finite volume staggered grid scheme for viscous SVE. This scheme is known as a robust and well-balanced scheme for classical SVE (1.1 - 1.2) (see in Chapter 1 or [16, 25, 26] for the analysis of mathematical properties, i.e. consistency, stability, entropy satisfying, and see [16, 41, 42, 34] for the applications). Hence, in this chapter we propose to construct and study the staggered scheme for viscous SVE.

The outline of this chapter is given as, in Section 3.2, the numerical staggered scheme for viscous SVE is constructed. The numerical validation such as comparison of classical and viscous SVE in dam-break simulation and the convergence rate of discrete L^1 -norm error in various grid points are given in Section 3.3. Moreover, the comparison of staggered, kinetic and Navier-Stokes scheme in laminar dam-break wet bed problem and also the study of dry-wet problem are examined. Finally in Section 3.4, the conclusions are organized.

3.2 Numerical scheme

Follow the notations in Chapter 1, the discretization of mass conservation equation (3.1) is given as in (1.6). The momentum balance equation (3.2) is discretized as in (1.2) with an additional a second-order central difference for the viscosity term,

reads

$$\begin{aligned} \frac{h_{i+\frac{1}{2}}^{n+1} u_{i+\frac{1}{2}}^{n+1} - h_{i+\frac{1}{2}}^n u_{i+\frac{1}{2}}^n}{\Delta t} + \frac{1}{\Delta x} & \left[q_{i+1}^n \hat{u}_{i+1}^n - q_i^n \hat{u}_i^n + \frac{1}{2} g \left((h_{i+1}^{n+1})^2 - (h_i^{n+1})^2 \right) \right. \\ & \left. + g h_{i+\frac{1}{2}}^{n+1} (z_{i+1}^0 - z_i^0) \right] + \kappa_{\text{vsv}} (h_{i+\frac{1}{2}}^{n+1}) u^{n+1} - 4\mu \frac{1}{\Delta x} & \left[h_{i+1}^{n+1} \frac{(u_{i+\frac{3}{2}}^n - u_{i+\frac{1}{2}}^n)}{\Delta x} \right. \\ & \left. - h_i^{n+1} \frac{(u_{i+\frac{1}{2}}^n - u_{i-\frac{1}{2}}^n)}{\Delta x} \right] = 0, \quad \forall i \in \mathcal{E}_{int}, \quad (3.4) \end{aligned}$$

where

$$\kappa_{\text{vsv}} (h_{i+\frac{1}{2}}^{n+1}) := \frac{\kappa}{\left(1 + \frac{\kappa h_{i+\frac{1}{2}}^{n+1}}{3\mu} \right)}. \quad (3.5)$$

Finally, the general algorithm is given in Algorithm 1.

Algorithm 1 The explicit staggered scheme.

Step 1. Give the initial conditions at $n = 0$.

Step 2. Compute (1.7) for $q_{i+\frac{1}{2}}^n \forall i \in \mathcal{E}_{int}$.

Step 3. Compute (1.10) for Δt to preserve the stability.

Step 4. Solve (1.6) for $h_i^{n+1} \forall i \in \mathcal{M}$.

Step 5. Solve (3.4) for $h_{i+\frac{1}{2}}^{n+1} u_{i+\frac{1}{2}}^{n+1} \forall i \in \mathcal{E}_{int}$ and immediately we can get $u_{i+\frac{1}{2}}^{n+1}$.

3.3 Numerical tests

In this section, we elaborate two numerical tests such as dam-break on a wet and dry bed simulations.

3.3.1 Dam-break on a wet bed

In this simulation, first we will examine the comparison between classical and viscous SVE. Here the domain is $\Omega = [-50 : 50]$ ($L = 100$ m length) and the initial

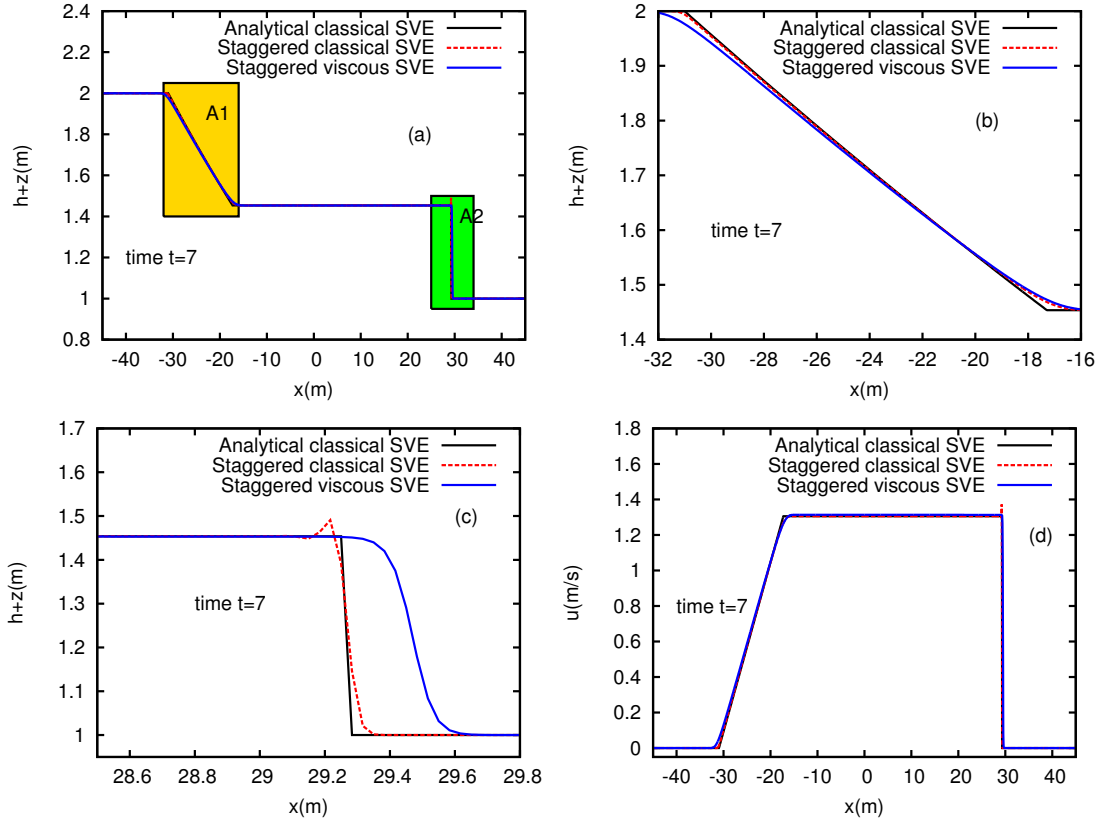


Figure 3.1: Dam-break on a wet bed. (a) The comparison of water level profile on full domain.(b) The zoom area of (A1) on the rarefaction wave. (c) The zoom area of (A2) on the shock wave. (d) The velocity profile on full domain. The CFL condition is 1 and final time $t = 7$ s.

conditions are given as

$$h_{\text{ini}}(x) = \begin{cases} h_l & \text{if } x \leq 0 \\ h_r & \text{otherwise} \end{cases}, \quad (3.6)$$

$$z_{\text{ini}}(x) = 0, \quad (3.7)$$

$$u_{\text{ini}}(x) = 0, \quad (3.8)$$

where $h_l = 2$, $h_r = 1$, the boundary conditions are set to be wall in the both boundaries and the CFL condition is set to be 1. For the viscous SVE, the coefficients of friction and viscosity term are given as $\kappa = 0$ and $\mu = \frac{h_l - h_r}{L}$ respectively.

In Figure 3.1, the results of water level and velocity are shown at final time $t = 7$ s. Figure 3.1(b) and 3.1(c) show the zoom part of Figure 3.1(a) in rarefaction

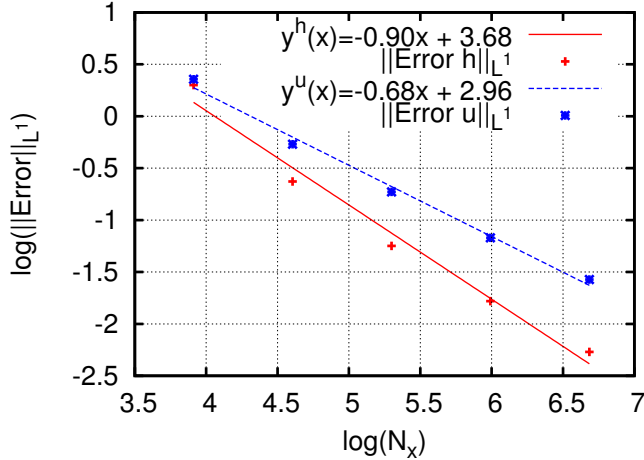


Figure 3.2: The convergence rate of discrete L^1 -norm error of h and u in various grid points N_x . The functions $y^h(x)$ and $y^u(x)$ are obtained from data fitting of L^1 -norm error of h and u respectively using the nonlinear least-squares method.

(A1) and shock (A2) waves of water level respectively. We can see clearly that, in the shock area, the numerical result in viscous SVE is more diffusive thus the oscillation in shock area vanished. Contrary, the staggered scheme for classical SVE in dam-break simulation produces small bump in the shock area (which is not due to numerical instability), however it is more accurate than the other robust methods (see [16] for more illustrations and explanations). Moreover, we can confirm that the shock speed in viscous SVE is faster than the classical SVE. On the other hand, in rarefaction wave and intermediate depth are quite similar in both cases.

In this test case, there is no analytical solution for dam-break in viscous SVE. Therefore, in order to evaluate the accuracy of the scheme, we used a reference solution. Here, a reference solution is computed by using a very fine mesh of 3200 grid points. The convergence rate of L^1 -norm error both in h and u , in various grid points N_x are shown in Figure 3.2. We can observe that, in Figure 3.2 the convergence of our scheme ameliorates along with the increasing of numbers of grid points as we expected.

Next, it will be interesting if we elaborate our scheme into a numerical simulation of viscous dam-break introduced in [27, 23]. Here, we will compare the results of our scheme with the results of kinetic scheme (see [2]) and direct Navier-stokes obtained in [23]. In this simulation, the domain and the initial conditions are given as in

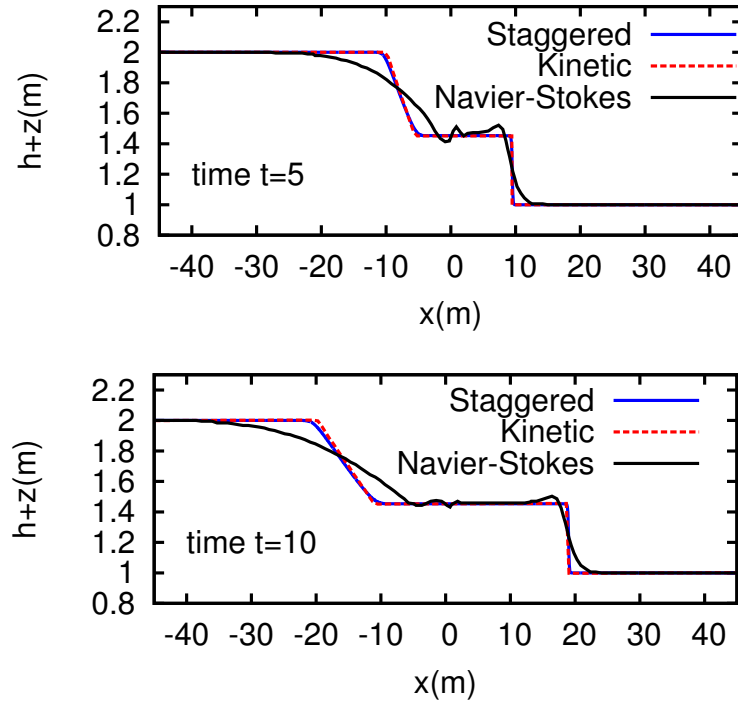


Figure 3.3: Dam-break viscous SVE. The series of water level $h + z$ profiles at final times $t = 5$ s and $t = 10$ s.

the previous simulation. However, in order to get the same simulation in [23], the gravitational force and two final time steps are modified as $g = 2 \text{ m/s}^2$, $t = 5 \text{ s}$ and $t = 10 \text{ s}$.

The results of these simulation are shown in Figure 3.3. They show that our scheme is comparable with the kinetic scheme for viscous SVE. In addition, comparing with the result using direct Navier-Stokes in Figure 3.3, all schemes have a same shock speed and intermediate water depth. The comparison of the intermediate water depth in various values of κ is shown in Figure 3.4. They show that the given of various κ produce difference profiles.

3.3.2 Dam-break on a dry bed

The aim of this simulation is not only to examine the ability of the scheme to handle vacuum, but also to confirm the ability to deduct non-smooth topography. Here the

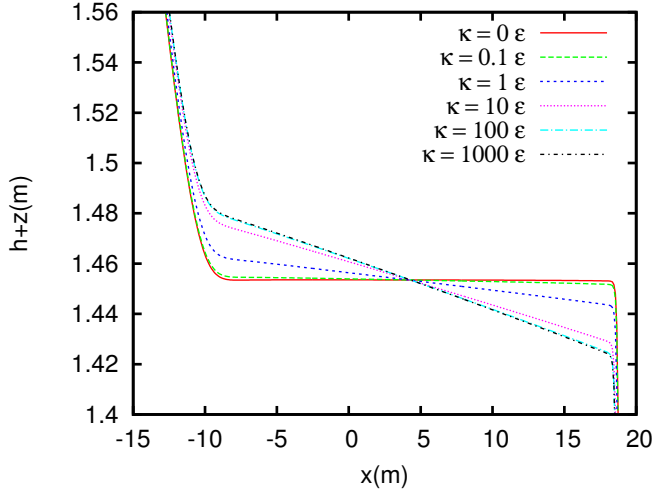


Figure 3.4: Dam-break on a wet bed of viscous SVE. The comparison of the intermediate water level $h + z$ profiles with various κ where $\epsilon = \frac{h_l - h_r}{L}$.

domain is $\Omega = [-50 : 50]$ m and the initial conditions are given as

$$z_{\text{ini}}(x) = \begin{cases} 1 & \text{if } -30 < x < -20 \\ 0.2(x - 20) & \text{if } x > 20 \\ 0. & \text{otherwise} \end{cases}, \quad (3.9)$$

$$(h + z)_{\text{ini}}(x) = \begin{cases} \max(2, z_{\text{ini}}(x)) & \text{if } x \leq 0 \\ \max(1, z_{\text{ini}}(x)) & \text{otherwise} \end{cases}, \quad (3.10)$$

$$u_{\text{ini}}(x) = 0. \quad (3.11)$$

The boundary conditions are set to be zero at the end of left and right domain. The CFL condition is used is 1 and the coefficients of friction and viscosity are given as $\kappa = 10\epsilon$ and $\mu = \epsilon$ respectively with $\epsilon = \frac{h_l - h_r}{L}$. Results from various final time steps ($t = 0$, $t = 13$, $t = 20$ and $t = 30$) are shown in Figure 3.5. Here, we can see clearly that the scheme is perfectly able to treat dry-wet transitions and also to handle the non-smooth topography. Moreover, we also can confirm that our scheme produces the waves over the jumps of topography.

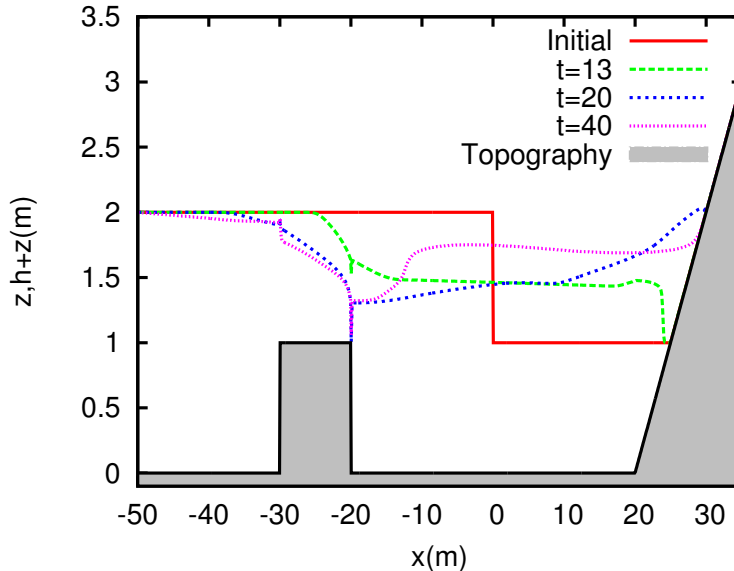


Figure 3.5: Dam-break on a dry bed of viscous SVE. The comparison of water level $h + z$ profiles with various final time steps.

3.4 Conclusion

The staggered grid scheme for viscous Saint-Venant equations has been presented. This scheme is simple, accurate and straightforward both for viscous and classical Saint-Venant equations. The good convergence rate of discrete L^1 -norm error in h and u are shown nicely increasing along with the increasing number of points. Some comparison results from other schemes are elaborated in dam-break problem. They have a good agreement with the another results using kinetic scheme and direct Navier-Stokes approach. Moreover, through the simulation of dam-break on a dry bed, we can confirm that our scheme is able to handle vacuum and non-smooth topography. Finally, we can conclude that staggered grid scheme is a robust scheme for viscous SVE.

PART II

Related Models

Explicit staggered grid scheme for the Exner - shallow water equations⁴

The staggered numerical scheme is shown to be a robust and simple method for approximating the coupled system Exner - shallow water equations for bedload sediment modelling. Numerical tests show good convergence properties to an analytical solution and match pretty well experimental data in the case of dam break with erodible bottom. The cases of subcritical steady flow over a bump and transcritical flow over a bump are presented, showing the robustness of the scheme and its interest for engineering applications.

4.1 Introduction

According to [40], there are two perspectives in the study of the interaction between surface flow and the dynamics of sediment transport. On one hand, we can study the influence of bed change on the flow dynamics (see. e.g., [10, 50]). On the other hand, we can investigate the morphological bed change and sedimentary deposits due to the flow dynamics (see e.g., [4, 11]).

In this chapter, following the second perspective, we consider the numerical simulation of the coupled system of Exner and shallow water equations. This coupled model consists of three equations: fluid mass conservation, fluid momentum conservation and the Exner equation which prescribes the mass conservation of sediment in interaction with the fluid flow. We use the finite volume method for approximating the shallow water equations. In this method, two approaches are classically

⁴This chapter has been submitted as: P. H. Gunawan, R. Eymard and S. R. Pudjaprasetya.
"Explicit staggered grid scheme for the Exner - shallow water equations", 2014.

available. In the collocated approach, all the unknown variables are computed at the same grid points and numerical fluxes are computed with an approximate Riemann solver [7, 30, 45].

However, the approximation of the coupled model Exner - shallow water equations using the collocated method shows some difficulties, as depicted in [11]. Indeed, we show in Figure 4.1 the spurious oscillations which are appearing in relation with the hyperbolicity of the system (better results seem to be obtained using the coupled Roe scheme [11] or the coupled relaxation scheme [4]).

We use here the staggered approach. In this method, the water height and the velocity are approximated into different grids [1]. The advantage for engineering applications is that this method leads to a quite simple implementation, and seems to be robust in the case of rapidly varying flows. We refer to Chapter 1 or [16, 26, 25] for its mathematical analysis (in these papers, it is shown that it preserves the positivity of the water height, the consistency, and that it satisfies an entropy criterion). In [42, 41, 34, 16] are given various numerical tests over fixed bed in one and two dimensions. We turn in this chapter to the case of a moveable bed.

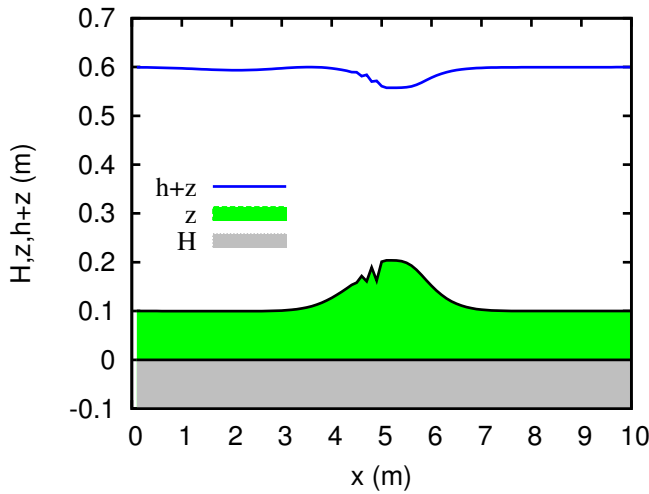


Figure 4.1: The unstable appearance using collocated splitting method in moveable subcritical steady state simulation at final time $t = 2.6$ with. This simulation used HLLC (Harten-Lax-van Leer-Contact) solver (see [7, 45] for more details about HLLC solver). The CFL condition for this simulation is set to be $\nu = 0.5$.

This chapter is organized as follows. The coupled model is described in Section 4.2 in the one dimensional case. The description of the staggered conservative scheme

is presented in Section 4.3. Numerical simulations, concerning comparisons with an analytical solution and experimental data in the case of the one dimensional erodible dam break, subcritical steady state over a moveable bump, and transcritical flow over a granular bump, are presented in Section 4.4. Finally, some conclusions are drawn in Section 4.5.

4.2 The Exner - shallow water model

The coupled shallow water – Exner equations are given in the one dimensional case by

$$\partial_t h + \partial_x(hu) = 0 \quad (4.1)$$

$$\partial_t(hu) + \partial_x\left(hu^2 + \frac{1}{2}gh^2\right) + gh\partial_x(z - H) + ghS_f = 0 \quad (4.2)$$

$$\partial_t z + \xi\partial_x Q_s = 0 \quad (4.3)$$

where h is the total water depth, u the velocity in the x direction, z the bed elevation, g the gravity acceleration, Q_s the sediment discharge (or bedload) and H the depth of fixed bedrock layer to the reference level (see Figure 4.2). The coefficient ξ is computed by $\xi = (1 - \phi)^{-1}$, where ϕ is the bed sediment porosity. The source term S_f , which is a friction term, depends on the type of flow.

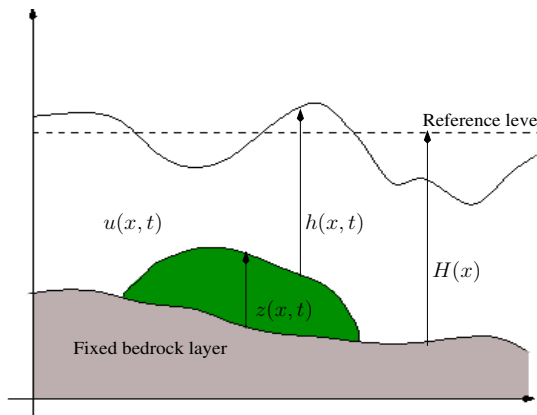


Figure 4.2: The one-dimensional sketch of shallow water with a sediment layer.

Let us review some of the most used empirical formulas for the bedload Q_s .

1. *Grass formula:*

CHAPTER 4

This formula is proposed by Grass [24] for the solid transport discharge:

$$Q_s = A_g |u|^{m-1} u, \quad (4.4)$$

where $0 \leq A_g \leq 1$ and $1 \leq m \leq 4$ are tuned on the experimental data. The value $m = 3$ is currently used, and strong interaction between fluid and sediment is simulated letting A_g be close to 1.

2. Meyer-Peter and Müller's formula:

Meyer-Peter and Müller's formula [31] is given by

$$Q_s = \operatorname{sgn}(u) 8(\tau_* - \tau_{*c})^{3/2} \sqrt{(\phi_r - 1)gd^3}, \quad (4.5)$$

where d is the size of sediment grain, $\phi_r = \rho_s/\rho_w$ is the relative density of the sediment, letting ρ_w and ρ_s be the respective densities of the fluid and sediment, τ_* is the non-dimensional shear stress and τ_{*c} is the non-dimensional critical shear stress (see [9] for more details). The non-dimensional shear stress τ_* is defined by

$$\tau_* = \frac{\tau}{g(\rho_s - \rho_w)d}, \quad (4.6)$$

where $\tau = \gamma R_h |S_f|$ is the shear stress, $R_h \approx h$ is the hydraulic ratio and S_f is the friction term, which depends on the flow condition. When the flow is laminar, Manning's friction law is often used:

$$S_f = \frac{k^2 u |u|}{h^{4/3}}. \quad (4.7)$$

where k is Manning's roughness coefficient. On the other hand, when the flow is turbulent, Darcy-Weisbach's friction law may be used:

$$S_f = \frac{f u |u|}{8gh}, \quad (4.8)$$

where the Darcy-Weisbach friction factor f may depend on the Reynolds number. In this chapter, f and k will be kept constant.

3. Van Rijn's formula:

Van Rijn's formula ([47, 39]) for the sediment discharge is given by

$$Q_s = \frac{5 \times 10^{-3}}{C_d^{1.7}} \left(\frac{d}{h} \right)^{0.2} \tau_*^{0.5} (\tau_*^{0.5} - \tau_{*c}^{0.5})^{2.4} \sqrt{(\phi_r - 1)gd^3}, \quad (4.9)$$

where C_d is called the drag coefficient, and the other variables are defined as in (4.5).

4.3 Description of the numerical schemes

4.3.1 1D staggered finite volume scheme

Following the notations in Chapter 1, the time interval $(0, T)$ is divided into N_t time steps of length Δt and, for all $n \in \{0, \dots, N_t\}$, $t^n := n\Delta t$. The domain $\Omega := (0, L)$ is divided into N_x cells of length Δx . The left end, the center and the right end of the i -th cell are respectively denoted by $x_{i-\frac{1}{2}}$, x_i and $x_{i+\frac{1}{2}}$. We set $\mathcal{M} := \{1, \dots, N_x\}$, $\mathcal{E}_{int} := \{1, \dots, N_x - 1\}$, $\mathcal{E}_b := \{0, N_x\}$, and $\mathcal{E} := \mathcal{E}_{int} \cup \mathcal{E}_b$.

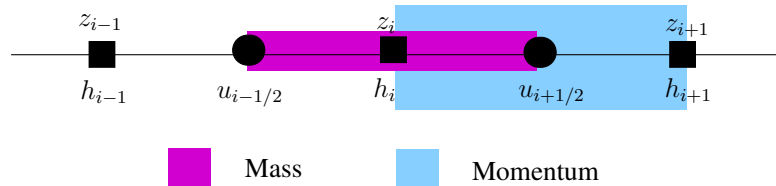


Figure 4.3: The one-dimensional staggered grids. The magenta area represents the control volume for the mass conservations, associated with unknowns h_i and z_i . The control volume for the momentum conservation (unknown $u_{i+\frac{1}{2}}$) is shown by the blue area.

The water height h and the sediment layer z are discretized at the center of the cells. The approximation of h (resp. z) at the point x_i and at time t^n is denoted by h_i^n (resp. z_i^n). The velocity u is discretized at the interfaces between the cells. The approximation of u at the point $x_{i+\frac{1}{2}}$ and at time t^n is denoted by $u_{i+\frac{1}{2}}^n$. This space discretization is shown in Figure 4.3.

CHAPTER 4

First, we prescribe the initial conditions by,

$$h_i^0 = \frac{1}{\Delta x} \int_{x_{i-\frac{1}{2}}}^{x_{i+\frac{1}{2}}} h_0(x) \, dx, \quad \forall i \in \mathcal{M}, \quad (4.10)$$

$$z_i^0 = \frac{1}{\Delta x} \int_{x_{i-\frac{1}{2}}}^{x_{i+\frac{1}{2}}} z_0(x) \, dx, \quad \forall i \in \mathcal{M}, \quad (4.11)$$

$$u_{i+\frac{1}{2}}^0 = \frac{1}{\Delta x} \int_{x_i}^{x_{i+1}} u_0(x) \, dx, \quad \forall i \in \mathcal{E}_{int}. \quad (4.12)$$

The water conservation equation (4.1) is discretized as in (1.6-1.7). The momentum balance equation (4.2) is discretized as (1.33) or (1.34) depends on friction term S_f , reads

$$\begin{aligned} h_{i+\frac{1}{2}}^{n+1} u_{i+\frac{1}{2}}^{n+1} - h_{i+\frac{1}{2}}^n u_{i+\frac{1}{2}}^n + \frac{\Delta t}{\Delta x} \left[q_{i+1}^n \hat{u}_{i+1}^n - q_i^n \hat{u}_i^n + \frac{1}{2} g \left((h_{i+1}^{n+1})^2 - (h_i^{n+1})^2 \right) + g h_{i+\frac{1}{2}}^{n+1} (z_{i+1}^n - z_i^n) \right. \\ \left. - g h_{i+\frac{1}{2}}^{n+1} (H_{i+1} - H_i) \right] + \Delta t S_{fi+1/2}^n = 0, \quad \forall i \in \mathcal{E}_{int}, \end{aligned} \quad (4.13)$$

The term $S_{fi+1/2}^n$ is given in the case of Manning's friction (see (4.7)) by

$$S_{fi+1/2}^n = \frac{k^2 |u_{i+\frac{1}{2}}^n| u_{i+\frac{1}{2}}^{n+1}}{\left(h_{i+\frac{1}{2}}^{n+1} \right)^{4/3}}, \quad (4.14)$$

and in the case of Darcy-Weisbach's friction (see (4.8)) by

$$S_{fi+1/2}^n = \frac{f |u_{i+\frac{1}{2}}^n| u_{i+\frac{1}{2}}^{n+1}}{8 g h_{i+\frac{1}{2}}^{n+1}}. \quad (4.15)$$

Finally the discretization of Exner equation (4.3) is given by

$$z_i^{n+1} - z_i^n + \frac{\Delta t}{\Delta x} \xi \left(Q_{i+\frac{1}{2}}^{n+1} - Q_{i-\frac{1}{2}}^{n+1} \right) = 0, \quad \forall i \in \mathcal{M}. \quad (4.16)$$

where $Q_{i+\frac{1}{2}}^{n+1} = Q_s(h_{i+\frac{1}{2}}^{n+1}, u_{i+\frac{1}{2}}^{n+1})$.

Let us conclude this section by gathering all the above information into Algorithm 2.

Algorithm 2 The explicit staggered scheme.

Step 1. Give the initial conditions at $n = 0$.

Step 2. Compute Δt from (1.10).

Step 3. Compute $(h_i^{n+1})_{i \in \mathcal{M}}$ from (1.6).

Step 4. Compute $(h_{i+\frac{1}{2}}^{n+1} u_{i+\frac{1}{2}}^{n+1})_{i \in \mathcal{E}_{int}}$ from (4.13), and update $u_{i+\frac{1}{2}}^{n+1}$.

Step 5. Compute $(z_i^{n+1})_{i \in \mathcal{M}}$ from (4.16).

4.4 Numerical tests

In this section, we will give some numerical tests such as comparison between numerical computation and the analytical solution, some comparisons of dam break simulation over a granular bed and experimental data, subcritical steady state and transcritical flow over a moveable bump. In these tests, the depth of bedrock to the reference level H is set to be constant ($\partial_x H = 0$).

4.4.1 Analytical solution

To show the performance and numerical convergence rate of the above scheme, here we consider a simple test where the analytical solution exist in literature, see [5]. In this simulation we consider the Grass formula $Q_s = A_g u |u|^{m-1}$ with $A_g = 0.005$ and $m = 3$. The initial conditions are given by:

$$\begin{aligned} (hu)_{\text{ini}}(x) &= 1, \\ u_{\text{ini}}(x) &= \left[\frac{\alpha x + \beta}{A_g} \right]^{1/3}, \\ h_{\text{ini}}(x) &= \frac{(hu)_{\text{ini}}(x)}{u_{\text{ini}}(x)}, \\ z_{\text{ini}}(x) &= 1 - \frac{u_{\text{ini}}^3(x) + 2g(hu)_{\text{ini}}^2(x)}{2gu_{\text{ini}}(x)}, \end{aligned}$$

where the coefficients are given by $\alpha = \beta = 0.005$. In this simulation, we let the friction term vanish $S_f = 0$ and we prescribe the CFL number $\nu = 1$.

In Figure 4.4, we can see that the analytical solution seems to be well approximated even with a coarse grid. This is not observed in [4], where the relaxation scheme is quite diffusive for coarse grids, which leads to results far from the analyt-

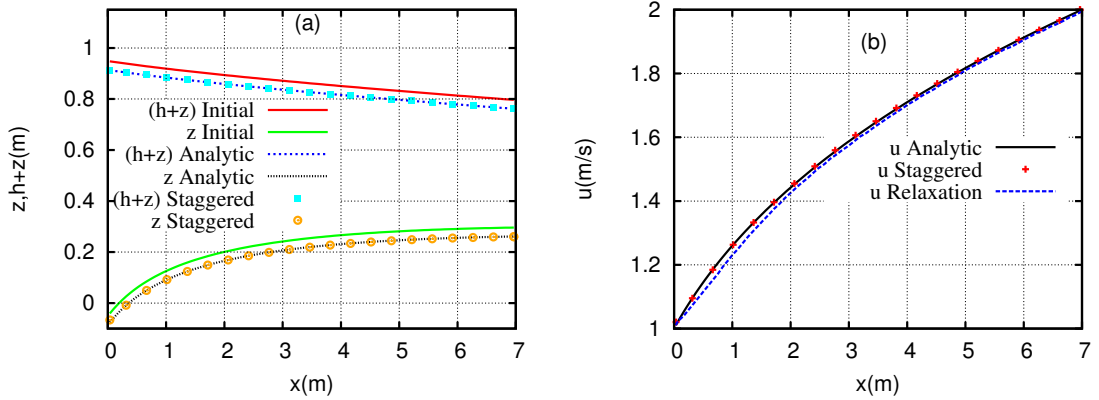


Figure 4.4: Analytical solution. Comparison between analytical and numerical solutions of (a) the water level and sediment profile, (b) the velocity profile at the final time $t = 7$.

Cells	$\ h - h_{\text{analytic}}\ _{L^1}$	τ	$\ u - u_{\text{analytic}}\ _{L^1}$	τ	$\ z - z_{\text{analytic}}\ _{L^1}$	τ
50	6.082E-3	/	1.941E-2	/	5.875E-3	/
100	3.666E-3	0.752	1.257E-2	0.670	2.979E-3	0.973
200	2.092E-3	0.809	7.072E-3	0.829	1.507E-3	0.982
400	1.143E-3	0.872	3.776E-3	0.905	7.596E-4	0.988
800	6.054E-4	0.916	1.952E-3	0.951	3.814E-4	0.993

Table 4.1: L^1 error of staggered scheme at $t = 7$.

ical solution. In Figure 4.4 (b), we see that our scheme (with $N_x = 100$) provides a closer velocity profile to the analytical solution than the relaxation scheme with the same grid, as provided by [5]. Table 4.1 shows the discrete L^1 -norm of the error for h , u and z at the final time step. This discrete L^1 -norm is computed by summing the differences with the analytical solution at the discretization points for h , u , or z , multiplied by the space step.

Table 4.1 provides the numerical convergence to the analytical solution as the number of points is increasing. Since our scheme has accuracy of order one, these rates tends to one as expected. It turns out that our scheme can produce stable results that confirm the analytical solution, which is calculated using the CFL number $\nu = 1$ by the stability condition (1.10). This is quite surprising since according to Cordier et al., [11], the CFL condition for Exner-shallow water equations is more restricted than the CFL condition for full shallow water equations. However, Audusse

et al., [4] propose a relaxation system of Exner-shallow water equations which has the same CFL condition as the full shallow water equations. Therefore, through several computations of Exner-shallow water equations, our staggered scheme is shown stable under the same CFL condition for full shallow water equations as defined in (1.10).

4.4.2 One-dimensional erodible dam break

Comparison with literature

This section is devoted to the numerical simulation of a one-dimensional erodible dam break, as introduced by [4]. The domain is given by $\Omega = [0 : 10]$ with a dam located at the middle of the domain. The dam separates two initial water heights $h_{\text{ini}}(x) = 2$ at the left side and $h_{\text{ini}}(x) = 1.25 \times 10^{-1}$ at the right side of the domain. Initially, the sediment load is $z_{\text{ini}}(x) = 0$, and fluid velocity is set to zero, and no friction term is introduced. The grid includes 400 points, and the final time is given by $t = 1$.

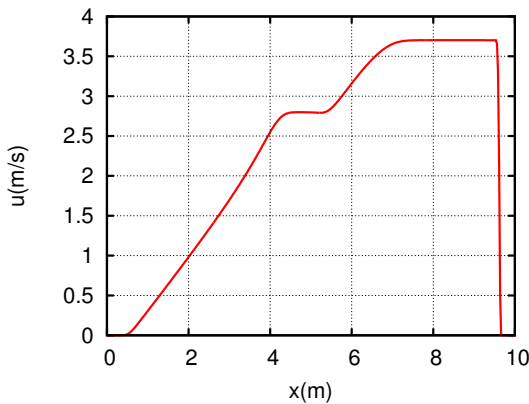


Figure 4.5: One-dimensional erodible dam break. Velocity profile at final time $t = 1$. In this simulation we used the Grass formula with $A_g = 5 \times 10^{-3}$ and $m = 3$.

Figure 4.5 and 4.6 show the velocity, the water level and the sediment profiles at the final time $t = 1$. We can see that in Figure 4.6 (b) the hydraulic jump arises in the water level profile around the initial dam site and it propagates upstream. This results are in agreement with the results given by [4].

Comparison with experimental data

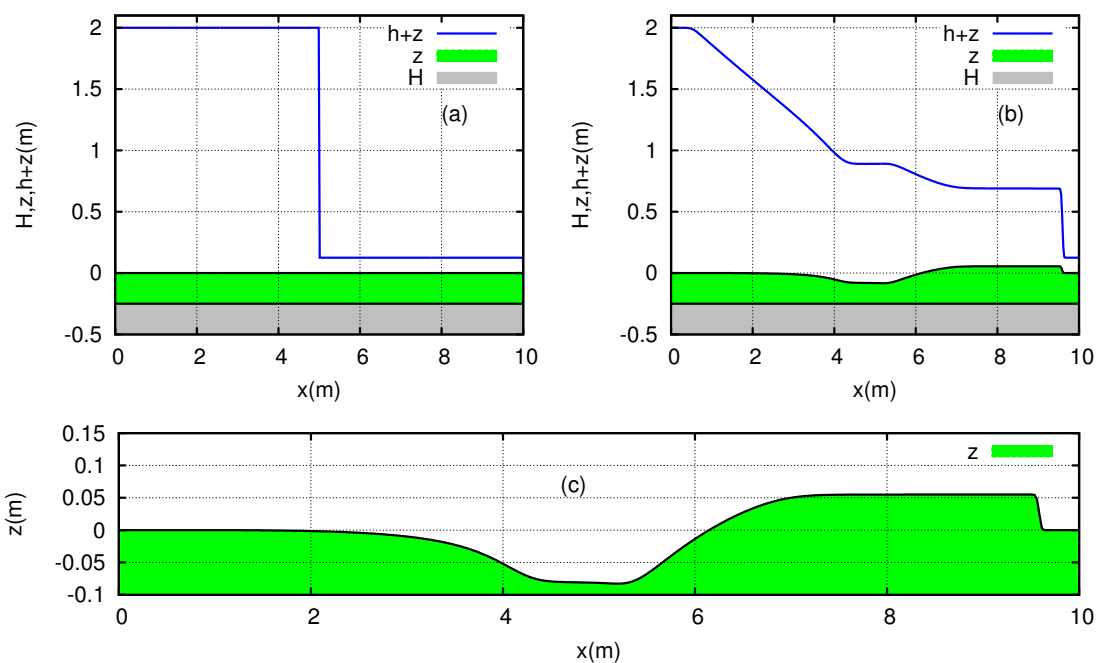


Figure 4.6: One-dimensional erodible dam break. (a) Initial position of dam break problem. (b) Water level $h + z$ and sediment z profiles at final time $t = 1$. (c) Zoom area of sediment profile at final time $t = 1$. In this simulation we used the Grass formula with $A_g = 5 \times 10^{-3}$ and $m = 3$.

CHAPTER 4

Let us now consider the comparison between numerical computations and experimental data. Some laboratory experiments in dam break over a granular bed have been reported, see for instance by [50]. We focus on the experiments performed in Louvain-la-Neuve, Université Catholique de Louvain by [21]. In these experiments, the characteristics of the sediment (i.e diameter of sediment, porosity, etc.) have been carefully prescribed.

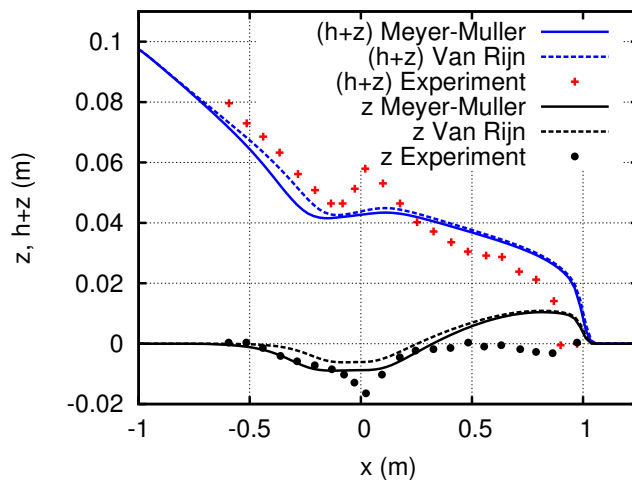


Figure 4.7: Dam-break over a granular bed. Comparison between numerical computations and experimental data. The calculated water level and sediment profiles at final time $t = 10t_0$, $t_0 = \sqrt{gh_0} \approx 0.101$ with bedload following Meyer-peter & Müller's (4.5) and Van Rijn's (4.9) formulas.

Here, we compare two sediment discharge Meyer-peter-Müller-(4.5) and Van Rijn-(4.9) formulas. The domain of this simulation is $\Omega = [-1.25 : 1.25]$, and the initial conditions of this simulation are given by

$$h_{\text{ini}}(x) = \begin{cases} 0.1 & \text{if } x < 0. \\ 0 & \text{otherwise} \end{cases},$$

$$u_{\text{ini}}(x) = 0,$$

$$z_{\text{ini}}(x) = 0.$$

The characteristics of the sediment are selected following [50], the sediment porosity is given by $\phi = 0.3$, with diameter $d = 3.2 \times 10^{-3}$, and density $\rho_s = 1,540$. Manning's coefficients for water and sediment are 0.001 and 0.03, respectively. In

CHAPTER 4

Van Rijn's formula, drag coefficient is set to $C_d = 1 \times 10^{-3}$. The CFL condition for this simulation is set to $\nu = 1$.

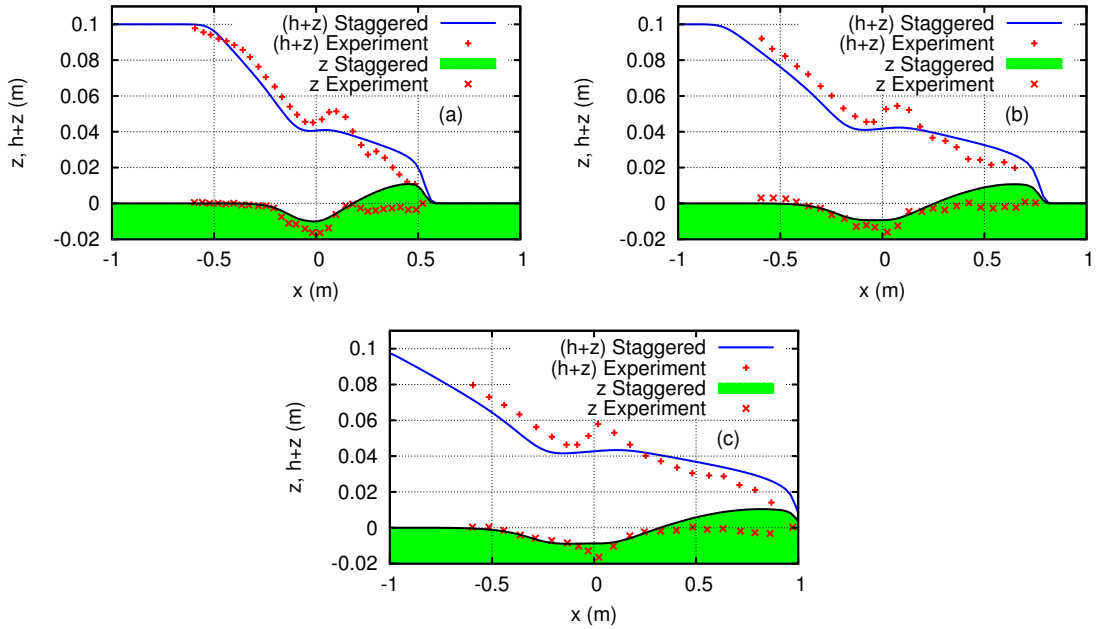


Figure 4.8: Dam-break over a granular bed. Comparison between numerical computations and experimental data of the water level and sediment at subsequent times (a) $t = 5t_0$, (b) $t = 7.5t_0$ and (d) $t = 10t_0$ with $t_0 = \sqrt{gh_0} \approx 0.101$. Meyer-Peter & Müller's formula (4.5) is used in this computation.

The water level and sediment profiles at time $t = 10t_0$ with $t_0 = \sqrt{gh_0} \approx 0.101$ resulting from Meyer-Peter & Müller's (4.5) and Van Rijn's (4.9) formula are shown in Figure 4.7. We observe that the water level is better approximated using Van Rijn's formula whereas the sediment is better with Meyer-peter & Müller's formula. These two discharge formulas only differ by the factor C_d , however this lead to obviously different results around initial dam site. This shows the importance of the characterization of the sediment properties.

Results at different times are presented in Fig 4.8. They show a good agreement between the numerical computation and the experimental data with respect to the water level and sediment profiles.

4.4.3 Subcritical steady state over a moveable bump

This test case is discussed in [11]. We consider as initial condition a subcritical steady state for the shallow water system given by

$$\begin{aligned}(hu)_{\text{ini}}(x) &= 0.5, \\ z_{\text{ini}}(x) &= 0.1 + 0.1e^{-(x-5)^2}, \\ \frac{(hu_{\text{ini}}(x))^2}{2h_{\text{ini}}^2(x)} + g(h_{\text{ini}}(x) + z_{\text{ini}}(x)) &= 6.386,\end{aligned}$$

over a domain $\Omega = [0 : 10]$. The initial profile of water surface and the sediment bed are shown in Figure 4.9 (a). We let the sediment to evolve under the above steady state initial condition. For sediment discharge we use the Grass bedload flux with $m = 3$. The water surface and sediment profiles at the final time $t = 10$ obtained with $A_g = 5 \times 10^{-3}$ (resp. at $t = 2.6$ with $A_g = 7 \times 10^{-2}$) are shown in Figure 4.9 (b) (resp. 4.9 (c)).

The results are in good agreement with corresponding results on [11]. Moreover, our scheme is stable also for CFL number close to the maximum value $\nu = 1$.

4.4.4 Transcritical flow over a granular bump

We now consider the case of movable sediment under transcritical flow, following [11]. The domain of this simulation is $\Omega = [0 : 10]$ and the Grass formula with $m = 3$ is used for the sediment discharge. The initial configuration are

$$\begin{aligned}z_{\text{ini}}(x) &= 0.1 + 0.1e^{-(x-5)^2}, \\ (hu)_{\text{ini}}(x) &= 0.6, \\ (h + z)_{\text{ini}}(x) &= 0.4,\end{aligned}$$

with the left boundary condition $(hu)(0, t) = 0.6$ and free flux for the right boundary. This simulation is conducted in two steps. First, without sediment flux $A_g = 0$ (see Figure 4.10), and we let the above initial condition to reach a steady state. In the second step, we let the sediment to evolve, by setting $A_g = 5 \times 10^{-4}$.

Results at different times are shown in Figure 4.11: after a long enough time of simulation, the sediment profile and the water surface are getting flat. Cordier et al. noted in [11] that this test case involves negative eigenvalues of the system in

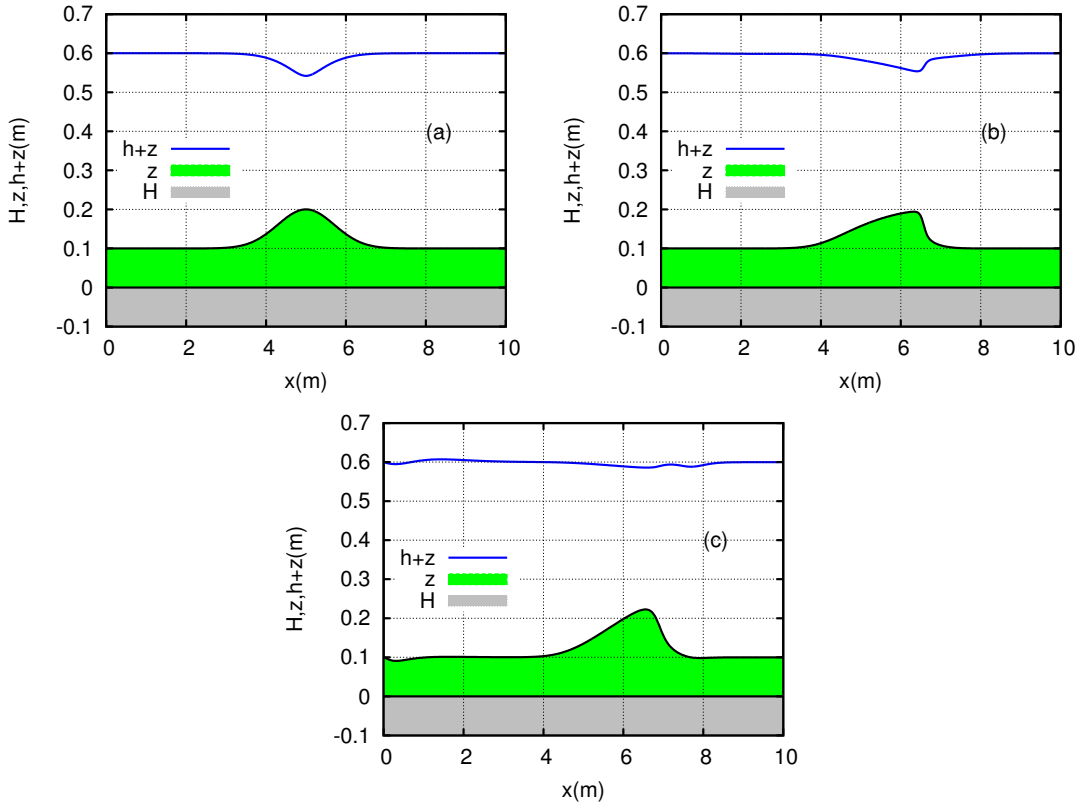


Figure 4.9: Subcritical steady state over a moveable bump. Simulations with sediment discharge of Grass formula with $m = 3$, calculated using 400 mesh points. The profiles of free surface $h + z$ and sediment z (a) at initial time, (b) at time $t = 10$, with parameter $A_g = 5 \times 10^{-3}$, (c) at time $t = 2.6$ with parameter $A_g = 7 \times 10^{-2}$.

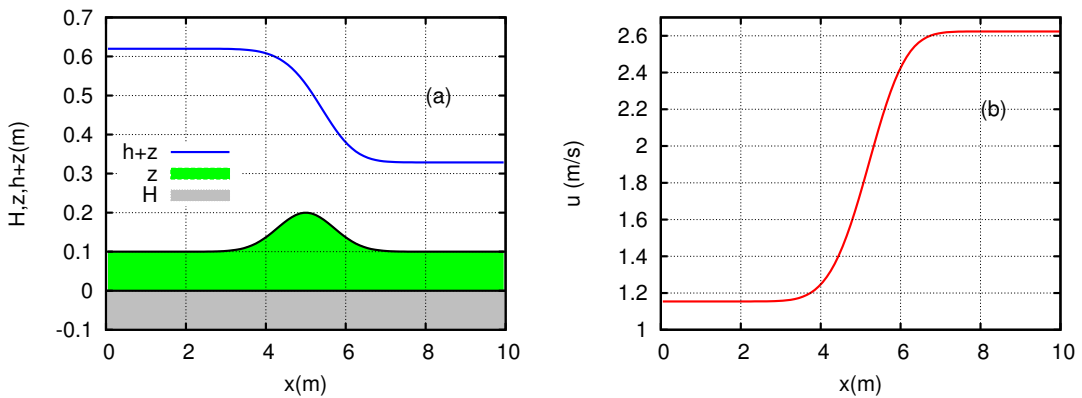


Figure 4.10: Transcritical flow over a granular bump. (a) The water level and sediment, and (b) the velocity profile in steady state.

supercritical region, which are not easy to handle. We show here that our scheme can handle this problem, even when parameters used for computations correspond to a CFL number that is close to the maximum value $\nu = 1$.

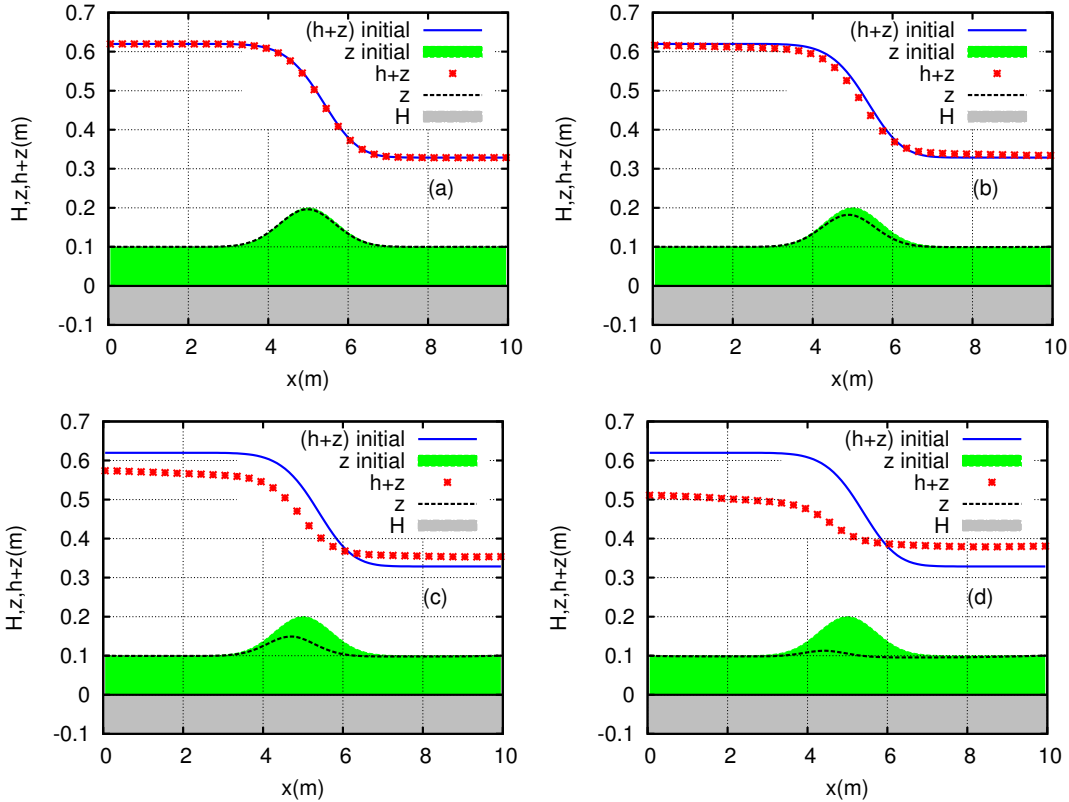


Figure 4.11: Transcritical flow over a granular bump. Water level and sediment profiles with $A_g = 5 \times 10^{-4}$ at times (a) $t=1$, (b) $t=5$, (c) $t=15$ and (d) $t=30$.

4.5 Conclusion

We have presented in this chapter an explicit staggered scheme for the simulation of the coupled system Exner - shallow water equations, in the one-dimensional case only. Several numerical tests seem to validate the robustness of the scheme. Satisfactory convergence properties to an analytical solution (the convergence rate tends to 1 in L^1 -norm since first order scheme is applied) and good agreement with experimental data are obtained. Moreover, robustness properties have been exhibited in the case of transcritical flow. These observations enhance the interest of this scheme for engineering purposes.

CHAPTER 4

Shear shallow water flows model by Richard-Gavrilyuk Model

The aim of this chapter is to design a finite volume scheme (collocated) for the Richard-Gavrilyuk model. This model is a shallow water model including shear and turbulence effects. Several numerical simulations related to sheer shallow water using standard shallow water equations and Richard-Gavrilyuk model are presented. Moreover in the runup solitary wave simulation, the results from both models show match pretty well with experimental data.

5.1 Introduction

The shear shallow water flow is used to describe the strong hydraulic jump phenomena. This phenomena is related to the larger of Froude numbers. For instance, we can imagine the problem of the unstable of water surface shown an inclined plane. The profile of this surface is called roll waves which is the hydraulic jump in a periodic system separated by smooth profiles. Conventionally, this phenomena is based on the standard shallow water equation or the Saint-Venant equations. In one dimension, the standard shallow water model (with Darcy-Weisbach friction) reads

$$\partial_t h + \partial_x(hu) = 0, \quad (5.1)$$

$$\partial_t(hu) + \partial_x \left(hu^2 + \frac{1}{2}gh^2 \right) = -gh\partial_x z - C_f u|u|, \quad (5.2)$$

where t denotes the time variable, x the space variable, h the water height, u the velocity, g the gravitational constant, z the topography of the bottom, and C_f a friction coefficient. However as recorded in [38], this model is not able to provide the information related to the hydraulic jump such as the length of hydraulic jump or the roller length. Moreover, they can only be found by experimentally.

CHAPTER 5

A shallow water model including shear and turbulence effects has been proposed recently by G. Richard and S. Gavrilyuk [38, 37]. This shear shallow water model is obtained by taking into account the fluctuation of the horizontal velocity along the vertical direction. In other words, the Richard-Gavrilyuk model is an extension of the standard shallow water model, involving some additional unknowns, the roller enstrophy Φ , and two additional parameters, the wall enstrophy ϕ_0 and the roller drag coefficient C_r . In one dimension of space (where the wall enstrophy ϕ_0 is set to be a constant) the equations of the model are,

$$\partial_t h + \partial_x(hu) = 0, \quad (5.3)$$

$$\partial_t(hu) + \partial_x(hu^2 + p) = -gh\partial_x z - C_f u|u|, \quad (5.4)$$

$$\partial_t(h(u^2/2 + e)) + \partial_x((h(u^2/2 + e) + p)u) = \left(-gh\partial_x z - \left(C_f + \frac{\Phi}{\phi_0 + \Phi}C_r\right)u|u|\right)u, \quad (5.5)$$

where

$$p = \frac{1}{2}gh^2 + (\phi_0 + \Phi)h^3, \quad (5.6)$$

$$e = \frac{1}{2}gh + \frac{1}{2}(\phi_0 + \Phi)h^2. \quad (5.7)$$

The Richard-Gavrilyuk model is similar to the fully Euler equation where shear and turbulence effects are involved in the internal energy balance (5.5). In order to discretize (5.3-5.5), the idea is to design a numerical scheme similar to discretize the full Euler equation. In a finite volume scheme, there are two methods proposed to approximate the fully Euler equation. The first method is the collocated scheme using HLLC (Harten-Lax-van Leer-Contact) solver or Suliciu solver which is given by F. Bouchut [7]. This scheme is a robust scheme for the shock capture phenomena in the full Euler equations (full gas dynamics). The second method is called the explicit staggered scheme for the full Euler equations which is introduced in [26, 32]. Nevertheless, this scheme is not straightforward as for approximating the standard shallow water (in Chapter 1) and the barotropic Euler equations (in [26, 32]). The correction term in the discretization of the internal energy balance appears to recover a consistent discretization of the total energy balance (see [26, 32]).

In this chapter we only consider the collocated scheme with the HLLC solver or Suliciu solver for approximating the Richard-Gavrilyuk model. Therefore, the aims of this chapter are to design a collocated finite volume scheme for the Richard-Gavrilyuk model and also to present various numerical simulations using Richard-Gavrilyuk model together with those calculated using standard shallow water equations model.

5.2 Mathematical analysis of the model

Definition 1 (Conservative variable). *The variable $U(x, t) \in \mathbb{R}^p$ in which the system takes the conservative form*

$$\partial_t U + \partial_x (F(U)) = 0, \quad (5.8)$$

for some nonlinearity F that takes values in \mathbb{R}^p is called conservative variable. The system (5.8) is also called system of conservation laws.

For instance, the conservative part of system (5.3 - 5.5) can be written as a system of conservation laws

$$\partial_t V + \partial_x (F(V)) = 0, \quad (5.9)$$

with the conservative variables

$$V = \begin{pmatrix} h \\ hu \\ h(u^2/2 + e) \end{pmatrix}, \quad (5.10)$$

and the nonlinearity function

$$F = \begin{pmatrix} hu \\ hu^2 + p \\ (h(u^2/2 + e) + p)u \end{pmatrix}, \quad (5.11)$$

where the total pressure p and the specific internal energy e are defined as (5.6) and (5.7) respectively.

CHAPTER 5

Proposition 5 (Hyperbolicity). *The conservative system (5.9) is hyperbolic. The eigenvalues of the system are $u - \sqrt{gh + 3(\phi_0 + \Phi)h^2}$, u and $u + \sqrt{gh + 3(\phi_0 + \Phi)h^2}$. The quantity $-h\Phi$ is a strictly convex (mathematical sense) entropy associated with the entropy flux $-hu\Phi$.*

Proof. Let $\tau = \frac{1}{h}$, then from (5.7) we can express Φ as a function of e and h :

$$\Phi(e, h) = \left(\frac{2e}{h^2} - g \frac{1}{h} \right) - \phi_0, \quad (5.12)$$

$$= (2e - g\tau)^2 - \phi_0. \quad (5.13)$$

Since ϕ_0 is a constant and corresponding the Gibbs identity we have

$$de + pd\tau = \frac{h^2}{2} d\Phi. \quad (5.14)$$

Thus the roller enstrophy Φ is analogous to the specific entropy s in the models of full gas dynamics (full Euler equations) [7]. As consequence of (5.9), the specific entropy is conserved along trajectories:

$$\partial_t \Phi + u \partial_x \Phi = 0. \quad (5.15)$$

Then, the equations (5.9) is hyperbolic with the characteristic speeds $u - a < u < u + a$ where a is the sound speed for the Euler equations. This sound speed is defined as

$$a^2 = -\tau^2 \frac{\partial p}{\partial \tau} \Big|_{\Phi=\text{const}}, \quad (5.16)$$

since

$$p = \frac{1}{2}g\tau^{-2} + \tau^{-3}(\phi_0 + \Phi), \quad (5.17)$$

we obtain

$$a^2 = gh + 3(\phi_0 + \Phi)h^2 > 0, \quad (5.18)$$

where the index ($\Phi = \text{const}$) at (5.16) means that the derivative is taken at Φ is constant.

Moreover, since we found that Φ is analogous to the specific entropy s in full gas dynamics, then by [edwige1996numerical] in Chapter 2, we can show that the quantity $-h\Phi$ is a strictly convex entropy associated with the entropy flux $-hu\Phi$. \square

5.3 Numerical scheme

The Richard-Gravrilyuk equations can be solved by a splitting method. This method is similar to discretize the Euler equations which is known as Strang's splitting method, can be found in Toro [45] for more detail. Here we discretize the equations by three steps. First, the conservative part of (5.3 - 5.5) is solved by Suliciu finite volume scheme (HLLC solver [7]):

$$\tilde{h}_i^{n+1} - h_i^n + \frac{\Delta t}{\Delta x_i} (F_{i+\frac{1}{2}}^h - F_{i-\frac{1}{2}}^h) = 0, \quad (5.19)$$

$$\tilde{h}_i^{n+1} \tilde{u}_i^{n+1} - h_i^n u_i^n + \frac{\Delta t}{\Delta x_i} (F_{i+\frac{1}{2}}^{hu} - F_{i-\frac{1}{2}}^{hu}) = 0, \quad (5.20)$$

$$\begin{aligned} \tilde{h}_i^{n+1} \left(\frac{1}{2} (\tilde{u}_i^{n+1})^2 + e(\tilde{h}_i^{n+1}, \tilde{\Phi}_i^{n+1}) \right) - h_i^n \left(\frac{1}{2} (u_i^n)^2 + e(h_i^n, \Phi_i^n) \right) \\ + \frac{\Delta t}{\Delta x_i} (F_{i+\frac{1}{2}}^{he} - F_{i-\frac{1}{2}}^{he}) = 0, \end{aligned} \quad (5.21)$$

where

$$e(h_i^n, \Phi_i^n) = \frac{1}{2} g h_i^n + \frac{1}{2} (\phi_0 + \Phi_i^n) (h_i^n)^2, \quad (5.22)$$

$$e(\tilde{h}_i^{n+1}, \tilde{\Phi}_i^{n+1}) = \frac{1}{2} g \tilde{h}_i^{n+1} + \frac{1}{2} (\phi_0 + \tilde{\Phi}_i^{n+1}) (\tilde{h}_i^{n+1})^2. \quad (5.23)$$

Second, the topography term is treated by the hydrostatic reconstruction scheme which has been introduced in Audusse [3] and Bouchut [7]. Actually, this scheme is designed to solve shallow water equations where the pressure is a hydrostatic pressure. However in Richard-Gavrilyuk equations, the pressure term is also using hydrostatic pressure and together with the shear term $(\phi_0 + \Phi)h^3$ become the total pressure. Therefore, the hydrostatic reconstruction scheme can be used to treat the topography term. The detail about this scheme can be seen in [3, 7].

Third, the source term is treated by approximating the system of differential equations

$$d_t h_i = 0, \quad (5.24)$$

$$d_t (h_i u_i) = -C_f u_i |u_i|, \quad (5.25)$$

$$d_t (h_i (u_i^2/2 + e_i)) = - \left(C_f + \frac{\Phi_i}{\phi_0 + \Phi_i} C_r \right) (u_i)^3, \quad (5.26)$$

CHAPTER 5

on $[0, \Delta t]$, with $h_i(0) = \tilde{h}_i^{n+1}$, $u_i(0) = \tilde{u}_i^{n+1}$ and $\Phi_i(0) = \tilde{\Phi}_i^{n+1}$. In order to discretize the friction terms in equations (5.25) and (5.26), we will simplify those equations into primitive variables form. By using the equation (5.24), the equation (5.25) becomes

$$\begin{aligned} h_i d_t(u_i) + u_i d_t(h_i) &= -C_f u_i |u_i|, \\ h_i d_t(u_i) &= -C_f u_i |u_i|, \\ d_t(u_i) &= -\frac{C_f}{h_i} u_i |u_i|. \end{aligned} \quad (5.27)$$

Next, from the equation (5.26) we have

$$d_t \left(\frac{1}{2} h_i u_i^2 + \frac{1}{2} g h_i^2 + \frac{1}{2} (\phi_0 + \Phi_i) h_i^3 \right) = - \left(C_f + \frac{\Phi_i}{\phi_0 + \Phi_i} C_r \right) (u_i)^3,$$

since $d_t h_i = 0$ and ϕ_0 is a constant, thus we have

$$\begin{aligned} \frac{1}{2} u_i d_t(h_i u_i) + \frac{1}{2} h_i u_i d_t(u_i) + \frac{1}{2} d_t(\Phi_i h_i^3) &= - \left(C_f + \frac{\Phi_i}{\phi_0 + \Phi_i} C_r \right) (u_i)^3, \\ \frac{1}{2} u_i (-C_f u_i |u_i|) + \frac{1}{2} h_i u_i \left(-\frac{C_f}{h_i} u_i |u_i| \right) + \frac{1}{2} h_i^3 d_t(\Phi_i) &= - \left(C_f + \frac{\Phi_i}{\phi_0 + \Phi_i} C_r \right) (u_i)^3, \\ -\frac{1}{2} C_f (u_i)^3 - \frac{1}{2} C_f (u_i)^3 + \frac{1}{2} h_i^3 d_t(\Phi_i) &= - \left(C_f + \frac{\Phi_i}{\phi_0 + \Phi_i} C_r \right) (u_i)^3, \\ d_t(\Phi_i) &= - \left(\frac{2C_r \Phi_i}{\phi_0 + \Phi_i} \right) \left(\frac{u_i}{h_i} \right)^3. \end{aligned} \quad (5.28)$$

Therefore, we have the new ordinary differential equations (5.24), (5.27), and (5.28) to discretize the friction terms.

The full discretization of equations (5.24), (5.27), and (5.28) are given as

$$h_i^{n+1} = \tilde{h}_i^{n+1}, \quad (5.29)$$

$$u_i^{n+1} = \tilde{u}_i^{n+1} - \frac{\Delta t C_f}{\tilde{h}_i^{n+1}} \tilde{u}_i^{n+1} |\tilde{u}_i^{n+1}|, \quad (5.30)$$

$$\Phi_i^{n+1} = \tilde{\Phi}_i^{n+1} - \Delta t \left(\frac{2C_r \tilde{\Phi}_i^{n+1}}{\phi_0 + \tilde{\Phi}_i^{n+1}} \right) \left(\frac{\tilde{u}_i^{n+1}}{\tilde{h}_i^{n+1}} \right)^3, \quad (5.31)$$

then we can calculate the new specific internal energy by

$$e(h_i^{n+1}, \Phi_i^{n+1}) = \frac{1}{2} g h_i^{n+1} + \frac{1}{2} (\phi_0 + \Phi_i^{n+1}) (h_i^{n+1})^2. \quad (5.32)$$

Finally, the general algorithm to compute the Richard-Gavrilyuk equations is given in Algorithm 3.

Algorithm 3 The splitting method for Richard-Gavrilyuk equations.

Step 1. Give the initial conditions at $n = 0$.

Step 2. Compute the conservative parts (5.19-5.21) by HLLC solver for \tilde{h}_i^{n+1} , \tilde{u}_i^{n+1} , and $e(\tilde{h}_i^{n+1}, \tilde{\Phi}_i^{n+1})$.

Step 3. Compute the prediction of roller enstrophy $\tilde{\Phi}_i^{n+1}$ by (5.23).

Step 4. Solve (5.29- 5.31) for $h_{i+\frac{1}{2}}^{n+1}$, $u_{i+\frac{1}{2}}^{n+1}$, $\Phi_{i+\frac{1}{2}}^{n+1}$ and immediately we can get $e(h_{i+\frac{1}{2}}^{n+1}, \Phi_{i+\frac{1}{2}}^{n+1})$ by (5.32).

5.3.1 Suliciu/HLLC solver for the conservative part

As we have summarized in Algorithm 3, we use the numerical scheme of splitting method to discretize the Richard-Gavrilyuk equations. The conservative part of our discretization (5.19 - 5.21) has some good mathematical properties as the full gas dynamics which are given in following proposition.

Proposition 6. *The step (5.19 - 5.21) has the following properties:*

(i) *It preserves the positivity of the water height (h).*

(ii) *It satisfies discrete entropy inequality, i.e.,*

$$\tilde{h}_i^{n+1} \rho(\tilde{\Phi}_i^{n+1}) - h_i^n \rho(\Phi_i^n) + \frac{\Delta t}{\Delta x_i} \left(F_{i+\frac{1}{2}}^{\rho(\Phi)} - F_{i-\frac{1}{2}}^{\rho(\Phi)} \right) \leq 0 \quad (5.33)$$

for any ρ convex function.

(iii) *It satisfies the minimum principle on the roller enstrophy, i.e.,*

$$\tilde{\Phi}_i^{n+1} \geq \min_i \Phi_i^n. \quad (5.34)$$

Proof. Here, we use the HLLC solver for approximate the fluxes F in the gas dynamics which is introduced by Bouchut[7]. As we see in Proposition 5 that the quantity $-h\Phi$ is strictly convex satisfied. Moreover, the choice of the HLLC solver (use the relaxation speed into a Riemann solver) for our scheme lead to the positivity of water height, the discrete entropy inequality and the minimum principle on

the roller enstrophy are satisfied. The detail proof of this proposition can be found in [7] specially in Proposition 2.21 Chapter 2. \square

5.4 Numerical simulations

In this section we simulate some numerical simulations such as: dam break, trans-critical flow, roll waves, and runup of solitary wave.

5.4.1 Dam break

The domain is $\Omega = [0, 1]$ and the topography is flat. The initial velocity and the roller enstrophy are zero. The initial water height is $h_{ini}(x) = \mathbb{1}_{x<0.5} + 0.2\mathbb{1}_{x\geq 0.5}$. The results of water height, velocity and enstrophy profile are shown in Figure 5.1, 5.2, and 5.3 respectively with difference value of C_r .

In Figure 5.1 (a), we can see clearly that, with the $C_r = 0$, we have the water height profile such as the full Euler equations. With the $C_r = 100$ which is strong enough, we have the water height profile (Figure 5.1 (c)) is similar to the dam break profile of standard shallow water equations.

The interesting result is shown in Figure 5.1 (b) which has $C_r = 2$. The scheme produces the roller profile in the shock area. This roller waves due to the friction term in the roller enstrophy.

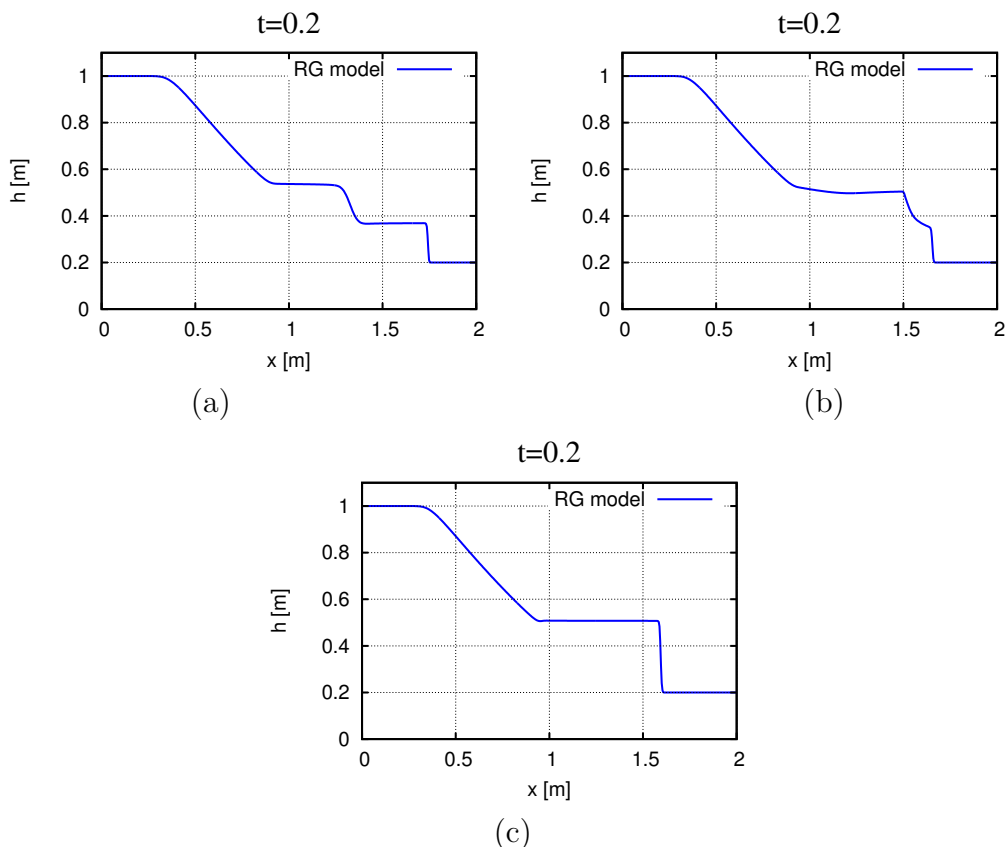


Figure 5.1: The h profile of Dam break at final time $T = 0.2$. (a) $C_r=0$, (b) $C_r=2$, and $C_r=100$

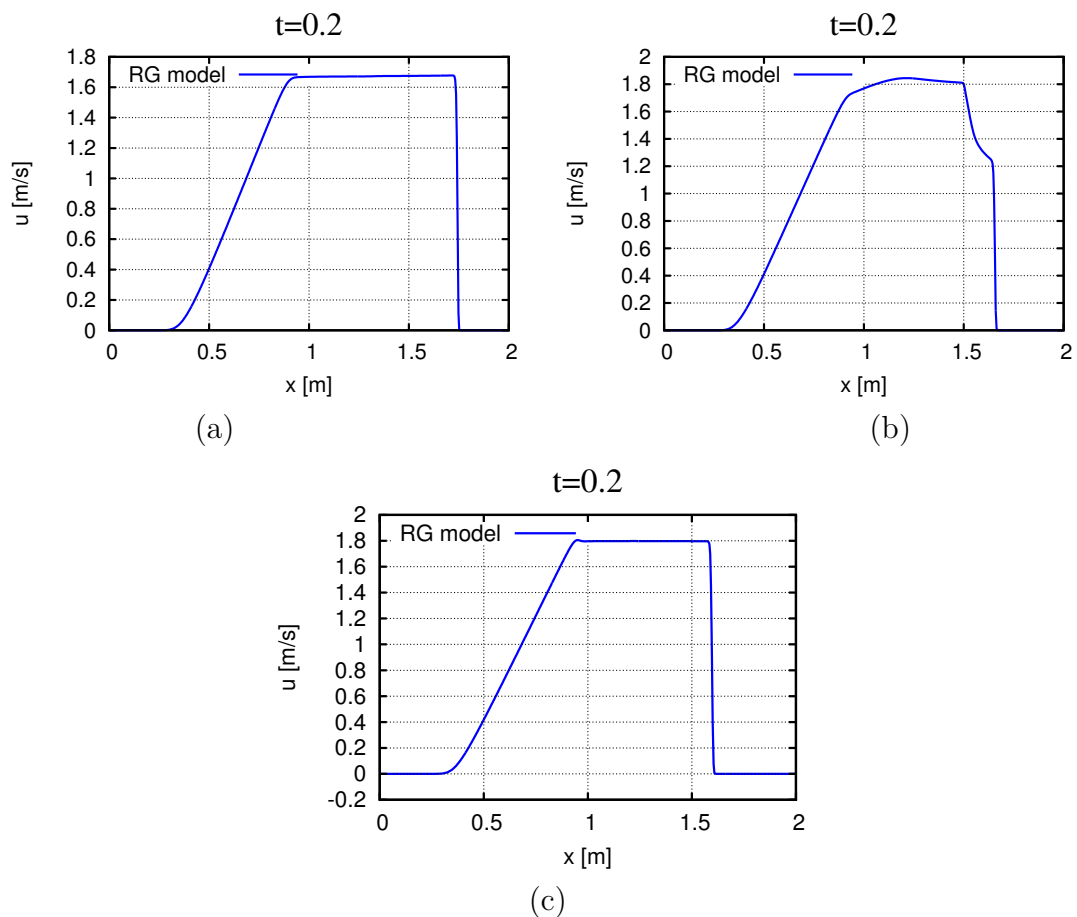


Figure 5.2: The u profile of Dam break at final time $T = 0.2$. (a) $C_r=0$, (b) $C_r=2.$, and $C_r=100$

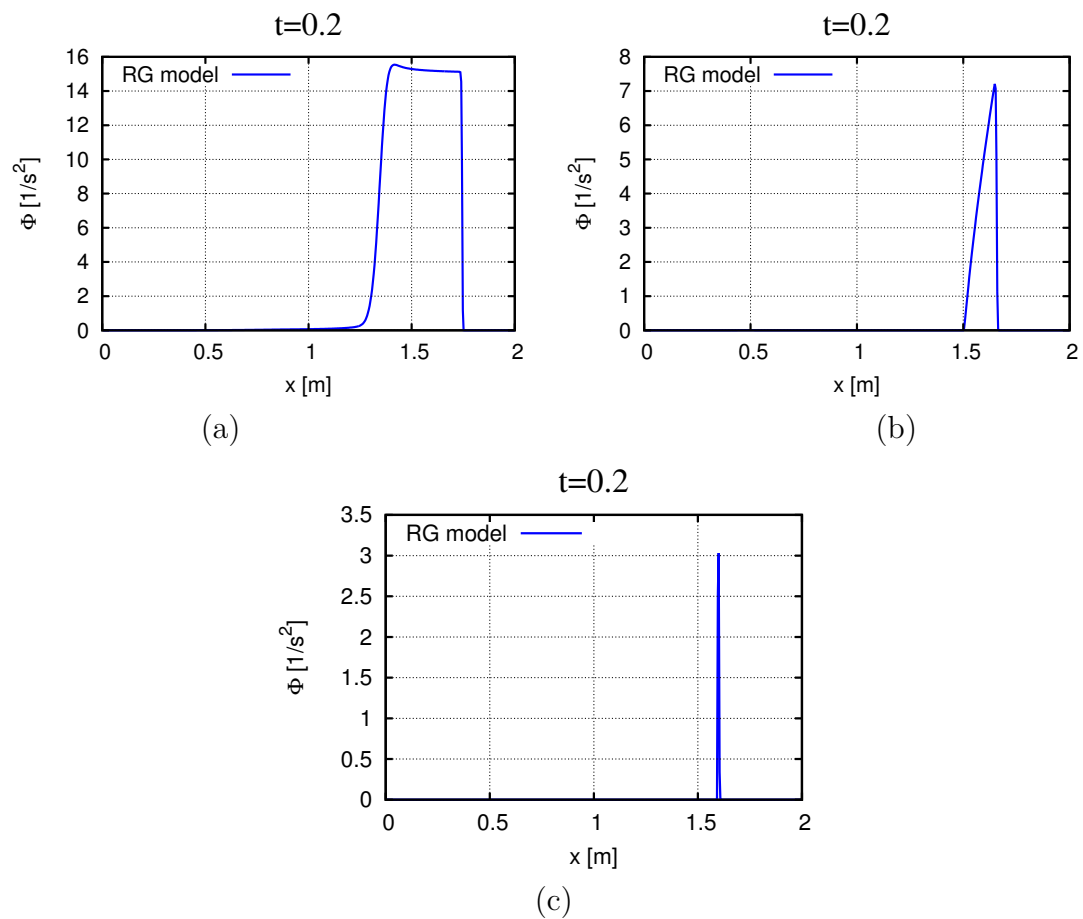


Figure 5.3: The Φ profile of Dam break at final time $T = 0.2$. (a) $C_r=0$, (b) $C_r=2.$, and $C_r=100$

5.4.2 Transcritical flow

Here the simulation of transcritical flow is presented. In this simulation, the domain is $\Omega = [0, 25]$ and the topography is defined as,

$$z(x) = \begin{cases} 0.2 - 0.05(x - 10)^2 & \text{if } 8 < x < 12, \\ 0 & \text{otherwise.} \end{cases}$$

The initial conditions are $h_{\text{ini}}(x) = 0.33 - z(x)$ for the water height and $u_{\text{ini}}(x) = 0.18/0.33$ for the velocity. Here, the friction term is set to be zero ($C_f = 0$). At the upstream end of the domain, the discharge is enforced ($hu(x = 0) = 0.18$), while, at the downstream end, the water height is prescribed ($h(x = 25) = 0.33$). In Figure 5.4, we can see the results of numerical simulation where the water level profile from various C_r are given. This results are obtained at final time $t = 25$. Here the results are presented in various roller drag coefficients $C_r = 0$, $C_r = 2$ and $C_r = 100$. At the final time $t = 2.5$, the profile of water level with $C_r = 0$ is not completely reaches a steady state. We can see that the oscillation still occurs in the downstream area. Meanwhile, with the $C_r = 2$ and $C_r = 100$, the steady state is completely reached at final time $t = 2.5$.

Next, we are interested in the value of roller drag coefficient between $C_r = 0$ and $C_r = 2$ at greater final time $t = 100$. From several numerical experiments, here we found interesting result with $C_r = 0.5$ (see Figure 5.5). In Figure 5.5 we can see that, with $C_r = 0$ and $C_r = 2$ the hydraulic jump occurs at the transition from a rapid flow to steady state in an open channel. Meanwhile, with $C_r = 0.5$ we have a hydraulic jump of low height with free-surface or standing waves. As recorded in [49], those standing waves are called undulations, where they can stretch out over a great length due to the low dissipation of wave. This phenomena is called the undular hydraulic jump.

For the long time simulation ($t \geq 100$), the profiles of water level with $C_r = 0$ and $C_r = 2$ reach completely a steady state condition. However, form our observation, we find that the water height profile with $C_r = 0.5$ keep in unsteady condition (see Figure 5.6). In Figure 5.6, we show the time series of the average of water level in location around $10 \leq x \leq 14$. Here, we can see clearly that, with the $C_r = 0.5$ the undular hydraulic jump keeps produce waves in the long time simulations.

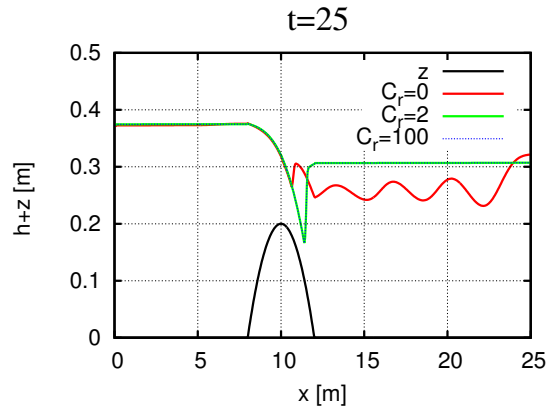


Figure 5.4: The comparison of $h + z$ in various C_r at final time $t = 25$.

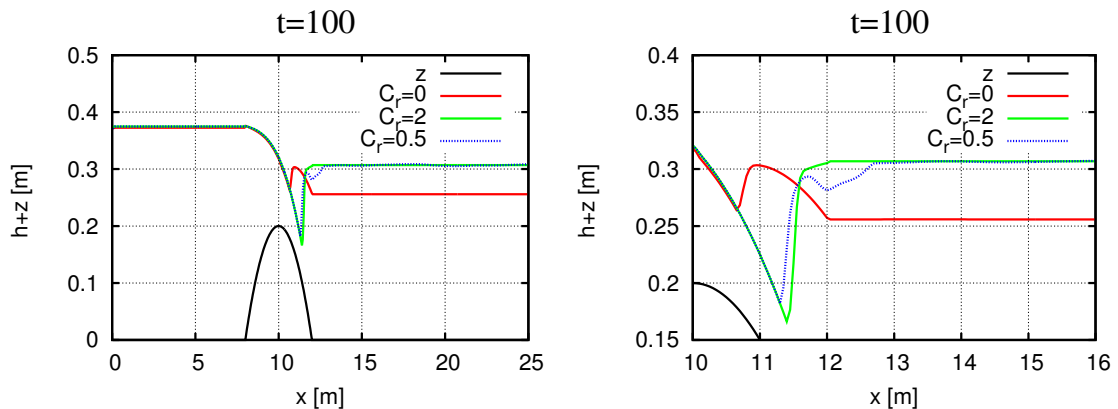


Figure 5.5: (Left) The comparison of $h + z$ in various C_r at final time $t = 25$. (Right) The zoom part around the hydraulic jump

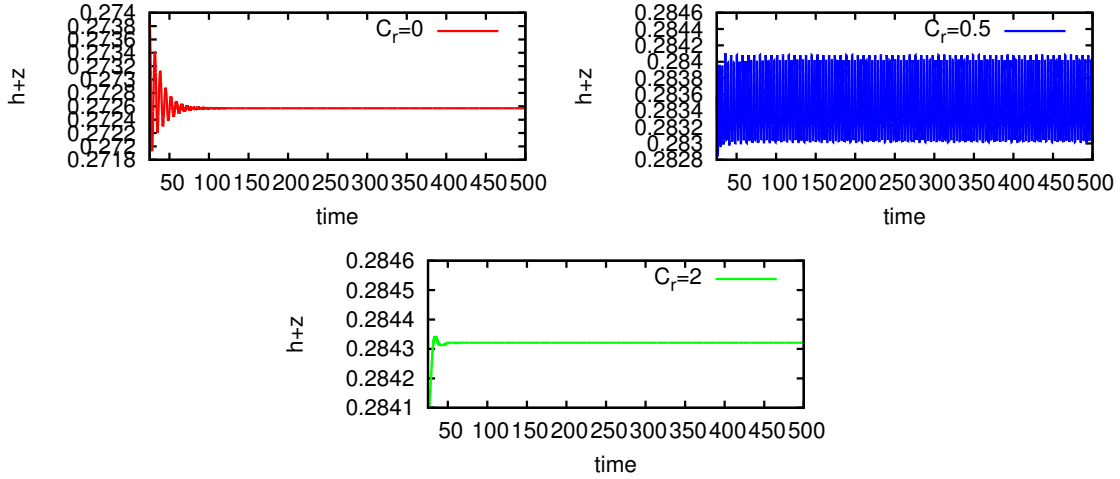


Figure 5.6: The time series of the average of water level in location around $10 \leq x \leq 14$ with various C_r .

5.4.3 Roll waves

The purpose of this section is to present the numerical simulation of roll waves. As described in [17], the instability flow occurs due to the steady flow down an inclined channel. Moreover with the periodic solutions, the roll waves appear by a hydraulic jump which is located at transition between subcritical and supercritical flow (see Figure 5.7).

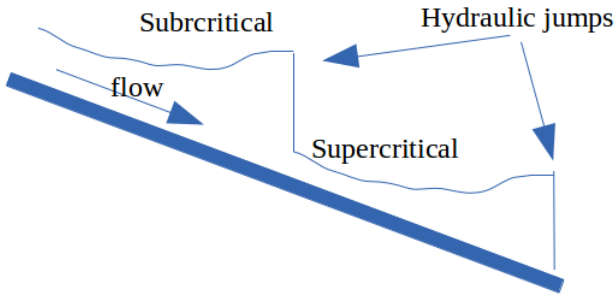


Figure 5.7: Sketch of roll waves down an inclined open channel

In Figures 5.8 and 5.9, the photographs of roll waves in a concrete channel in Lions Bay, B.C. are presented (the photos was taken from [12]). We can observe clearly that, on the inclined channel the periodic nature of waves are shown. Moreover, the waves seem to be long and shallow.



Figure 5.8: Roll waves flow down an inclined channel. Source: <http://www.math.ubc.ca/~njb/Research/rollo.htm>



Figure 5.9: Roll waves flow down an inclined channel by Grünnbach, Merlingen (Suisse) in [12].

CHAPTER 5

In the manuscript of [14], the simulation of roll waves has been done with the shallow water equations using collocated scheme. On the other hand, in this section we want to elaborate the simulation of roll waves using standard shallow water equations and Richard-Gavrilyuk model. The approximation of shallow water equations and Richard-Gavrilyuk model are using staggered scheme and collocated scheme (HLLC solver) respectively. In this simulation, the topography should not be flat i.e the bottom has a constant slope related to the Froude number. The slope of canal is fixed with the relation

$$S = \frac{fu^2}{8gh} = \frac{f}{8} Fr^2, \quad (5.35)$$

where $f = 0.048$ is the Darcy-Weisbach coefficient and Fr the Froude number. The domain is $\Omega = [0 : 2]$, the initial water height and debit are given by

$$h_{\text{ini}}(x) = h_0(\epsilon \sin(\kappa x) + 1), \quad (5.36)$$

$$q_{\text{ini}}(x) = 0.001, \quad (5.37)$$

where $\epsilon = 0.005$, $\kappa = 5\pi$ and h_0 is a constant value defined by

$$h_0 = \left(\frac{1}{g} \frac{q_{\text{ini}}^2}{Fr^2} \right)^{1/3}. \quad (5.38)$$

As explained in [14] and [36], the perturbations to the steady solution will be obtain if the Froude number $Fr > 2$. Contrary, with the Froude number $Fr \leq 2$ the steady solution will be achieved. Therefore, first we present the numerical simulation of roll-waves with several Froude numbers. The evolution of roll-waves by standard shallow water equations using staggered scheme at several times with Froude numbers $Fr = 1.5$, $Fr = 2$ and $Fr = 2.5$ are shown in Figures 5.10, 5.11 and 5.12 respectively. Moreover, the results in Figure 5.12 are in a good agreement with the results by Y-T. Que and K. Xu (2006) in [36] (page 1016).

CHAPTER 5

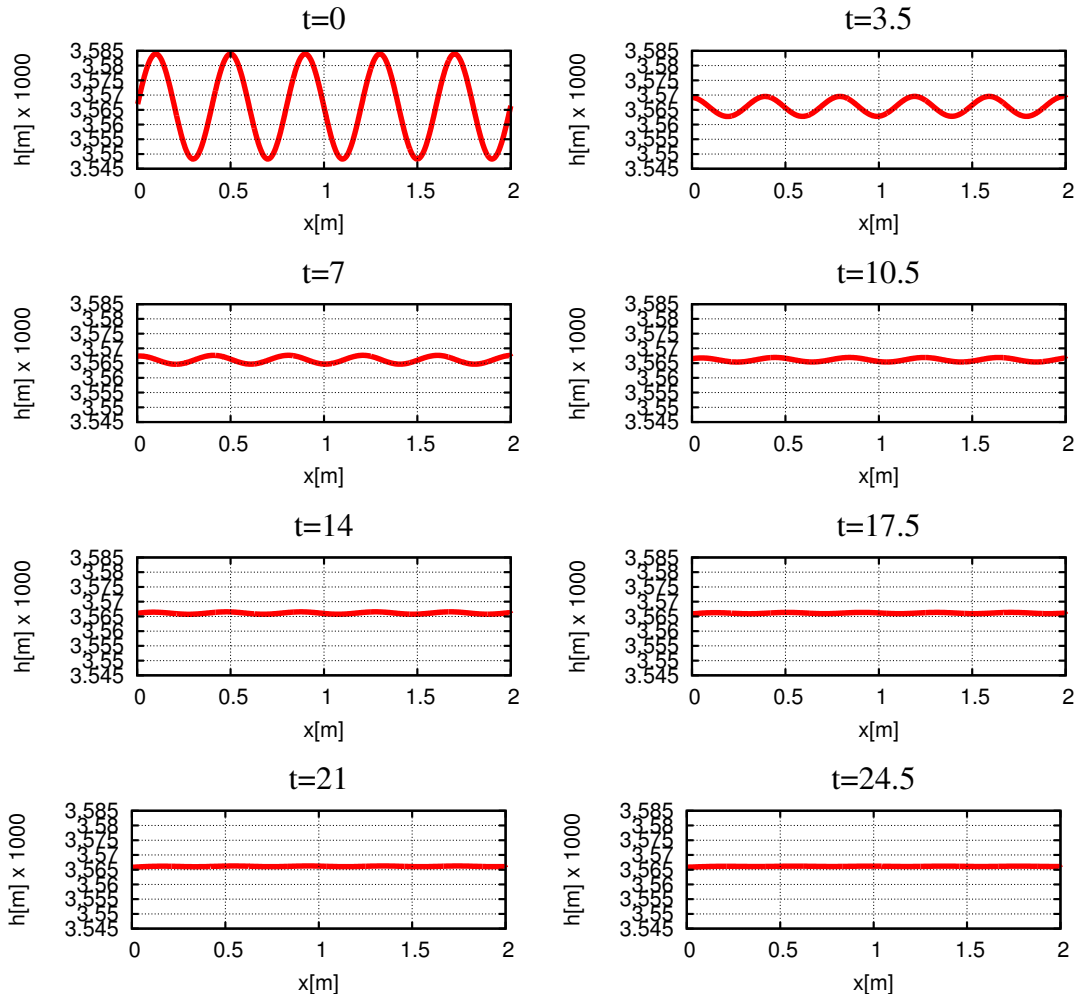


Figure 5.10: The evolution of roll-waves by staggered scheme with several times. The parameters values are $\epsilon = 0.5\%$, $k = 5\pi$, $C_f = 0.048/8$, $q_0 = 0.001m^2s^{-1}$, and $F_r = 1.5$.

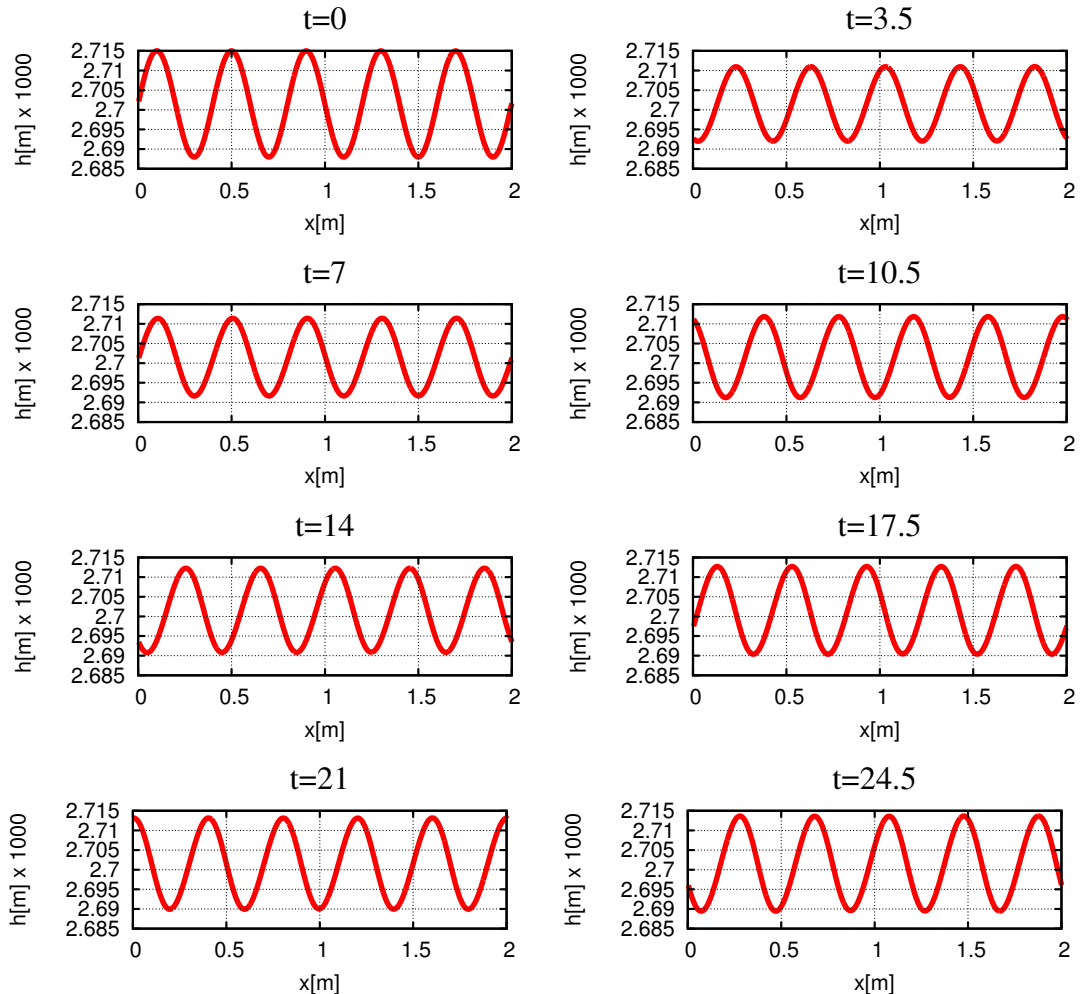


Figure 5.11: The evolution of roll-waves by staggered scheme with several times. The parameters values are $\epsilon = 0.5\%$, $k = 5\pi$, $C_f = 0.048/8$, $q_0 = 0.001m^2s^{-1}$, and $F_r = 2$.

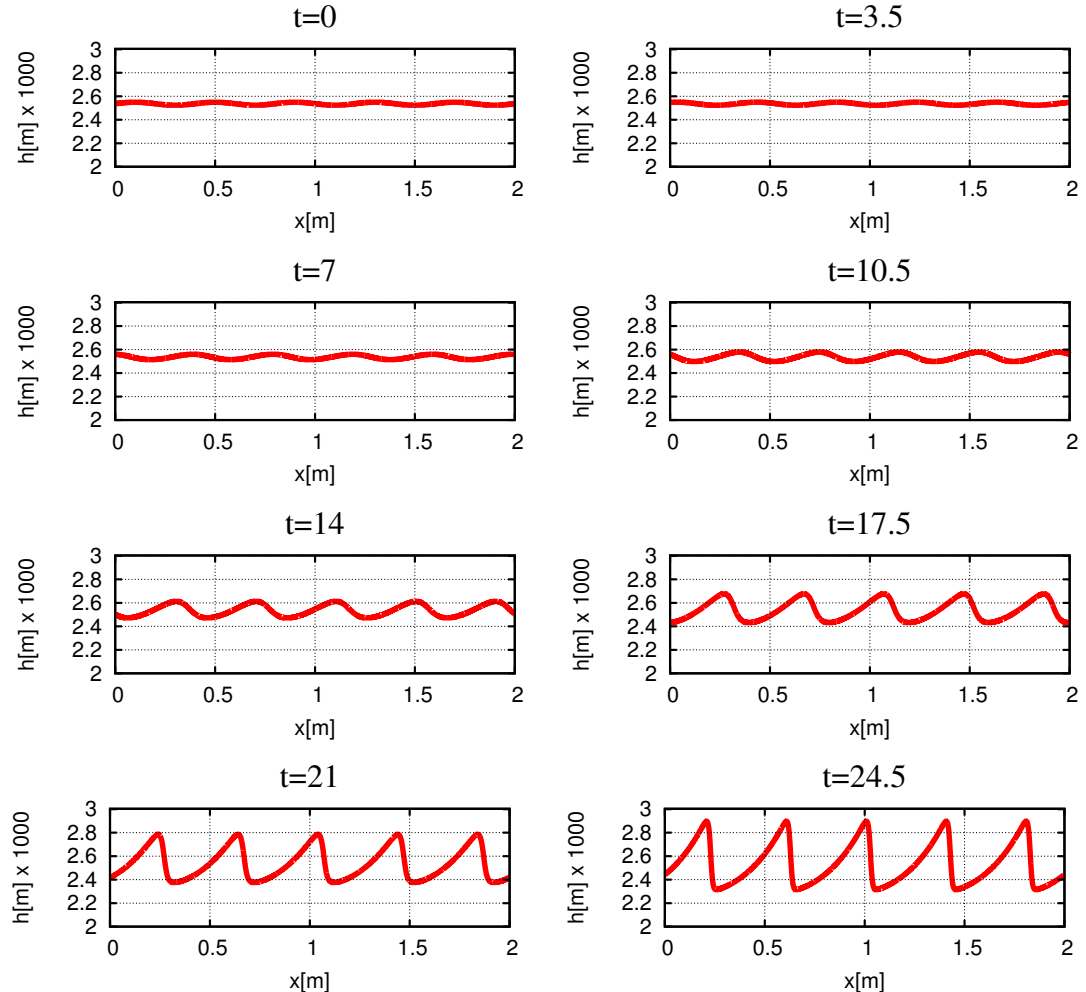


Figure 5.12: The evolution of roll-waves by staggered scheme with several times. The parameters values are $\epsilon = 0.5\%$, $k = 5\pi$, $C_f = 0.048/8$, $q_0 = 0.001m^2s^{-1}$, and $F_r = 2.5$.

CHAPTER 5

The evolution of roll waves by Richard-Gavrilyuk model using collocated scheme (HLLC solver) at several times with Froude numbers $F_r = 1.5$, $F_r = 2$ and $F_r = 2.5$ are shown in Figures 5.13, 5.14 and 5.15 respectively. We can see clearly that, with the Froude number $F_r = 1.5$ in Figure 5.13 the water surface reaches the steady state at long time simulation. Meanwhile, with $F_r \geq 2$ the unstable waves occurs in the long time simulation as shown in Figure 5.14 and 5.15. Therefore from our results, the theory of stability ($F_r < 2$) and instability ($F_r \geq 2$) conditions for our scheme are satisfied.

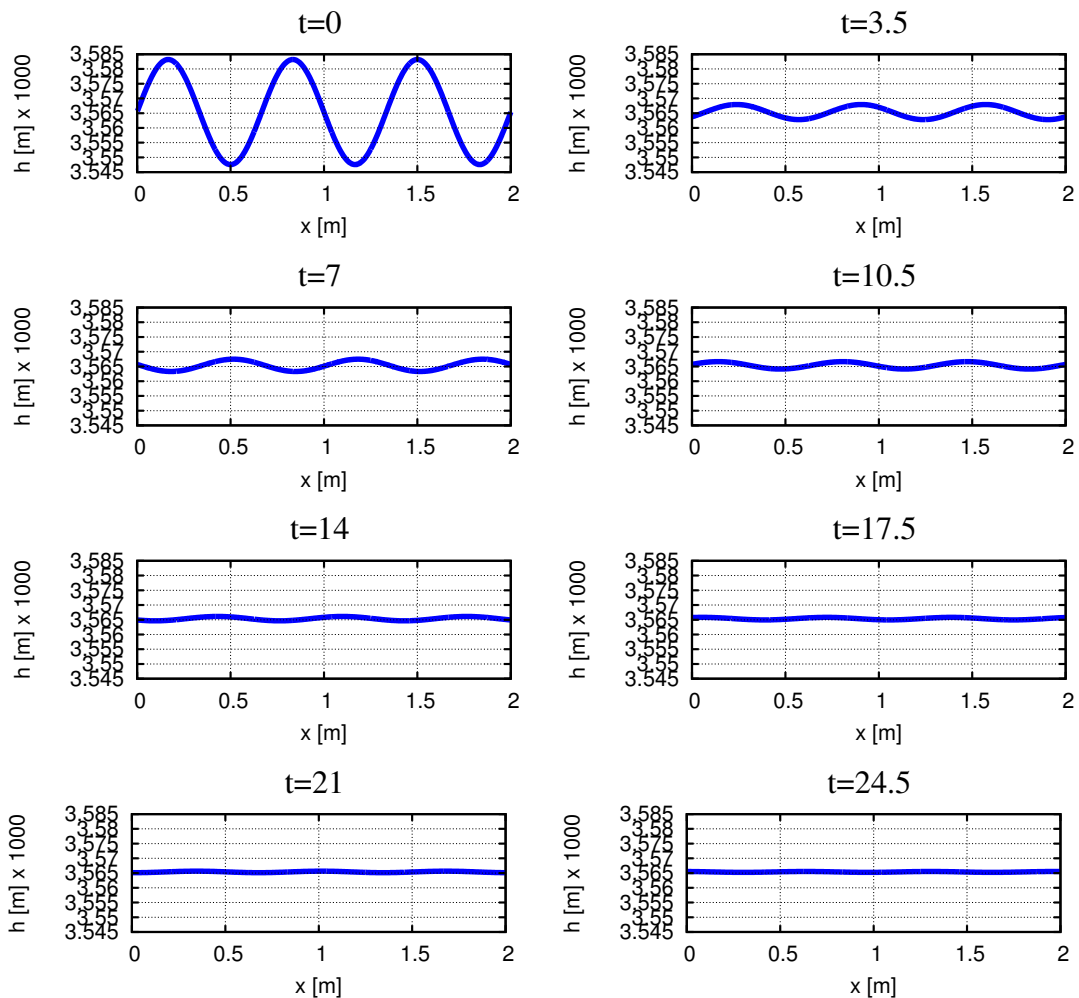


Figure 5.13: The evolution of roll-waves by Richard-Gavrilyuk model using HLLC solver with several times. The parameters values are $\epsilon = 0.5\%$, $k = 5\pi$, $C_f = 0.048/8$, $q_0 = 0.001m^2s^{-1}$, $\phi_0 = 0.02$, $C_r = 0.5C_f$ and $F_r = 1.5$.

In the previous simulations, the roller drag coefficient $C_r = 0.5C_f$ are given

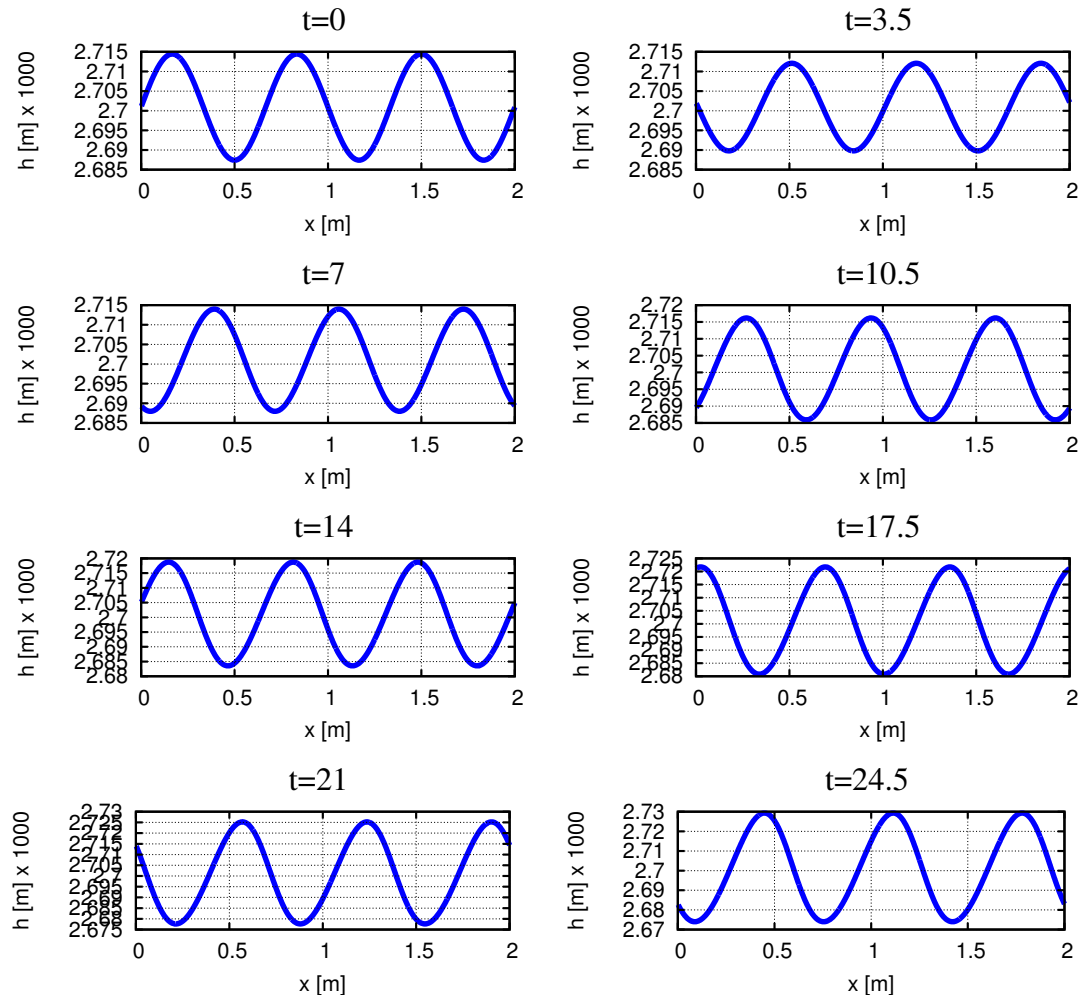


Figure 5.14: The evolution of roll-waves by Richard-Gavrilyuk model using HLLC solver with several times. The parameters values are $\epsilon = 0.5\%$, $k = 5\pi$, $C_f = 0.048/8$, $q_0 = 0.001 m^2 s^{-1}$, $\phi_0 = 0.02$, $C_r = 0.5C_f$ and $F_r = 2$.

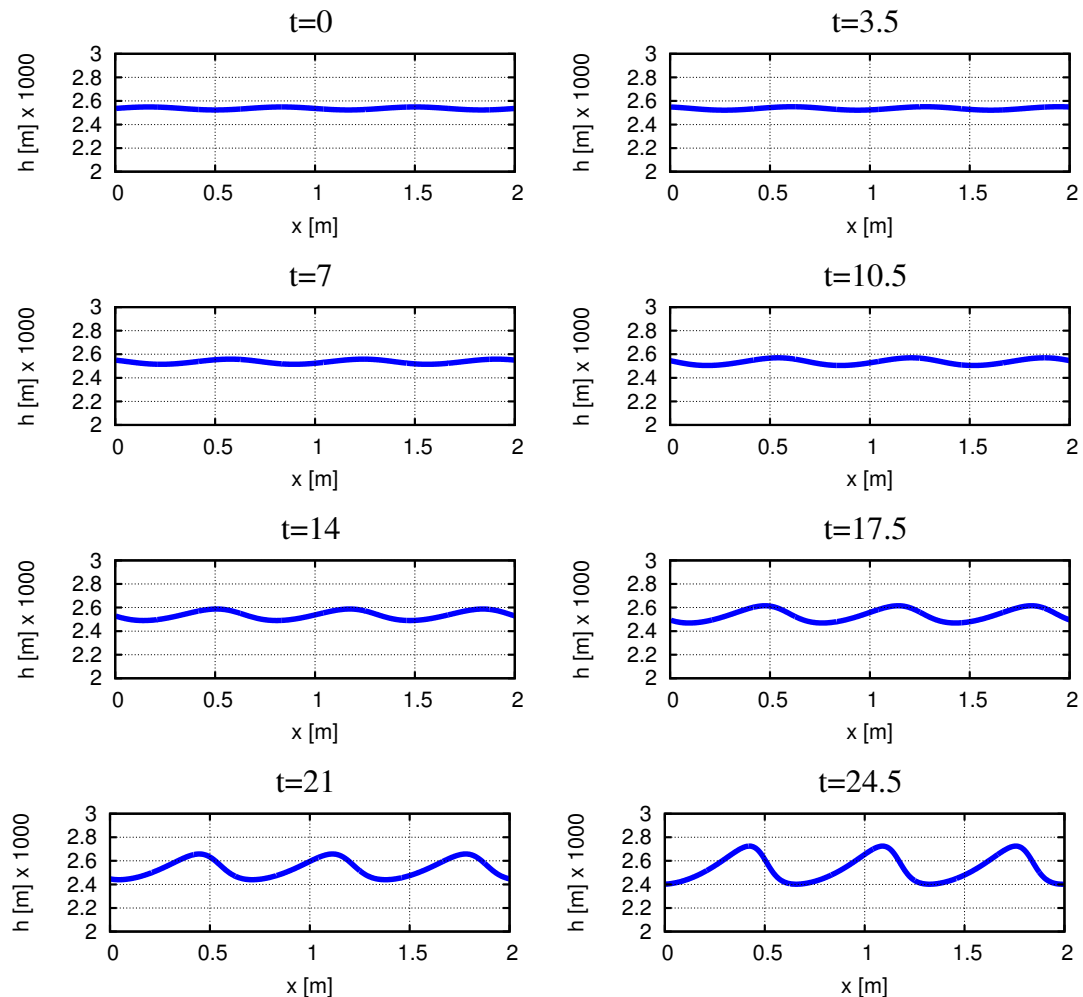


Figure 5.15: The evolution of roll-waves by Richard-Gavrilyuk model using HLLC solver with several times. The parameters values are $\epsilon = 0.5\%$, $k = 5\pi$, $C_f = 0.048/8$, $q_0 = 0.001 m^2 s^{-1}$, $\phi_0 = 0.02$, $C_r = 0.5C_f$ and $F_r = 2.5$.

CHAPTER 5

arbitrary. Here, we present the numerical experiment of roll waves by several roller drag coefficients. The results of roll waves with $C_r = 0.1C_f$, $C_r = 0.5C_f$ and $C_r = 100C_f$ with $F_r = 6$ are shown in Figure 5.16. In Figure 5.16, the comparison of water height h , velocity u , and roller enstrophy Φ are given at long time simulation $t = 200$. Here we can confirm that the period distance of water height depends on the value of C_r .

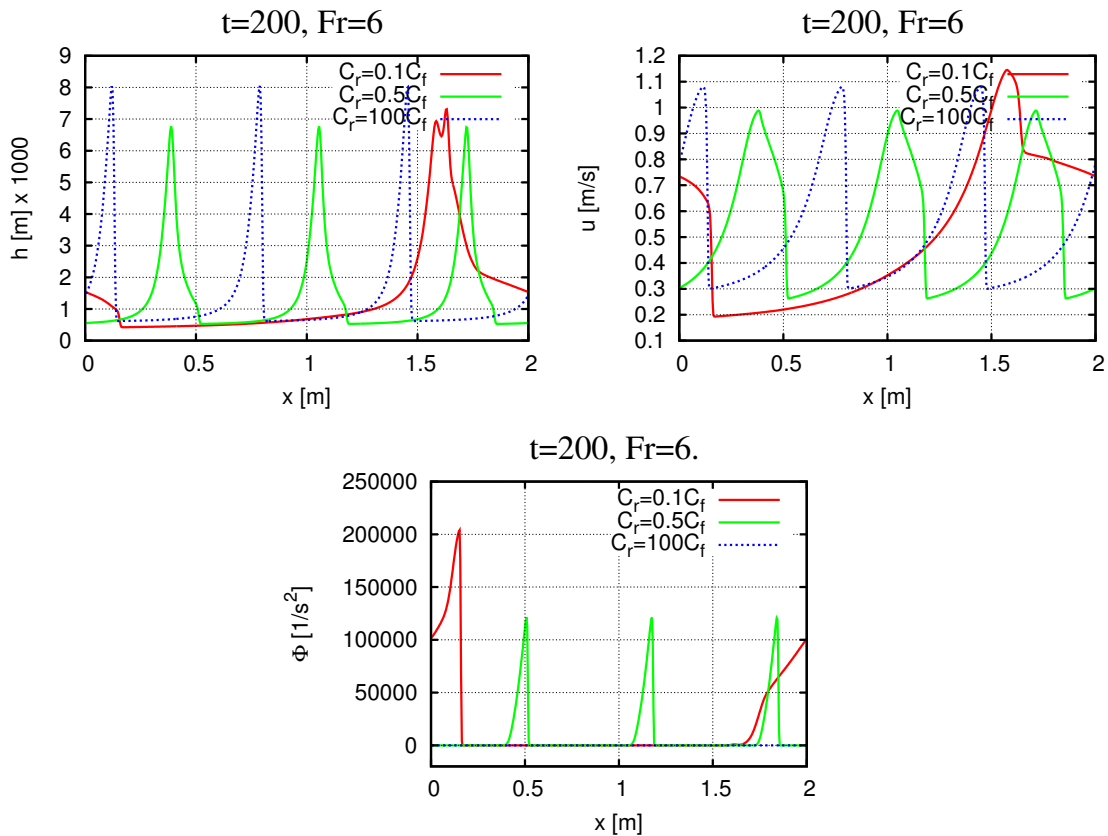


Figure 5.16: The comparison of h , u and Φ in various C_f at final time $t = 200$.

5.4.4 Runup of solitary wave

The aim of this section is to simulate the solitary wave using the standard shallow water equations and Richard-Gavrilyuk model. Here, the discretization of shallow water equations uses the explicit staggered scheme as in Chapter 1. Meanwhile, the discretization of Richard-Gavrilyuk model uses the HLLC method in Section 5.3.

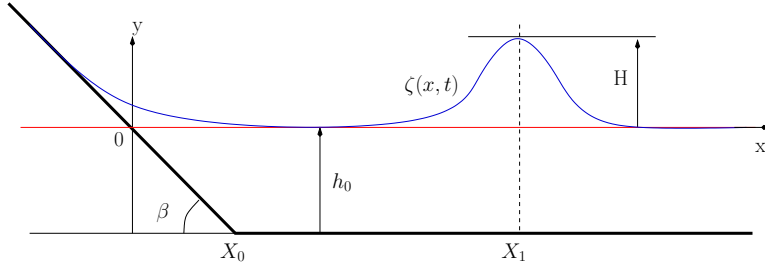


Figure 5.17: The sketch of runup of solitary wave.

The experiment setup follow the model which is introduced by Synolakis [43]. The sketch of experiment can be seen in Figure 5.17. In Figure 5.17, the elevation of solitary wave is described by $\zeta(x, t)$ with the amplitude H and initial location wave height X_1 . The sloping topography with an angle β to the x -direction is located in the left side of X_0 and a constant depth h_0 at the right side.

In order to simulate the runup of solitary wave, here the domain is given as $\Omega = [-10, 20]$. The initial conditions are given as,

$$\begin{aligned}\zeta_{\text{ini}}(x) &= (h + z)_{\text{ini}}(x) = \frac{H}{h_0} \operatorname{sech}^2 \left(\sqrt{(3H/4h_0)}(x - X_1) \right), \\ u_{\text{ini}}(x) &= -\frac{\left(\sqrt{g(H + h_0)} \right) \zeta_{\text{ini}}(x)}{1 + \zeta_{\text{ini}}(x)}, \\ z_{\text{ini}}(x) &= -\frac{x}{X_0} \mathbb{1}_{x \leq X_0} - \mathbb{1}_{x > X_0}, \\ X_1 &= X_0 + \frac{1}{\sqrt{(3H/4h_0)}} \operatorname{arccosh} \sqrt{20}.\end{aligned}$$

where the initial sloping point is $X_0 = 19.85$. Here, the other parameters are $H = 0.3$, $h_0 = 1$ and dimensionless time $t_0 = \sqrt{g/h_0}$. The results of surface profile of shallow water equations using staggered scheme are shown in Figure 5.18. They show the comparisons of numerical simulation and experimental data in various final times.

We can observe clearly that, the shallow water equations using staggered scheme produces nicely comparable results with experimental data.

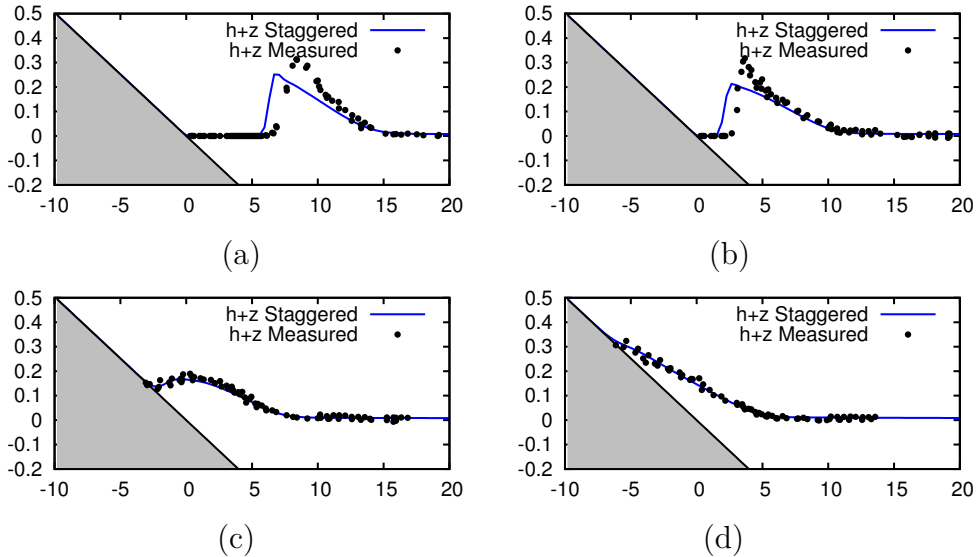


Figure 5.18: The surface profile of standard shallow water equations using staggered scheme at $t = 15t_0$ (a), $t = 20t_0$ (b), $t = 25t_0$ (c), and $t = 30t_0$ (d).

The Figures 5.19 and 5.20 are shown the comparison of Richard-Gavrilyuk model and experimental data with the coefficients $C_f = 0, C_r = 0$ and $C_f = 0.01, C_r = 0.006$ respectively. Here, we can see clearly that, the diffusive shock is obtained at time from $15t_0$ to $25t_0$ from both figures. However, at final time $t = 30t_0$, the results is slightly better. The surface profile of numerical approximation and experimental data is nicely comparable.

Further, we are interested to compare the shallow water equations, Richard-Gavrilyuk model and experimental data in one frame. Their results can be found in Figure 5.21. In Figure 5.21, we used the Richard-Gavrilyuk model with $C_f = 0.01$ and $C_r = 0.006$. We can observe that in Figure 5.21, the shallow water equations is better than the Richard-Gavrilyuk model. In Figure 5.21 (a) and (b) the shock waves of shallow water equations are better than Richard-Gavrilyuk model to approach experimental data. Moreover, in Figure 5.21 (c) and (d) where the solitary wave approaches the coastal area, the shallow water equations is more nicely comparable than Richard-Gavrilyuk model to simulate the dry wet simulation.

Another simulation is used $H/h_0 = 1.85 \times 10^{-2}$ from [43]. The results are given in Figures 5.22 and 5.23. They show that, both models are nicely comparable with the

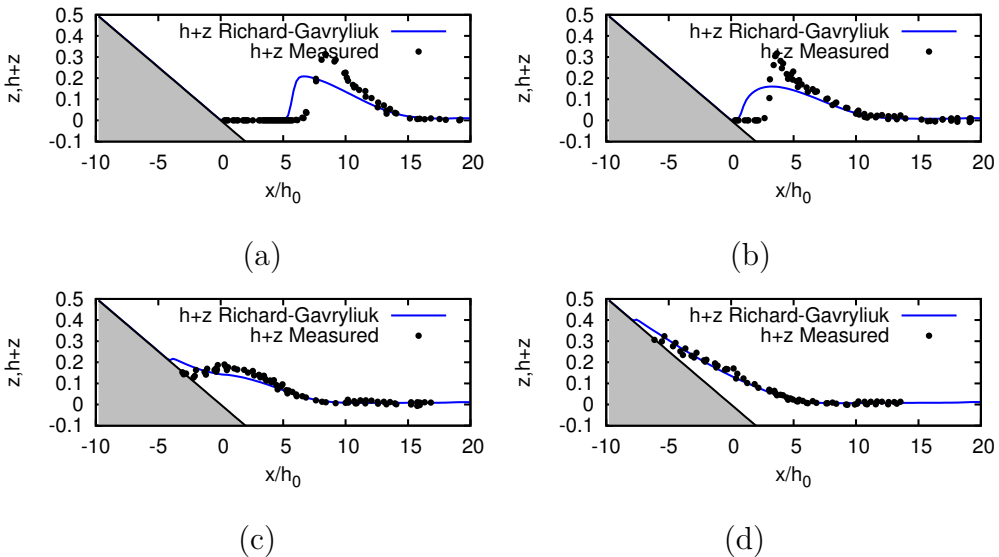


Figure 5.19: The surface profile of Richard-Gavrilyuk model at $t = 15t_0$ (a), $t = 20t_0$ (b), $t = 25t_0$ (c), and $t = 30t_0$ (d). The coefficients C_r and C_f are set to be zero for both.

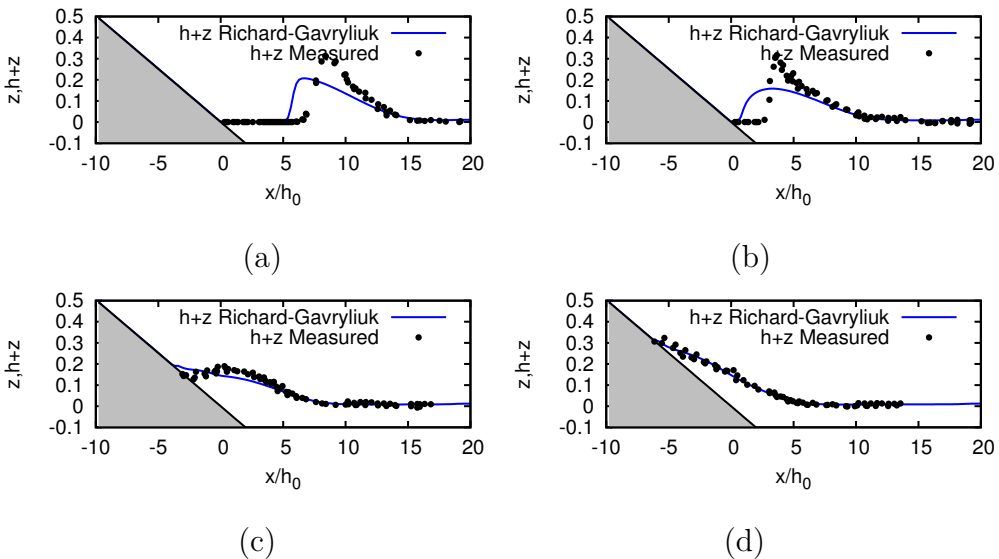


Figure 5.20: The surface profile of Richard-Gavrilyuk model at $t = 15t_0$ (a), $t = 20t_0$ (b), $t = 25t_0$ (c), and $t = 30t_0$ (d). The coefficients C_r and C_f are set to be 0.01 and 0.006 respectively.

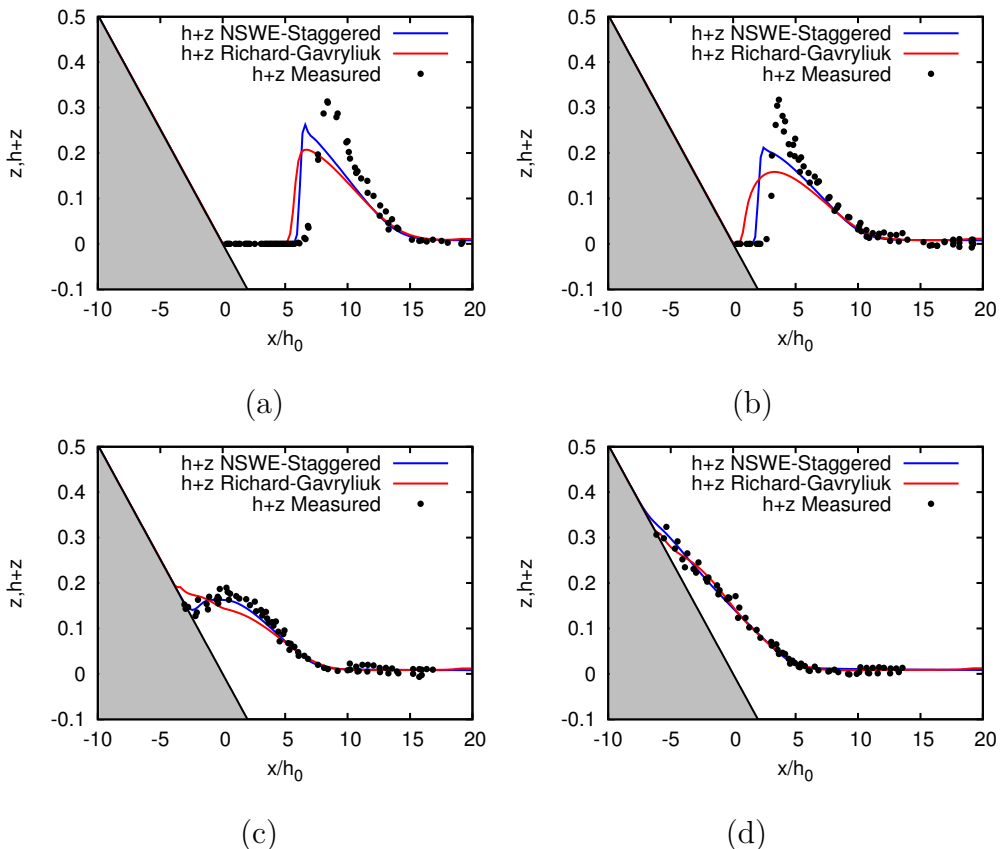


Figure 5.21: The comparison of surface profile between standard shallow water equations using staggered grid scheme and Richard-Gavriluk model using collocated HLLC flux at various final times $t = 15t_0$ (a), $t = 20t_0$ (b), $t = 25t_0$ (c), and $t = 30t_0$ (d). The coefficients C_r and C_f in Richard-Gavriluk model are set to be 0.01 and 0.006 respectively.

CHAPTER 5

experimental data. Moreover, in zoom part of final time step $t = 70t_0$ in Figure 5.24, we can see clearly that shallow water equations nicely satisfied dry transition and reached the lowest point from experimental data. Meanwhile, the Richard-Gavrilyuk model remains wet on the inclined bed and just approximates the upper points of experimental data.

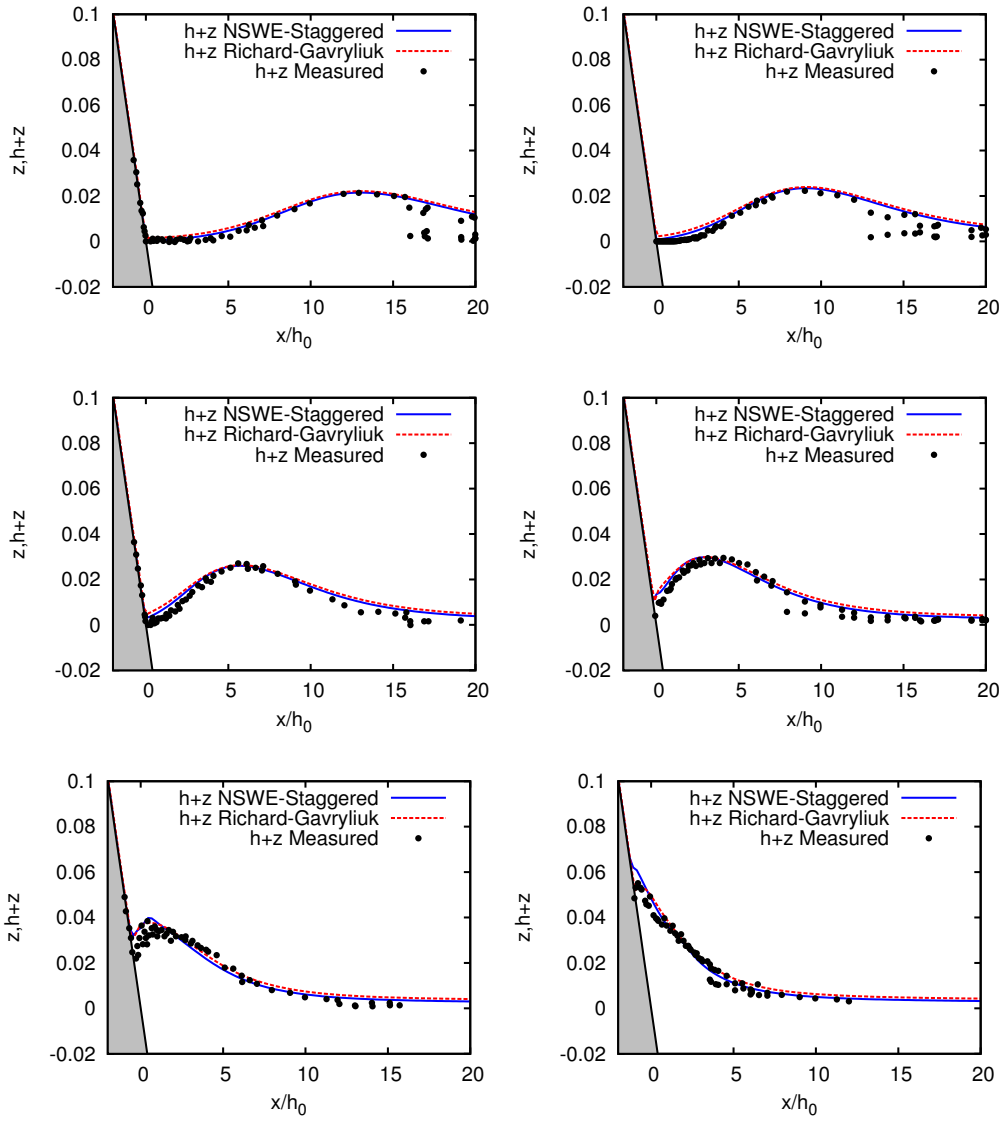


Figure 5.22: The comparison of surface profile between standard shallow water equations using staggered grid scheme and Richard-Gavriluk model using collocated HLLC flux at various final time steps. The time steps are provided from $t = 25t_0$ to $t = 50t_0$ with 5 increments and the initial wave $H/h_0 = 1.85 \times 10^{-2}$. The coefficients C_r and C_f in Richard-Gavriluk model are set to be 0.01 and 0.006 respectively.

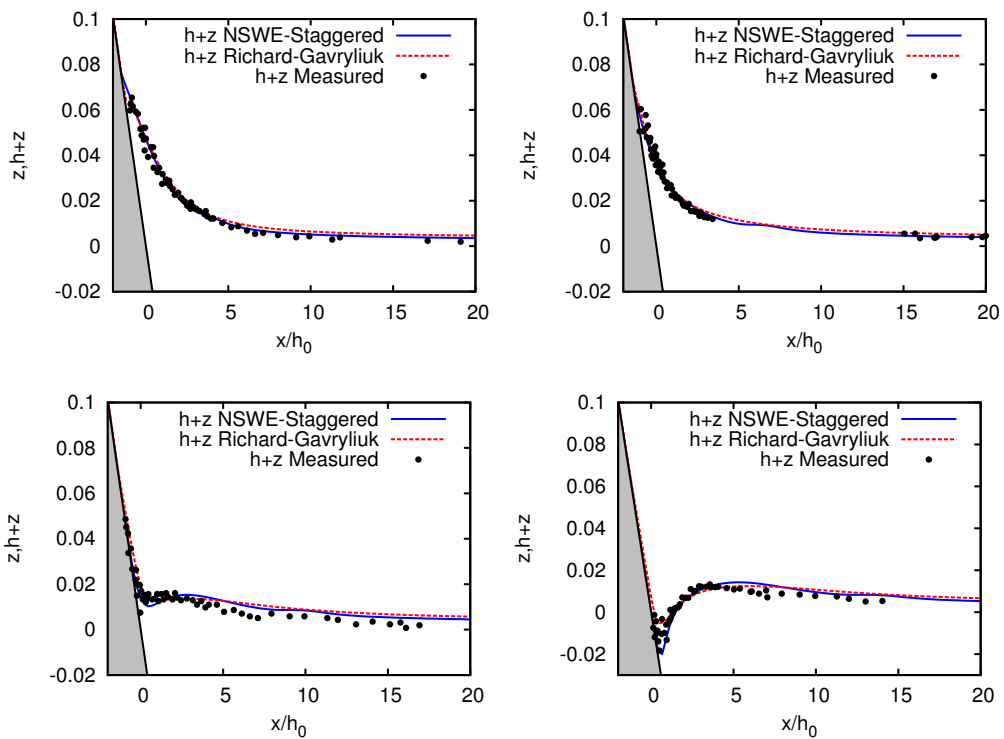


Figure 5.23: The comparison of surface profile between standard shallow water equations using staggered grid scheme and Richard-Gavriluk model using collocated HLLC flux at various final time steps. The time steps are provided from $t = 55t_0$ to $t = 70t_0$ with 5 increments and the initial wave $H/h_0 = 1.85 \times 10^{-2}$. The coefficients C_r and C_f in Richard-Gavriluk model are set to be 0.01 and 0.006 respectively.

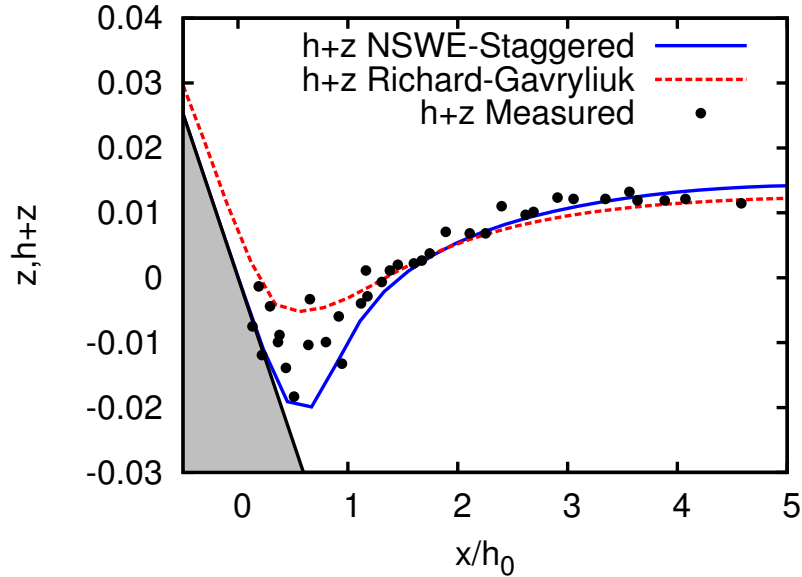


Figure 5.24: The comparison of surface profile between standard shallow water equations using staggered grid scheme and Richard-Gavriluk model using collocated HLLC flux at various final time step $t = 70t_0$ in the zoom part.

5.5 Conclusion

The numerical scheme for Richard-Gavriluk model has been constructed. This scheme is based on splitting method. First, the conservative part of Richard-Gavriluk equations is solved by Suliciu finite volume scheme /HLLC solver. Then, the source terms are treated by approximating the system of differential equations. Some numerical simulations have been presented to show the robustness of the scheme. Some numerical simulation such as dam-break and transcritical flow using Richard-Gavriluk model have been done. Moreover, the numerical simulation in roll and runup solitary wave using Richard-Gavriluk model together with the standard shallow water equations have been described. In the simulation of runup solitary wave, the results are in a good agreement with experimental data from both models.

CHAPTER 5

Summary and perspective

The staggered scheme is an alternative to the collocated schemes for solving the shallow water equations. The staggered scheme presents the same mathematical guarantees as the collocated schemes. In particular, the staggered scheme is consistent with the entropy inequality. The componentwise computation of numerical fluxes is simpler than the approximate Riemann solvers and the well-balanced discretization of the topography source term is straightforward. The numerical tests demonstrate that the staggered scheme is as accurate and robust as the collocated schemes. Some applications have been done into various problems such as in geostrophic flows and viscous flow. Another related models such as shallow water - Exner equations and shear shallow water are described. The staggered grid scheme into one-dimensional case of shallow water - Exner equations is constructed and is shown to be a robust scheme. Moreover, the numerical scheme for approximating the Richard-Gavrilyuk model in shear shallow water flow is also constructed. Here, we construct the collocated scheme with HLLC solver to discretize the Richard-Gavrilyuk model. Various simulations in shear shallow water flow have been done together with standard shallow water equations and Richard-Gavrilyuk model.

From previous works in this thesis, we have several perspectives for future work. Our first perspective here is to develop the numerical scheme for modelling the tsunami wave mitigation by mangroves in shallow water flow. A way of modelling the mangrove resistance is to add a bottom friction term (similar to those used in the simulation of overland flows [14]) to the shallow water equations.

Second perspective here is to develop the numerical scheme in two-dimensional case for the Exner – shallow water equations. Moreover, the comparison of the result with the experimental data will be needed.

Last but not least, our perspective is to analyse and to build the explicit staggered numerical scheme for Richard-Gavriliyuk equations.

SUMMARY AND PERSPECTIVE

PART III

Appendices

Appendix A

A.1 Analytical solution

In this section, we will discuss two analytical solutions for shallow water equations. Here we present the analytical solution for a dam break problem and oscillation in Paraboloid for dry-wet problem. Another analytical solutions for the standard test which are given in Chapter 1 can be found in the papers or thesis of Delestre [14, 15].

A.1.1 Dam break

First, we will explain one of the standard tests for shallow water equations that is a dam break problem. This problem is important test because it has an analytical solution. In this test, two cases are exist such as wet and dry dam break problem. A wet dam break test is also important to see the applicability of our scheme to handle shock. Meanwhile, a dry dam break is a numerical test to confirm the robustness of our scheme to handle vacuum. The analytical solution of this problem also can be found in [14, 15].

Let $x_0 \in \mathbb{R}$ is the position of the discontinuity and we define the initial condition of water height such as in (Figure A.1 (a))

$$h(0, x) = \begin{cases} h_g & x \leq x_0 \\ h_d & x > x_0 \end{cases} \quad (\text{A.1})$$

with

$$0 \leq h_d \leq h_g, \quad (\text{A.2})$$

thus h_g is represent the highest of water level in dam break.

APPENDIX A

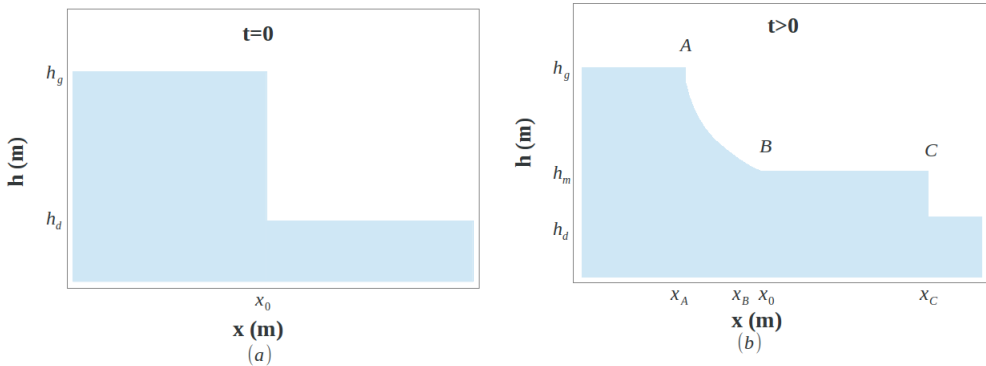


Figure A.1: Dam break on wet bottom

The initial condition for the velocity is

$$u(0, x) = 0 \quad \forall x \in \mathbb{R} \quad (\text{A.3})$$

In order to make a simple description for this analytical solution, we define a dam at $x_0 = 0$. The interesting one for us is to see the result when $t > 0$ after dam break. From Figure A.1 (b), we can see that there is a parabolic shape (between point A and B) between h_g and h_m , and there is a shock (in point C) between h_m and h_d .

Let the celerities $c_g = \sqrt{gh_g}$, $c_m = \sqrt{gh_m}$, $c_d = \sqrt{gh_d}$ and u_m are the water velocities in zone m (between point B and C). Due to Riemann invariant and theory characteristics, we can obtain celerity and velocity for $x \in [x_A, x_B]$

$$\begin{cases} c = \sqrt{gh} = \frac{2}{3}(c_g - \frac{x}{2t}) \\ u = \frac{2}{3}(\frac{x}{t} + c_g) \end{cases} \quad (\text{A.4})$$

where

$$h = \frac{4}{9g}(c_g - \frac{x}{2t})^2. \quad (\text{A.5})$$

As we can see that, point B is located on the zone m and there is relaxation by Riemann invariant, so we obtain

$$u_m = 2(c_g - c_m). \quad (\text{A.6})$$

At last, due to Riemann invariant and jump relation (Rankine–Hugoniot) on the

APPENDIX A

zone m until zone d , we obtain the shock velocity,

$$v_c = \frac{h_m u_m}{h_m - h_d}. \quad (\text{A.7})$$

Then the last unknown c_m is found by an equation sixth degree (resolved by iterations):

$$c_m^6 - 9c_d^2 c_m^4 + 16c_g c_d^2 c_m^3 - c_d^2(c_d^2 + 8c_g^2)c_m^2 + c_d^6 = 0. \quad (\text{A.8})$$

For $t > 0$, points A, B, C are defined by:

1. $x_A(t) = c_g t$
2. $x_B(t) = (u_m - c_m)t = (2c_g - 3c - m)$
3. $x_C(t) = v_c t$

as resume we get,

$$(h, u) = \begin{cases} (h_g, 0) & \text{if } x \leq x_A(t) \\ \left(\frac{4}{9g}(c_g - \frac{x}{2t}), \frac{2}{3}(\frac{x}{t} + c_g)\right) & \text{if } x_A(t) \leq x \leq x_B(t) \\ (h_m, 2(c_g - c_m)) & \text{if } x_B(t) \leq x \leq x_C(t) \\ (h_d, 0) & \text{if } x \leq x_C(t) \end{cases} \quad (\text{A.9})$$

A.1.2 Oscillation in Paraboloid

The oscillation in Paraboloid is a standard test case which is used to confirm the convergence and the robustness of the scheme for the dry-wet problem with non-flat topography. Here, an analytical solution of oscillation in Paraboloid is available. This problem was introduced by Thacker in [44]. First, let we define the initial conditions for the problem such as,

$$z_{\text{ini}}(x) = \frac{h_0}{a^2} \left(x - \frac{L}{2}\right)^2 - h_0, \quad (\text{A.10})$$

$$u_{\text{ini}}(x) = 0, \quad (\text{A.11})$$

$$h_{\text{ini}}(x) = \begin{cases} -h_0 \left(\frac{1}{a} \left(x - \frac{L}{2}\right) + \frac{\omega}{\sqrt{2gh_0}}\right)^2 + h_0 & \text{for } x_1(0) \leq x \leq x_2(0), \\ 0 & \text{otherwise.} \end{cases} \quad (\text{A.12})$$

APPENDIX A

where $\omega = \sqrt{2gh_0}/(2a)$, the constants are defined as $a = 1$, $h_0 = 0.5$, and $L = 4$. Then the analytical solution by Thacker's is given by

$$h(x, t) = \begin{cases} -h_0 \left(\frac{1}{a} \left(x - \frac{L}{2} \right) + \frac{\omega}{\sqrt{2gh_0}} \cos(2\omega t) \right)^2 + h_0 & \text{for } x_1(t) \leq x \leq x_2(t), \\ 0 & \text{otherwise.} \end{cases} \quad (\text{A.13})$$

$$u(x, t) = \begin{cases} \omega \sin(a\omega t) & \text{for } x_1(t) \leq x \leq x_2(t), \\ 0 & \text{otherwise.} \end{cases} \quad (\text{A.14})$$

where $x_1(t)$ and $x_2(t)$ are the locations of dry-wet interfaces at time t

$$x_1(t) = -\frac{1}{2} \cos(2\omega t) - a + \frac{L}{2}, \quad (\text{A.15})$$

$$x_2(t) = -\frac{1}{2} \cos(2\omega t) + a + \frac{L}{2}. \quad (\text{A.16})$$

APPENDIX B

Appendix B

In this section, we prove that the upwind staggered scheme is consistent in the sense that if the discrete solutions converge and satisfy some reasonable estimates then the limit is a solution of the shallow water equations. This prove is follow the paper of [26, 32], where here the topography is included. First, we need to specify the concept of solution. We set $Q_T := (0, T) \times \Omega$ and $z \in C^1(\bar{\Omega})$.

Let's write the scheme again. We set $\mathcal{M} := \{1, \dots, N_x\}$, $\mathcal{E}_{int} := \{1, \dots, N_x - 1\}$, $\mathcal{E}_b := \{0, N_x\}$, and $\mathcal{E} := \mathcal{E}_{int} \cup \mathcal{E}_b$. First, we give the initial conditions such as,

$$h_i^0 = \frac{1}{\Delta x} \int_{x_{i-\frac{1}{2}}}^{x_{i+\frac{1}{2}}} h_0(x) \, dx, \quad \forall i \in \mathcal{M}, \quad (\text{B.1})$$

$$u_{i+\frac{1}{2}}^0 = \frac{1}{\Delta x} \int_{x_i}^{x_{i+1}} u_0(x) \, dx, \quad \forall i \in \mathcal{E}_{int}. \quad (\text{B.2})$$

The mass conservation equation is discretized with an explicit upwind scheme:

$$h_i^{n+1} - h_i^n + \frac{\Delta t}{\Delta x} (q_{i+\frac{1}{2}}^n - q_{i-\frac{1}{2}}^n) = 0, \quad \forall i \in \mathcal{M} \quad (\text{B.3})$$

where

$$q_{i+\frac{1}{2}}^n := \hat{h}_{i+\frac{1}{2}}^n u_{i+\frac{1}{2}}^n, \quad \hat{h}_{i+\frac{1}{2}}^n := \begin{cases} h_i^n & \text{if } u_{i+\frac{1}{2}}^n \geq 0 \\ h_{i+1}^n & \text{if } u_{i+\frac{1}{2}}^n < 0 \end{cases}, \quad \forall i \in \mathcal{E}. \quad (\text{B.4})$$

The momentum balance equation is discretized with explicit upwind fluxes for the convection term and implicit centered fluxes for the pressure term and topography term:

$$\begin{aligned} h_{i+\frac{1}{2}}^{n+1} u_{i+\frac{1}{2}}^{n+1} - h_{i+\frac{1}{2}}^n u_{i+\frac{1}{2}}^n + \frac{\Delta t}{\Delta x} \left[q_{i+1}^n \hat{u}_{i+1}^n - q_i^n \hat{u}_i^n \right. \\ \left. + \frac{1}{2} g \left[(h_{i+1}^{n+1})^2 - (h_i^{n+1})^2 \right] + g h_{i+\frac{1}{2}}^{n+1} (z_{i+1} - z_i) \right] = 0, \quad \forall i \in \mathcal{E}_{int}, \end{aligned} \quad (\text{B.5})$$

APPENDIX B

where

$$h_{i+\frac{1}{2}}^n := \frac{1}{2} (h_i^n + h_{i+1}^n), \quad \forall i \in \mathcal{E}_{int}, \quad (\text{B.6})$$

$$q_i^n := \frac{1}{2} (q_{i-\frac{1}{2}}^n + q_{i+\frac{1}{2}}^n), \quad \hat{u}_i^n := \begin{cases} u_{i-\frac{1}{2}}^n & \text{if } q_i^n \geq 0 \\ u_{i+\frac{1}{2}}^n & \text{if } q_i^n < 0 \end{cases}, \quad \forall i \in \mathcal{M}.$$

Definition 2. A pair of functions $(h, u) \in L^\infty(Q_T) \times L^\infty(Q_T)$ is a weak solution of (1.1)-(1.2) if, for all test functions $\varphi \in C_c^\infty(Q_T)$,

$$\int_{Q_T} (h \partial_t \varphi + hu \partial_x \varphi) dx dt = 0, \quad (\text{B.7})$$

$$\int_{Q_T} (hu \partial_t \varphi + (hu^2 + \frac{1}{2}gh^2) \partial_x \varphi) dx dt = \int_{Q_T} gh \partial_x z \varphi dx dt. \quad (\text{B.8})$$

Definition 3. A pair of functions $(h, u) \in L^\infty(Q_T) \times L^\infty(Q_T)$ is a weak entropy solution of (1.1)-(1.2) if (h, u) is a weak solution and, for all nonnegative test functions $\varphi \in C_c^\infty(Q_T)$,

$$\int_{Q_T} (\eta(h, hu) \partial_t \varphi + G(h, hu) \partial_x \varphi) dx dt + \int_{Q_T} ghu \partial_x z \varphi dx dt \geq 0, \quad (\text{B.9})$$

where the entropy η and the entropy flux G are defined by

$$\eta(h, hu) := \frac{1}{2} hu^2 + \frac{1}{2} gh^2.$$

$$G(h, hu) := \left(\frac{1}{2} hu^2 + gh^2 \right) u.$$

We consider a sequence of discretizations indexed by $k \in \mathbb{N}$. In the k -th discretization, the domain Ω is divided in $N_x^{(k)}$ intervals of length $\Delta x^{(k)}$ and the time interval $[0, T]$ in $N_t^{(k)}$ steps of length $\Delta t^{(k)}$. We assume that the meshsize $\Delta x^{(k)}$ and the time step $\Delta t^{(k)}$ tend to zero when k tend to infinity. We define the approximate solutions $h^{(k)} : Q_T \rightarrow \mathbb{R}$ and $u^{(k)} : Q_T \rightarrow \mathbb{R}$ such that

$$\begin{aligned} h^{(k)}(t, x) &= h_i^n && \text{if } t \in [t^n, t^{n+1}), x \in [x_{i-\frac{1}{2}}, x_{i+\frac{1}{2}}] \\ u^{(k)}(t, x) &= u_{i+\frac{1}{2}}^n && \text{if } t \in [t^n, t^{n+1}), x \in [x_i, x_{i+1}] \\ \tilde{h}^{(k)}(t, x) &= h_i^{n+1} && \text{if } t \in (t^n, t^{n+1}], x \in [x_{i-\frac{1}{2}}, x_{i+\frac{1}{2}}] \\ \tilde{u}^{(k)}(t, x) &= u_{i+\frac{1}{2}}^{n+1} && \text{if } t \in (t^n, t^{n+1}], x \in [x_i, x_{i+1}] \end{aligned}$$

APPENDIX B

Let us define the discrete norms

$$\|h^{(k)}\|_{k,BV_x} := \sum_{n=0}^{N_t^{(k)}} \sum_{i=1}^{N_x^{(k)}-1} \Delta t^{(k)} |h_{i+1}^n - h_i^n| \quad (\text{B.10})$$

$$\|h^{(k)}\|_{k,BV_t} := \sum_{n=0}^{N_t^{(k)}-1} \sum_{i=1}^{N_x^{(k)}} \Delta x^{(k)} |h_i^{n+1} - h_i^n| \quad (\text{B.11})$$

Definition 4. (Interpolate one-dimensional meshes).

Let Ω be an open bounded interval of \mathbb{R} and let \mathcal{M} be a mesh over Ω . For all nonnegative test functions $\varphi \in C_c^\infty(Q_T)$, $0 \leq n \leq N_t$ and $i \in \mathcal{M}$, we set $\varphi_i^n = \varphi(x_i, t^n)$, with x_i the mass center of i . The interpolate $\varphi_{\mathcal{M}}$ of φ on the mesh \mathcal{M} is defined by:

$$\begin{aligned} \varphi_{\mathcal{M}}(0, x) &= \varphi_i^0 \quad \text{if } x \in [x_{i-\frac{1}{2}}, x_{i+\frac{1}{2}}), \\ \varphi_{\mathcal{M}}(t, x) &= \varphi_i^{n+1} \quad \text{if } t \in (t^n, t^{n+1}], x \in [x_{i-\frac{1}{2}}, x_{i+\frac{1}{2}}). \end{aligned}$$

The time discrete derivative of $\varphi_{\mathcal{M}}$ is given by:

$$\bar{\partial}_t \varphi_{\mathcal{M}}(t, x) = \frac{\varphi_i^{n+1} - \varphi_i^n}{\Delta t} \quad \text{if } t \in (t^n, t^{n+1}], x \in [x_{i-\frac{1}{2}}, x_{i+\frac{1}{2}}),$$

and its space discrete derivative by:

$$\bar{\partial}_x \varphi_{\mathcal{M}}(t, x) = \frac{\varphi_{i+1}^{n+1} - \varphi_i^{n+1}}{\Delta x} \quad \text{if } t \in (t^n, t^{n+1}], x \in [x_i, x_{i+1}).$$

For $0 \leq n \leq N_t$ and $i \in \mathcal{E}_{int}$, we set $\varphi_{i-\frac{1}{2}}^n = \varphi(x_{i-\frac{1}{2}}, t^n)$. The interpolate $\varphi_{\mathcal{E}_{int}}$ of φ on the mesh \mathcal{E}_{int} is defined by:

$$\begin{aligned} \varphi_{\mathcal{E}_{int}}(0, x) &= \varphi_{i-\frac{1}{2}}^0 \quad \text{if } x \in [x_{i-1}, x_i), \\ \varphi_{\mathcal{E}_{int}}(t, x) &= \varphi_{i-\frac{1}{2}}^{n+1} \quad \text{if } t \in (t^n, t^{n+1}], x \in [x_{i-1}, x_i). \end{aligned}$$

The time discrete derivative of $\varphi_{\mathcal{E}_{int}}$ is given by:

$$\bar{\partial}_t \varphi_{\mathcal{E}_{int}}(t, x) = \frac{\varphi_{i-\frac{1}{2}}^{n+1} - \varphi_{i-\frac{1}{2}}^n}{\Delta t} \quad \text{if } t \in (t^n, t^{n+1}], x \in [x_{i-1}, x_i),$$

and its space discrete derivative by:

$$\bar{\partial}_x \varphi_{\mathcal{E}_{int}}(t, x) = \frac{\varphi_{i+\frac{1}{2}}^{n+1} - \varphi_{i-\frac{1}{2}}^{n+1}}{\Delta x} \quad \text{if } t \in (t^n, t^{n+1}], x \in [x_{i-\frac{1}{2}}, x_{i+\frac{1}{2}}).$$

Assumption 4. There exist constants C , independant of the discretization, such that

$$0 < h^{(k)} \leq C, \quad |u^{(k)}| \leq C, \quad (\text{B.12})$$

and

$$\|h^{(k)}\|_{k, BV_x} + \|u^{(k)}\|_{k, BV_x} \leq C. \quad (\text{B.13})$$

Assumption 5. There exist a constant C , independent of the discretization, such that

$$\|h^{(k)}\|_{k, BV_t} \leq C. \quad (\text{B.14})$$

Assumption 6. The sequence $(\Delta x^{(k)}, \Delta t^{(k)})_{k \in \mathbb{N}}$ is such that

$$\lim_{k \rightarrow +\infty} \frac{\Delta t^{(k)}}{\Delta x^{(k)}} = 0. \quad (\text{B.15})$$

B.1 Consistency of the scheme

Theorem 2. If the sequence $(h^{(k)}, u^{(k)}, \tilde{h}^{(k)})$ satisfies the estimates of Assumption 4 and converges in $L^p(Q_T) \times L^p(Q_T)$, with $p \in [1, +\infty)$, then its limit (h, u) is a weak solution of (1.1)-(1.2) and satisfy the system (B.7)-(B.8).

Proof. The proof consists in passing to the limit in the discrete mass equation, the discrete momentum equation, and the discrete entropy balance. The only difference with the proof of [26] is the presence of topography terms in the discrete momentum equation and the discrete entropy balance.

Let $\varphi \in C_c^\infty(Q_T)$, $k \in \mathbb{N}$, $\Delta x^{(k)}$ and $\Delta t^{(k)}$ be given. For simplicity, dropping for short the superscript (k) and thanks to the regularity of φ , the interpolate discrete functions φ_M , $\bar{\partial}_t \varphi_M$ and $\bar{\partial}_x \varphi_M$ respectively defined in Definition 4 in converge in $L^p(Q_T)$, with $p \in [1, +\infty)$, to φ , $\partial_t \varphi$ and $\partial_x \varphi$ respectively. In addition, $\varphi_M(\cdot, 0)$ converges to $\varphi(\cdot, 0)$ in $L^p(\Omega)$, with $p \in [1, +\infty)$. Since the support φ is compact in Q_T , for k large enough, the interpolate of φ vanishes at the boundary cells and at the last time step(s); hereafter, systematically assume that we are in this case.

APPENDIX B

B.1.1 Mass balance Equation

Let us multiply the first equation (B.3) of the scheme by $\Delta t \varphi_i^{n+1}$, and sum the result for $0 \leq n \leq N_t - 1$ and $i \in \mathcal{M}$ to obtain $T_1^{(k)} + T_2^{(k)} = 0$ with

$$\begin{aligned} T_1^{(k)} &= \sum_{n=0}^{N_t-1} \sum_{i=1}^{N_x} \Delta x (h_i^{n+1} - h_i^n) \varphi_i^{n+1}, \\ T_2^{(k)} &= \sum_{n=0}^{N_t-1} \sum_{i=1}^{N_x} \Delta t (q_{i+\frac{1}{2}}^n - q_{i-\frac{1}{2}}^n) \varphi_i^{n+1}. \end{aligned}$$

Reordering the sum $T_1^{(k)}$ yields:

$$T_1^{(k)} = - \sum_{n=0}^{N_t-1} \Delta t \sum_{i=1}^{N_x} \Delta x h_i^n \frac{\varphi_i^{n+1} - \varphi_i^n}{\Delta t} - \sum_{i=1}^{N_x} \Delta x h_i^0 \varphi_i^0,$$

so that:

$$T_1^{(k)} = - \int_{Q_T} h^{(k)} \bar{\partial}_t \varphi_{\mathcal{M}} \, dx dt - \int_{\Omega} (h^{(k)})^0(x) \varphi_{\mathcal{M}}(x, 0) \, dx,$$

The boundedness of h_0 and the definition of initial condition (B.1) for the scheme, it ensures that $((h^{(k)})^0)_{k \in \mathbb{N}}$ converges to h_0 in $L^\infty(\Omega)$. Thus we obtain

$$\lim_{k \rightarrow +\infty} T_1^{(k)} = - \int_{Q_T} \bar{h} \partial_t \varphi \, dx dt - \int_{\Omega} h_0(x) \varphi(x, 0) \, dx. \quad (\text{B.16})$$

Using the expression flux $q_{i-\frac{1}{2}}$, reordering $T_2^{(k)}$, we get,

$$T_2^{(k)} = - \sum_{n=0}^{N_t-1} \Delta t \sum_{i=1}^{N_x} \Delta x h_{i-\frac{1}{2}}^n u_{i-\frac{1}{2}}^n \frac{\varphi_i^{n+1} - \varphi_{i-1}^{n+1}}{\Delta x}$$

since $h_{i-\frac{1}{2}}^n$ is the upwind approximation of h^n at the interface $i - \frac{1}{2}$, we can rewrite $T_2^{(k)} = \mathcal{T}_2^{(k)} + \mathcal{R}_2^{(k)}$

$$\mathcal{T}_2^{(k)} = - \sum_{n=0}^{N_t-1} \Delta t \sum_{i=1}^{N_x} \frac{\Delta x}{2} (h_i^n + h_{i-1}^n) u_{i-\frac{1}{2}}^n \frac{\varphi_i^{n+1} - \varphi_{i-1}^{n+1}}{\Delta x}$$

$$\mathcal{R}_2^{(k)} = - \sum_{n=0}^{N_t-1} \Delta t \sum_{i=1}^{N_x} (h_{i-1}^n - h_i^n) \frac{\Delta x}{2} ((u_{i-\frac{1}{2}}^n)^- + (u_{i-\frac{1}{2}}^n)^+) \frac{\varphi_i^{n+1} - \varphi_{i-1}^{n+1}}{\Delta x}$$

where for $a \in \mathfrak{R}$, $a^+ = \max(a, 0)$ and $a^- = -\min(a, 0)$ (so $a = a^+ + a^-$). We have

APPENDIX B

the term $\mathcal{T}_2^{(k)}$:

$$\mathcal{T}_2^{(k)} = - \int_{Q_T} h^{(k)} u^{(k)} \bar{\partial}_t \varphi_{\mathcal{M}} \, dx dt$$

and therefore,

$$\lim_{k \rightarrow +\infty} \mathcal{T}_2^{(k)} = - \int_{Q_T} \bar{h} \bar{u} \partial_x \varphi \, dx dt.$$

The remainder term $\mathcal{R}_2^{(k)}$ is bounded as follows, with $C_\varphi = ||\partial \varphi||_{L^\infty(Q_T)}$:

$$\begin{aligned} |\mathcal{R}_2^{(k)}| &\leq C_\varphi \sum_{n=0}^{N_t-1} \Delta t \sum_{i=1}^{N_x} |h_{i-1}^n - h_i^n| |\Delta x| |u_{i-\frac{1}{2}}^n| \\ &\leq C_\varphi \|h^{(k)}\|_{k, BV_x} \|u^{(k)}\|_{L^\infty(Q_T)} \Delta x^{(k)} \end{aligned}$$

where $|\mathcal{R}_2^{(k)}| \rightarrow 0$, as $k \rightarrow +\infty$, so we have

$$\lim_{k \rightarrow +\infty} T_2^{(k)} = \lim_{k \rightarrow +\infty} \mathcal{T}_2^{(k)}.$$

Gather equations (B.16) and (B.1.1), we have

$$- \int_{Q_T} (\bar{h} \partial_t \varphi + \bar{h} \bar{u} \partial_x \varphi) \, dx dt - \int_{\Omega} h_0(x) \varphi(x, 0) \, dx = 0,$$

then we get,

$$\int_{Q_T} (\partial_t h \varphi + \partial_x h u \varphi) \, dx dt = 0. \quad (\text{B.17})$$

B.1.2 Momentum balance equations

Let us multiply the first equation (B.5) of the scheme by $\Delta t \varphi_{i-\frac{1}{2}}^{n+1}$, and sum the result for $0 \leq n \leq N_t - 1$ and $i \in \mathcal{E}_{\text{int}}$ to obtain $T_1^{(k)} + T_2^{(k)} + T_3^{(k)} + T_4^{(k)} = 0$ with

$$\begin{aligned} T_1^{(k)} &= \sum_{n=0}^{N_t-1} \sum_{i=1}^{N_x-1} \Delta x \left(h_{i+\frac{1}{2}}^{n+1} u_{i+\frac{1}{2}}^{n+1} - h_{i+\frac{1}{2}}^n u_{i+\frac{1}{2}}^n \right) \varphi_{i+\frac{1}{2}}^{n+1}, \\ T_2^{(k)} &= \sum_{n=0}^{N_t-1} \Delta t \sum_{i=1}^{N_x-1} \left(q_{i+1}^n u_{i+1}^n - q_i^n u_i^n \right) \varphi_{i+\frac{1}{2}}^{n+1}, \\ T_3^{(k)} &= \sum_{n=0}^{N_t-1} \Delta t \sum_{i=1}^{N_x-1} \left(\frac{1}{2} g h_{i+1}^{n+1} - \frac{1}{2} g h_i^{n+1} \right) \varphi_{i+\frac{1}{2}}^{n+1}, \\ T_4^{(k)} &= - \sum_{n=0}^{N_t-1} \Delta t \sum_{i=1}^{N_x-1} g h_{i+\frac{1}{2}}^{n+1} (z_{i+1} - z_i) \varphi_{i+\frac{1}{2}}^{n+1}. \end{aligned}$$

APPENDIX B

Reordering the sums, we get for $T_1^{(k)}$:

$$T_1^{(k)} = - \sum_{n=0}^{N_t-1} \Delta t \sum_{i=1}^{N_x-1} \Delta x h_{i+\frac{1}{2}}^n u_{i+\frac{1}{2}}^n \frac{\varphi_{i+\frac{1}{2}}^{n+1} - \varphi_{i+\frac{1}{2}}^n}{\Delta t} - \sum_{i=1}^{N_x-1} \Delta x h_{i+\frac{1}{2}}^0 u_{i+\frac{1}{2}}^0 \varphi_{i+\frac{1}{2}}^1$$

thanks to relations (B.6), of the water height at the interface, we have

$$T_1^{(k)} = - \sum_{n=0}^{N_t-1} \Delta t \sum_{i=1}^{N_x-1} \frac{\Delta x}{2} (h_i^n + h_{i+1}^n) u_{i+\frac{1}{2}}^n \frac{\varphi_{i+\frac{1}{2}}^{n+1} - \varphi_{i+\frac{1}{2}}^n}{\Delta t} - \sum_{i=1}^{N_x-1} \frac{\Delta x}{2} (h_i^0 + h_{i+1}^0) u_{i+\frac{1}{2}}^0 \varphi_{i+\frac{1}{2}}^1$$

so that:

$$T_1^{(k)} = - \int_{Q_T} h^{(k)} u^{(k)} \bar{\partial}_t \varphi_{\mathcal{E}_{\text{int}}} \, dx dt - \int_{\Omega} (h^{(k)})^0(x) (u^{(k)})^0(x) \varphi_{\mathcal{E}_{\text{int}}}(x, 0) \, dx$$

From the definition (B.1) and (B.2), of the initial conditions and the assumed regularity of h_0 and u_0 , the sequence $((h^{(k)})^0)_{k \in \mathbb{N}}$ and $((u^{(k)})^0)_{k \in \mathbb{N}}$ converge in $L^\infty(\Omega)$, to h_0 and u_0 respectively. For the convergence assumption for the sequence of discrete solutions, we therefore obtain

$$\lim_{k \rightarrow +\infty} T_1^{(k)} = - \int_{Q_T} \bar{h} \bar{u} \partial_t \varphi \, dx dt - \int_{\Omega} h_0(x) u_0(x) \varphi(x, 0) \, dx. \quad (\text{B.18})$$

Let us now turn to $T_2^{(k)}$. Reordering the sums and using the definition of the mass fluxes at the center cell, we get:

$$\begin{aligned} T_2^{(k)} &= - \sum_{n=0}^{N_t-1} \Delta t \sum_{i=1}^{N_x-1} q_i^n u_i^n \left(\varphi_{i+\frac{1}{2}}^{n+1} - \varphi_{i-\frac{1}{2}}^{n+1} \right), \\ &= - \frac{1}{2} \sum_{n=0}^{N_t-1} \Delta t \sum_{i=1}^{N_x-1} \left(\hat{h}_{i+\frac{1}{2}}^n u_{i+\frac{1}{2}}^n + \hat{h}_{i-\frac{1}{2}}^n u_{i-\frac{1}{2}}^n \right) u_i^n \left(\varphi_{i+\frac{1}{2}}^{n+1} - \varphi_{i-\frac{1}{2}}^{n+1} \right). \end{aligned}$$

Using the relation

$$\int_{Q_T} h^{(k)} (u^{(k)})^2 \bar{\partial}_t \varphi_{\mathcal{E}_{\text{int}}} \, dx dt = \frac{1}{2} \sum_{n=0}^{N_t-1} \Delta t \sum_{i=1}^{N_x-1} h_i^n \left[(u_{i-\frac{1}{2}}^n)^2 + (u_{i+\frac{1}{2}}^n)^2 \right] \left(\varphi_{i+\frac{1}{2}}^{n+1} - \varphi_{i-\frac{1}{2}}^{n+1} \right),$$

we can rewrite the term $T_2^{(k)}$ as

$$T_2^{(k)} = - \int_{Q_T} h^{(k)} (u^{(k)})^2 \bar{\partial}_t \varphi_{\mathcal{E}_{\text{int}}} \, dx dt + \mathcal{R}_2^{(k)},$$

APPENDIX B

where

$$\mathcal{R}_2^{(k)} = -\frac{1}{2} \sum_{n=0}^{N_t-1} \Delta t \sum_{i=1}^{N_x-1} \left[\left(\hat{h}_{i+\frac{1}{2}}^n u_{i+\frac{1}{2}}^n + \hat{h}_{i-\frac{1}{2}}^n u_{i-\frac{1}{2}}^n \right) u_i^n - h_i^n \left((u_{i-\frac{1}{2}}^n)^2 + (u_{i+\frac{1}{2}}^n)^2 \right) \right] \\ \left(\varphi_{i+\frac{1}{2}}^{n+1} - \varphi_{i-\frac{1}{2}}^{n+1} \right).$$

Let us split $\mathcal{R}_2^{(k)} = \mathcal{R}_{21}^{(k)} + \mathcal{R}_{22}^{(k)}$ with

$$\mathcal{R}_{21}^{(k)} = -\frac{1}{2} \sum_{n=0}^{N_t-1} \Delta t \sum_{i=1}^{N_x-1} u_{i-\frac{1}{2}}^n \left(\hat{h}_{i-\frac{1}{2}}^n u_i^n - h_i^n u_{i-\frac{1}{2}}^n \right) \left(\varphi_{i+\frac{1}{2}}^{n+1} - \varphi_{i-\frac{1}{2}}^{n+1} \right), \\ \mathcal{R}_{22}^{(k)} = -\frac{1}{2} \sum_{n=0}^{N_t-1} \Delta t \sum_{i=1}^{N_x-1} u_{i+\frac{1}{2}}^n \left(\hat{h}_{i+\frac{1}{2}}^n u_i^n - h_i^n u_{i+\frac{1}{2}}^n \right) \left(\varphi_{i+\frac{1}{2}}^{n+1} - \varphi_{i-\frac{1}{2}}^{n+1} \right).$$

First we study $\mathcal{R}_{21}^{(k)}$. Thanks to the identity $2(ab+cd) = (a-c)(b+d)+(a+c)(b+d)$, $\forall (a, b, c, d) \in \mathbb{R}^4$ and (B.4) of the upwind value $\hat{h}_{i-\frac{1}{2}}^n$, so applying to the term $\left(\hat{h}_{i-\frac{1}{2}}^n u_i^n - h_i^n u_{i-\frac{1}{2}}^n \right)$ and using the fact that the quantities $\hat{h}_{i-\frac{1}{2}}^n - h_i^n$ and $u_{i-\frac{1}{2}}^n - u_i^n$ are either zero or differences of the density at two neighbouring cells and the velocity at two two neighbouring faces respectively, we get that:

$$|\mathcal{R}_{21}^{(k)}| = \frac{1}{2} \left| \sum_{n=0}^{N_t-1} \Delta t \sum_{i=1}^{N_x-1} u_{i-\frac{1}{2}}^n \left(\hat{h}_{i-\frac{1}{2}}^n u_i^n - h_i^n u_{i-\frac{1}{2}}^n \right) \left(\varphi_{i+\frac{1}{2}}^{n+1} - \varphi_{i-\frac{1}{2}}^{n+1} \right) \right|, \\ \leq C_\varphi \|u^{(k)}\|_{L^\infty(Q_T)} \left[\|h^{(k)}\|_{k, BV_x} \|u^{(k)}\|_{L^\infty(Q_T)} + \|h^{(k)}\|_{L^\infty(Q_T)} \|u^{(k)}\|_{k, BV_x} \right] \Delta x^{(k)}$$

where the real number C_φ only depends on φ . The same estimate holds for $\mathcal{R}_{22}^{(k)}$, like

$$|\mathcal{R}_{22}^{(k)}| = \frac{1}{2} \left| \sum_{n=0}^{N_t-1} \Delta t \sum_{i=1}^{N_x-1} u_{i+\frac{1}{2}}^n \left(\hat{h}_{i+\frac{1}{2}}^n u_i^n - h_i^n u_{i+\frac{1}{2}}^n \right) \left(\varphi_{i+\frac{1}{2}}^{n+1} - \varphi_{i-\frac{1}{2}}^{n+1} \right) \right|, \\ \leq C_\varphi \|u^{(k)}\|_{L^\infty(Q_T)} \left[\|h^{(k)}\|_{k, BV_x} \|u^{(k)}\|_{L^\infty(Q_T)} + \|h^{(k)}\|_{L^\infty(Q_T)} \|u^{(k)}\|_{k, BV_x} \right] \Delta x^{(k)}.$$

Finally we get $|\mathcal{R}_2^{(k)}| = |\mathcal{R}_{21}^{(k)}| + |\mathcal{R}_{22}^{(k)}| \rightarrow 0$, as $k \rightarrow +\infty$ and thus we get

$$\lim_{k \rightarrow +\infty} T_2^{(k)} = - \int_{Q_T} \bar{h} \bar{u}^2 \partial_x \varphi \, dx dt. \quad (\text{B.19})$$

APPENDIX B

Now, we study $T_3^{(k)}$, consider the i point of $T_3^{(k)}$, we have

$$\begin{aligned} T_3^{(k)} &= -\frac{g}{2} \sum_{n=0}^{N_t-1} \Delta t \sum_{i=1}^{N_x-1} (h_i^{n+1})^2 \left(\varphi_{i+\frac{1}{2}}^{n+1} - \varphi_{i-\frac{1}{2}}^{n+1} \right), \\ &= \underbrace{-\frac{g}{2} \sum_{n=0}^{N_t-1} \Delta t \sum_{i=1}^{N_x-1} (h_i^n)^2 \left(\varphi_{i+\frac{1}{2}}^{n+1} - \varphi_{i-\frac{1}{2}}^{n+1} \right)}_{\mathcal{T}_3^{(k)}} - \underbrace{\frac{g}{2} \sum_{n=0}^{N_t-1} \Delta t \sum_{i=1}^{N_x-1} ((h_i^{n+1})^2 - (h_i^n)^2) \left(\varphi_{i+\frac{1}{2}}^{n+1} - \varphi_{i-\frac{1}{2}}^{n+1} \right)}_{\mathcal{R}_3^{(k)}} \end{aligned}$$

thus we obtain $T_3^{(k)} = \mathcal{T}_3^{(k)} + \mathcal{R}_3^{(k)}$ with

$$\mathcal{T}_3^{(k)} = -\frac{g}{2} \sum_{n=0}^{N_t-1} \Delta t \sum_{i=1}^{N_x-1} (h_i^n)^2 \left(\varphi_{i+\frac{1}{2}}^{n+1} - \varphi_{i-\frac{1}{2}}^{n+1} \right),$$

and

$$\mathcal{R}_3^{(k)} = -\frac{g}{2} \sum_{n=0}^{N_t-1} \Delta t \sum_{i=1}^{N_x-1} ((h_i^{n+1})^2 - (h_i^n)^2) \left(\varphi_{i+\frac{1}{2}}^{n+1} - \varphi_{i-\frac{1}{2}}^{n+1} \right).$$

The remainder term read

$$\mathcal{R}_3^{(k)} = -\frac{g}{2} \sum_{n=1}^{N_t-1} \Delta t \sum_{i=1}^{N_x-1} (h_i^n)^2 \left[\left(\varphi_{i+\frac{1}{2}}^{n+1} - \varphi_{i-\frac{1}{2}}^{n+1} \right) - \left(\varphi_{i+\frac{1}{2}}^n - \varphi_{i-\frac{1}{2}}^n \right) \right] + \frac{g}{2} \Delta t \sum_{i=1}^{N_x-1} (h_i^0)^2 \left(\varphi_{i+\frac{1}{2}}^1 - \varphi_{i-\frac{1}{2}}^1 \right),$$

and thus

$$|\mathcal{R}_3^{(k)}| \leq \frac{g}{2} C_\varphi |\Omega| \left[(T+1) \Delta t^{(k)} + \Delta x^{(k)} \right] \|h^{(k)}\|_{L^\infty(Q_T)}^2,$$

where the real number C_φ only depends on (the first and second derivative of) φ . Thus $|\mathcal{R}_3^{(k)}| \rightarrow 0$, as $k \rightarrow +\infty$. And since

$$\mathcal{T}_3^{(k)} = -\frac{g}{2} \int_{Q_T} (h^{(k)})^2 \bar{\partial}_x \varphi_{\mathcal{E}_{\text{int}}} \, dx dt, \quad (\text{B.20})$$

we obtain that

$$\lim_{k \rightarrow +\infty} T_3^{(k)} = - \int_{Q_T} \frac{1}{2} g \bar{h}^2 \partial_x \varphi \, dx dt. \quad (\text{B.21})$$

Finally we can study for $T_4^{(k)}$. We obtain,

$$T_4^{(k)} = - \int_{Q_T} g \tilde{h}^{(k)} \partial_x z^{(k)} \bar{\varphi}_{\mathcal{E}_{\text{int}}} \, dx dt,$$

and taking the limit,

$$\lim_{k \rightarrow +\infty} T_4^{(k)} = - \int_{Q_T} g \bar{h} \partial_x \bar{z} \varphi \, dxdt. \quad (\text{B.22})$$

Gather equations (B.18-B.22), we have

$$\begin{aligned} & - \int_{Q_T} \left(\bar{h} \bar{u} \partial_t \varphi + (\bar{h} \bar{u}^2 + \frac{1}{2} g \bar{h}^2) \partial_x \varphi \right) \, dxdt - \int_{\Omega} h_0(x) u_0(x) \varphi(x, 0) \, dx \\ & \quad - \int_{Q_T} g \bar{h} \partial_x \bar{z} \varphi \, dxdt = 0, \end{aligned}$$

then we get,

$$\int_{Q_T} \left(\partial_t h u \varphi + \partial_x (h u + \frac{1}{2} g h^2) \varphi \right) \, dxdt = \int_{Q_T} g h \partial_x z \varphi \, dxdt. \quad (\text{B.23})$$

□

B.2 Consistency of the Entropy balance

Theorem 3. *Under the assumption of Theorem 2, and if $(h^{(k)}, u^{(k)}, \tilde{h}^{(k)}, \tilde{u}^{(k)})$ satisfies Assumptions 4, 5 and 6, then (h, u) is a weak entropy solution of (1.1)-(1.2) and satisfy the entropy condition (B.9).*

Proof. Let $\varphi \in C_c^\infty(Q_T)$, $k \in \mathbb{N}$, $\Delta x^{(k)}$ and $\Delta t^{(k)}$ be given. For simplicity, dropping for short the superscript $^{(k)}$ and thanks to the regularity of φ , the interpolate discrete functions φ_M , $\bar{\partial}_t \varphi_M$ and $\bar{\partial}_x \varphi_M$ respectively defined in Definition 4 in converge in $L^p(Q_T)$, with $p \in [1, +\infty)$, to φ , $\partial_t \varphi$ and $\partial_x \varphi$ respectively. In addition, $\varphi_M(\cdot, 0)$ converges to $\varphi(\cdot, 0)$ in $L^p(\Omega)$, with $p \in [1, +\infty)$. Since the support φ is compact in Q_T , for k large enough, the interpolate of φ vanishes at the boundary cells and at the last time step(s); hereafter, systematically assume that we are in this case.

Let us multiply the kinetic balance equations (1.52)-(1.53) by $\Delta t \varphi_{i+\frac{1}{2}}^{n+1}$ and the elastic potential balance (1.61)-(1.62) of the scheme by $\Delta t \varphi_i^{n+1}$, and sum over the edges and cells respectively and over the time step. Let $\mathcal{H}_i^n := \frac{1}{2} g(h_i^n)^2$ and $\mathcal{H}_{i+\frac{1}{2}}^n := \frac{1}{2} g(\hat{h}_i^n)^2$ where \hat{h}_i^n is define by (B.4), thus we obtain,

$$T_1^{(k)} + T_2^{(k)} + T_3^{(k)} + T_4^{(k)} + \tilde{T}_1^{(k)} + \tilde{T}_2^{(k)} + \tilde{T}_3^{(k)} = -R^{(k)} - \tilde{R}^{(k)}$$

APPENDIX B

where

(Kinetic terms)

$$\begin{aligned}
T_1^{(k)} &= \frac{1}{2} \sum_{n=0}^{N_t-1} \sum_{i \in \mathcal{E}_{int}} \Delta x \left(h_{i+\frac{1}{2}}^{n+1} (u_{i+\frac{1}{2}}^{n+1})^2 - h_{i+\frac{1}{2}}^n (u_{i+\frac{1}{2}}^n)^2 \right) \varphi_{i+\frac{1}{2}}^{n+1}, \\
T_2^{(k)} &= \frac{1}{2} \sum_{n=0}^{N_t-1} \Delta t \sum_{i \in \mathcal{E}_{int}} \left(q_{i+1}^n (\hat{u}_{i+1}^n)^2 - q_i^n (\hat{u}_i^n)^2 \right) \varphi_{i+\frac{1}{2}}^{n+1}, \\
T_3^{(k)} &= \sum_{n=0}^{N_t-1} \Delta t \sum_{i \in \mathcal{E}_{int}} \left(\mathcal{H}_{i+1}^{n+1} - \mathcal{H}_i^{n+1} \right) u_{i+\frac{1}{2}}^{n+1} \varphi_{i+\frac{1}{2}}^{n+1}, \\
T_4^{(k)} &= g \sum_{n=0}^{N_t-1} \Delta t \sum_{i \in \mathcal{E}_{int}} h_{i+\frac{1}{2}}^{n+1} u_{i+\frac{1}{2}}^{n+1} (z_{i+1} - z_i) \varphi_{i+\frac{1}{2}}^{n+1}, \\
R^{(k)} &= \sum_{n=0}^{N_t-1} \Delta t \sum_{i \in \mathcal{E}_{int}} R_{i+\frac{1}{2}}^{n+1} \varphi_{i+\frac{1}{2}}^{n+1},
\end{aligned}$$

(Potential terms)

$$\begin{aligned}
\tilde{T}_1^{(k)} &= \sum_{n=0}^{N_t-1} \sum_{i \in \mathcal{M}} \Delta x \left(\mathcal{H}_i^{n+1} - \mathcal{H}_i^n \right) \varphi_i^{n+1}, \\
\tilde{T}_2^{(k)} &= \sum_{n=0}^{N_t-1} \Delta t \sum_{i \in \mathcal{M}} \left(\mathcal{H}_{i+\frac{1}{2}}^n u_{i+\frac{1}{2}}^n - \mathcal{H}_{i-\frac{1}{2}}^n u_{i-\frac{1}{2}}^n \right) \varphi_i^{n+1}, \\
\tilde{T}_3^{(k)} &= \sum_{n=0}^{N_t-1} \Delta t \sum_{i \in \mathcal{M}} \mathcal{H}_i^n \left(u_{i+\frac{1}{2}}^n - u_{i-\frac{1}{2}}^n \right) \varphi_i^{n+1}, \\
\tilde{R}^{(k)} &= \sum_{n=0}^{N_t-1} \Delta t \sum_{i \in \mathcal{E}_{int}} R_i^{n+1} \varphi_i^{n+1},
\end{aligned}$$

Reordering the sum $T_1^{(k)}$ (integral by parts) yields:

$$T_1^{(k)} = -\frac{1}{2} \sum_{n=0}^{N_t-1} \sum_{i \in \mathcal{E}_{int}} \Delta x h_{i+\frac{1}{2}}^n (u_{i+\frac{1}{2}}^n)^2 \frac{\varphi_i^{n+1} - \varphi_i^n}{\Delta t} - \frac{1}{2} \sum_{i \in \mathcal{E}_{int}} h_{i+\frac{1}{2}}^0 (u_{i+\frac{1}{2}}^0)^2 \varphi_i^1 \Delta x$$

using relation of $h_{i+\frac{1}{2}}^n : \frac{1}{2}(h_{i+1}^n + h_i^n)$, we have

$$T_1^{(k)} = -\frac{1}{2} \sum_{n=0}^{N_t-1} \sum_{i \in \mathcal{E}_{int}} \Delta x \frac{1}{2} (h_{i+1}^n + h_i^n) (u_{i+\frac{1}{2}}^n)^2 \frac{\varphi_i^{n+1} - \varphi_i^n}{\Delta t} - \frac{1}{2} \sum_{i \in \mathcal{E}_{int}} \frac{1}{2} (h_{i+1}^0 + h_i^0) (u_{i+\frac{1}{2}}^0)^2 \varphi_i^1 \Delta x$$

APPENDIX B

reordering the summation, so that:

$$T_1^{(k)} = - \int_{Q_T} \frac{1}{2} h^{(k)} u^{(k)} \bar{\partial}_t \varphi_{\mathcal{E}_{int}} \, dx dt - \int_{\Omega} \frac{1}{2} (h^{(k)})^0(x) ((u^{(k)})^0(x))^2 \varphi_{\mathcal{E}_{int}}(x, 0) \, dx$$

thus we obtain

$$\lim_{k \rightarrow +\infty} T_1^{(k)} = - \int_{Q_T} \frac{1}{2} \bar{h} \bar{u}^2 \partial_t \varphi \, dx dt - \int_{\Omega} \frac{1}{2} h_0(x) u_0(x)^2 \varphi(x, 0) \, dx. \quad (\text{B.24})$$

Let us now turn to the terms $T_2^{(k)}$, reordering the sums, we get

$$T_2^{(k)} = - \frac{1}{2} \sum_{n=0}^{N_t-1} \Delta t \sum_{i \in \mathcal{E}_{int}} q_i^n (\hat{u}_i^n)^2 \left(\varphi_{i+\frac{1}{2}}^{n+1} - \varphi_{i-\frac{1}{2}}^{n+1} \right)$$

By definition $q_i^n := \frac{1}{2}(q_{i-\frac{1}{2}}^n + q_{i+\frac{1}{2}}^n)$, we have

$$T_2^{(k)} = - \frac{1}{4} \sum_{n=0}^{N_t-1} \Delta t \sum_{i \in \mathcal{E}_{int}} (q_{i-\frac{1}{2}}^n + q_{i+\frac{1}{2}}^n) (\hat{u}_i^n)^2 \left(\varphi_{i+\frac{1}{2}}^{n+1} - \varphi_{i-\frac{1}{2}}^{n+1} \right)$$

where we recall that \hat{u}_i^n is equal to either $u_{i-\frac{1}{2}}^n$ or $u_{i+\frac{1}{2}}^n$, depending on the sign of q_i^n .

Let us write $T_2^{(k)} = \mathcal{T}_2^{(k)} + \mathcal{R}_2^{(k)}$, with

$$\begin{aligned} \mathcal{T}_2^{(k)} &= - \frac{1}{4} \sum_{n=0}^{N_t-1} \Delta t \sum_{i \in \mathcal{E}_{int}} h_i^n \left((u_{i-\frac{1}{2}}^n)^3 + (u_{i+\frac{1}{2}}^n)^3 \right) \left(\varphi_{i+\frac{1}{2}}^{n+1} - \varphi_{i-\frac{1}{2}}^{n+1} \right), \\ \mathcal{R}_2^{(k)} &= - \frac{1}{4} \sum_{n=0}^{N_t-1} \Delta t \sum_{i \in \mathcal{E}_{int}} \left[(q_{i-\frac{1}{2}}^n + q_{i+\frac{1}{2}}^n) (\hat{u}_i^n)^2 - h_i^n \left((u_{i-\frac{1}{2}}^n)^3 + (u_{i+\frac{1}{2}}^n)^3 \right) \right] \left(\varphi_{i+\frac{1}{2}}^{n+1} - \varphi_{i-\frac{1}{2}}^{n+1} \right). \end{aligned}$$

for the remainder term, in order to have $u_i^n = u_{i-\frac{1}{2}}^n$, we use notation $i = i - \frac{1}{2} \rightarrow i + \frac{1}{2}$.

We obtain,

$$\begin{aligned} \mathcal{R}_2^{(k)} &= - \frac{1}{4} \sum_{n=0}^{N_t-1} \Delta t \sum_{i \in \mathcal{E}_{int}} \left[(h_{i-\frac{1}{2}}^n u_{i-\frac{1}{2}}^n + h_{i+\frac{1}{2}}^n u_{i+\frac{1}{2}}^n) (\hat{u}_{i-\frac{1}{2}}^n)^2 - h_i^n \left((u_{i-\frac{1}{2}}^n)^3 + (u_{i+\frac{1}{2}}^n)^3 \right) \right] \\ &\quad \left(\varphi_{i+\frac{1}{2}}^{n+1} - \varphi_{i-\frac{1}{2}}^{n+1} \right). \end{aligned}$$

APPENDIX B

Since, for $0 \leq n \leq N_t - 1$ and $i \in \mathcal{M}$,

$$(h_{i-\frac{1}{2}}^n u_{i-\frac{1}{2}}^n + h_{i+\frac{1}{2}}^n u_{i+\frac{1}{2}}^n)(\hat{u}_{i-\frac{1}{2}}^n)^2 - h_i^n \left((u_{i-\frac{1}{2}}^n)^3 + (u_{i+\frac{1}{2}}^n)^3 \right) = -(h_i^n - h_{i-\frac{1}{2}}^n)(u_{i-\frac{1}{2}}^n)^3 \\ + h_i^n u_{i+\frac{1}{2}}^n (u_{i-\frac{1}{2}}^n + u_{i+\frac{1}{2}}^n)(u_{i-\frac{1}{2}}^n - u_{i+\frac{1}{2}}^n) - (h_i^n - h_{i+\frac{1}{2}}^n) u_{i+\frac{1}{2}}^n (u_{i-\frac{1}{2}}^n)^2$$

then we have

$$|\mathcal{R}_2^{(k)}| \leq C_\varphi \Delta x^{(k)} \left[\|h^{(k)}\|_{k, BV_x} \|u^{(k)}\|_{L^\infty(Q_T)}^3 + \|h^{(k)}\|_{L^\infty(Q_T)} \|u^{(k)}\|_{L^\infty(Q_T)}^2 \|u^{(k)}\|_{k, BV_x} \right],$$

where the real number C_φ only depends on φ . Hence $|\mathcal{R}_2^{(k)}| \rightarrow 0$, as $k \rightarrow +\infty$. Finally we have

$$T_2^{(k)} = \mathcal{T}_2^{(k)} + 0, \\ = - \int_{Q_T} \frac{1}{2} h^{(k)} (u^{(k)})^3 \hat{\partial}_x \varphi_{\mathcal{E}_{int}} \, dx dt,$$

and hence:

$$T_2^{(k)} = - \int_{Q_T} \frac{1}{2} \hat{h} \hat{u}^3 \partial_x \varphi \, dx dt.$$

Now we investigate the terms $\tilde{T}_1^{(k)}$ and $\tilde{T}_2^{(k)}$. Reordering the sums in $\tilde{T}_1^{(k)}$ yields:

$$\tilde{T}_1^{(k)} = - \sum_{n=0}^{N_t-1} \Delta t \sum_{i \in \mathcal{M}} \Delta x \mathcal{H}_i^n \frac{(\varphi_i^{n+1} - \varphi_i^n)}{\Delta t} - \sum_{i \in \mathcal{M}} \Delta x \mathcal{H}_i^0 \varphi_i^1$$

so that:

$$\tilde{T}_1^{(k)} = - \int_{Q_T} \mathcal{H}^{(k)} \hat{\partial}_t \varphi_{\mathcal{M}} \, dx dt - \int_{\Omega} (\mathcal{H}^{(k)})^0(x) \varphi_{\mathcal{M}}(x, 0) \, dx, \\ = - \int_{Q_T} \frac{1}{2} g(h^{(k)})^2 \hat{\partial}_t \varphi_{\mathcal{M}} \, dx dt - \int_{\Omega} \frac{1}{2} g((h^{(k)})^0)^2(x) \varphi_{\mathcal{M}}(x, 0) \, dx.$$

The boundedness of h_0 and the definition (B.1) of the initial conditions for the scheme ensures that the sequences $((h^{(k)})^0)_{k \in \mathbb{N}}$ converge to h_0 in $L^p(\Omega)$ for $p \geq 1$. Since, by assumption, the sequence of discrete solutions and of the interpolate time derivatives converge in $L^p(Q_T)$ for $p \geq 1$, we thus obtain:

APPENDIX B

$$\lim_{k \rightarrow +\infty} \tilde{T}_1^{(k)} = - \int_{Q_T} \frac{1}{2} g \bar{h}^2 \partial_t \varphi \, dx dt - \int_{\Omega} \frac{1}{2} g h_0^2(x) \varphi(x, 0) \, dx.$$

Reordering the sums in $\tilde{T}_2^{(k)}$, we get

$$\tilde{T}_2^{(k)} = - \sum_{n=0}^{N_t-1} \Delta t \sum_{i \in \mathcal{M}} \mathcal{H}_{i-\frac{1}{2}}^n u_{i-\frac{1}{2}}^n (\varphi_{i+1}^{n+1} - \varphi_i^{n+1})$$

since $\mathcal{H}_{i-\frac{1}{2}}^n = \frac{1}{2} g h_{i-\frac{1}{2}}^n$ is the upwind approximation of h^n at the interface $i - \frac{1}{2}$, we can rewrite $\tilde{T}_2^{(k)} = \tilde{\mathcal{T}}_2^{(k)} + \tilde{\mathcal{R}}_2^{(k)}$

$$\begin{aligned} \tilde{\mathcal{T}}_2^{(k)} &= - \sum_{n=0}^{N_t-1} \Delta t \sum_{i=1}^{N_x} \frac{\Delta x}{2} (\mathcal{H}_i^n + \mathcal{H}_{i-1}^n) u_{i-\frac{1}{2}}^n \frac{\varphi_i^{n+1} - \varphi_{i-1}^{n+1}}{\Delta x} \\ \tilde{\mathcal{R}}_2^{(k)} &= - \sum_{n=0}^{N_t-1} \Delta t \sum_{i=1}^{N_x} (\mathcal{H}_{i-1}^n - \mathcal{H}_i^n) \left(\frac{\Delta x}{2} (u_{i-\frac{1}{2}}^n)^- + \frac{\Delta x}{2} (u_{i-\frac{1}{2}}^n)^+ \right) \frac{\varphi_i^{n+1} - \varphi_{i-1}^{n+1}}{\Delta x} \end{aligned}$$

We have the term $\tilde{\mathcal{T}}_2^{(k)}$:

$$\tilde{\mathcal{T}}_2^{(k)} = - \int_{Q_T} \frac{1}{2} g (h^{(k)})^2 u^{(k)} \bar{\partial}_t \varphi_{\mathcal{M}} \, dx dt$$

and therefore,

$$\lim_{k \rightarrow +\infty} \tilde{\mathcal{T}}_2^{(k)} = - \int_{Q_T} \frac{1}{2} g \bar{h}^2 \bar{u} \partial_x \varphi \, dx dt$$

The remainder term $\tilde{\mathcal{R}}_2^{(k)}$ is bounded as follows, with $C_{\varphi} = ||\partial \varphi||_{L^\infty(Q_T)}$:

$$\begin{aligned} |\tilde{\mathcal{R}}_2^{(k)}| &\leq \frac{1}{2} g C_{\varphi} \sum_{n=0}^{N_t-1} \Delta t \sum_{i=1}^{N_x} |(h_{i-1}^n)^2 - (h_i^n)^2| |\Delta x| |u_{i-\frac{1}{2}}^n| \\ &\leq 2C_{\varphi} ||h^{(k)}||_{k, BV_x} ||h^{(k)}||_{L^\infty(Q_T)} ||u^{(k)}||_{L^\infty(Q_T)} \Delta x^{(k)} \end{aligned}$$

where $|\tilde{\mathcal{R}}_2^{(k)}| \rightarrow 0$, as $k \rightarrow +\infty$, so we have

$$\lim_{k \rightarrow +\infty} \tilde{T}_2^{(k)} = \lim_{k \rightarrow +\infty} \tilde{\mathcal{T}}_2^{(k)} + 0.$$

Now we turn to $T_3^{(k)}$ and $\tilde{T}_3^{(k)}$. By a change in the notation of the time exponents,

APPENDIX B

using the fact that $\varphi_{i-\frac{1}{2}}$ vanishes at the last time step(s), we get:

$$T_3^{(k)} = \sum_{n=1}^{N_t-1} \Delta t \sum_{i \in \mathcal{E}_{int}} (\mathcal{H}_{i+1}^n - \mathcal{H}_i^n) u_{i+\frac{1}{2}}^n \varphi_{i+\frac{1}{2}}^n = \mathcal{T}_3^{(k)} + \mathcal{R}_3^{(k)}$$

with

$$\begin{aligned} \mathcal{T}_3^{(k)} &= \sum_{n=0}^{N_t-1} \Delta t \sum_{i \in \mathcal{E}_{int}} (\mathcal{H}_{i+1}^n - \mathcal{H}_i^n) u_{i+\frac{1}{2}}^n \varphi_{i+\frac{1}{2}}^{n+1}, \\ \mathcal{R}_3^{(k)} &= -\Delta t \sum_{i \in \mathcal{E}_{int}} (\mathcal{H}_{i+1}^0 - \mathcal{H}_i^0) u_{i+\frac{1}{2}}^0 \varphi_{i+\frac{1}{2}}^0 \\ &\quad + \sum_{n=0}^{N_t-1} \Delta t \sum_{i \in \mathcal{E}_{int}} (\mathcal{H}_{i+1}^n - \mathcal{H}_i^n) u_{i+\frac{1}{2}}^n (\varphi_{i+\frac{1}{2}}^n - \varphi_{i+\frac{1}{2}}^{n+1}), \end{aligned}$$

We have thanks to the regularity of φ :

$$|\mathcal{R}_3^{(k)}| \leq C_\varphi \Delta t^{(k)} \left[\|(u^{(k)})^0\|_{L^\infty(\Omega)} \|(\mathcal{H}^{(k)})^0\|_{BV(\Omega)} + \|u^{(k)}\|_{L^\infty(Q_T)} \|\mathcal{H}^{(k)}\|_{k, BV_x} \right]$$

Therefore, invoking the regularity of the initial conditions, this term tends to zero when $k \rightarrow +\infty$. We now have for the other terms, reordering the summations:

$$\begin{aligned} \tilde{T}_3^{(k)} + \mathcal{T}_3^{(k)} &= - \sum_{n=0}^{N_t-1} \Delta t \sum_{i \in \mathcal{M}} \mathcal{H}_i^n u_{i+\frac{1}{2}}^n (\varphi_{i+\frac{1}{2}}^{n+1} - \varphi_i^{n+1}) + \mathcal{H}_i^n u_{i-\frac{1}{2}}^n (\varphi_i^{n+1} - \varphi_{i-\frac{1}{2}}^{n+1}) \\ &= - \int_{Q_T} \mathcal{H}^{(k)} u^{(k)} \bar{\partial}_x \varphi_{\mathcal{M}, \mathcal{E}_{int}} \, dx dt \end{aligned}$$

Since $\bar{\partial}_x \varphi_{\mathcal{M}, \mathcal{E}_{int}}$ converges to $\partial_x \varphi$ in $L^p(Q_T)$ for any $p \geq 1$, we get:

$$\begin{aligned} \lim_{k \rightarrow +\infty} (\tilde{T}_3^{(k)} + \mathcal{T}_3^{(k)}) &= - \int_{Q_T} \bar{\mathcal{H}} \bar{u} \partial_x \varphi \, dx dt \\ &= - \int_{Q_T} \frac{1}{2} g \bar{h}^2 \bar{u} \partial_x \varphi \, dx dt \end{aligned}$$

Next we turn to $T_4^{(k)}$, we have

$$T_4^{(k)} = - \int_{Q_T} g \tilde{h}^{(k)} \tilde{u}^{(k)} \partial_x z^{(k)} \bar{\varphi}_{\mathcal{E}_{int}} \, dx dt,$$

APPENDIX B

and taking to the limit,

$$\lim_{k \rightarrow +\infty} T_4^{(k)} = - \int_{Q_T} ghu \partial_x z \varphi \, dx dt,$$

Finally, the remainder term $\tilde{\mathcal{R}}$ is non-negative under the CFL condition, while the positive part of \mathcal{R} tends to zero in $L^1(Q_T)$ under the Assumptions 5 and 6. The proof is thus complete. \square

Bibliography

BIBLIOGRAPHY

Bibliography

- [1] Akio Arakawa and Vivian R Lamb. “A potential enstrophy and energy conserving scheme for the shallow water equations”. In: *Monthly Weather Review* 109.1 (1981), pp. 18–36. DOI: [10.1175/1520-0493\(1981\)109<0018:APEAEC>2.0.CO;2](https://doi.org/10.1175/1520-0493(1981)109<0018:APEAEC>2.0.CO;2).
- [2] Emmanuel Audusse, Marie-Odile Bristeau, and Benoit Perthame. *Kinetic Schemes for Saint-Venant Equations with Source Terms on Unstructured Grids*. Rapport de recherche RR-3989. Projet M3N. INRIA, 2000. URL: <http://hal.inria.fr/inria-00072657>.
- [3] Emmanuel Audusse et al. “A fast and stable well-balanced scheme with hydrostatic reconstruction for shallow water flows”. In: *SIAM Journal on Scientific Computing* 25.6 (2004), pp. 2050–2065.
- [4] Emmanuel Audusse et al. “Sediment transport modelling: Relaxation schemes for Saint-Venant–Exner and three layer models”. In: *ESAIM: Proceedings*. Vol. 38. EDP Sciences. 2012, pp. 78–98. DOI: [10.1051/proc/201238005](https://doi.org/10.1051/proc/201238005).
- [5] Christophe Berthon et al. “An analytical solution of the Shallow Water system coupled to the Exner equation”. In: *Comptes Rendus Mathematique* 350.3 (2012), pp. 183–186. DOI: [10.1016/j.crma.2012.01.007](https://doi.org/10.1016/j.crma.2012.01.007).
- [6] Philippe Blanc, Robert Eymard, and Raphaèle Herbin. “A staggered finite volume scheme on general meshes for the generalized Stokes problem in two space dimensions”. In: *Int. J. Finite Volumes* 2.1 (2005).
- [7] François Bouchut. *Nonlinear Stability of Finite Volume Methods for Hyperbolic Conservation Laws: And Well-Balanced Schemes for Sources*. Frontiers in Mathematics. Birkhäuser Verlag, Basel, 2004.
- [8] François Bouchut, Julien Le Sommer, and Vladimir Zeitlin. “Frontal geostrophic adjustment and nonlinear wave phenomena in one-dimensional rotating shallow water. Part 2. High-resolution numerical simulations”. In: *Journal of Fluid Mechanics* 514 (2004), pp. 35–63.

BIBLIOGRAPHY

- [9] Zhixian Cao, Gareth Pender, and Jian Meng. “Explicit formulation of the Shields diagram for incipient motion of sediment”. In: *Journal of Hydraulic Engineering* 132.10 (2006), pp. 1097–1099. DOI: 10 . 1061 / (ASCE) 0733 - 9429(2006)132:10(1097).
- [10] Zhixian Cao et al. “Computational dam-break hydraulics over erodible sediment bed”. In: *Journal of hydraulic engineering* 130.7 (2004), pp. 689–703. DOI: 10 . 1061 / (ASCE)0733-9429(2004)130:7(689) .
- [11] Stéphane Cordier, Minh H Le, and T Morales de Luna. “Bedload transport in shallow water models: Why splitting (may) fail, how hyperbolicity (can) help”. In: *Advances in Water Resources* 34.8 (2011), pp. 980–989. DOI: 10 . 1016/j.advwatres.2011.05.002.
- [12] Vaughan Cornish and Harold Jeffreys. *Ocean waves and kindred geophysical phenomena*. CUP Archive, 1934.
- [13] Benoit Cushman-Roisin and Jean-Marie Beckers. *Introduction to geophysical fluid dynamics: physical and numerical aspects*. Vol. 101. Access Online via Elsevier, 2011.
- [14] Olivier Delestre. “Simulation du ruissellement d’eau de pluie sur des surfaces agricoles”. PhD thesis. Université d’Orléans, 2010.
- [15] Olivier Delestre et al. “SWASHES: a compilation of shallow water analytic solutions for hydraulic and environmental studies”. In: *International Journal for Numerical Methods in Fluids* 72.3 (2013), pp. 269–300.
- [16] David Doyen and Putu Harry Gunawan. “An Explicit Staggered Finite Volume Scheme for the Shallow Water Equations”. In: *Finite Volumes for Complex Applications VII-Methods and Theoretical Aspects*. Springer, 2014, pp. 227–235. DOI: 10 . 1007/978-3-319-05684-5_21.
- [17] Robert F Dressler. “Mathematical solution of the problem of roll-waves in inclined open channels”. In: *Communications on Pure and Applied Mathematics* 2.2-3 (1949), pp. 149–194.
- [18] Robert Eymard, Thierry Gallouët, and Raphaèle Herbin. “Finite volume methods”. In: *Handbook of numerical analysis* 7 (2000), pp. 713–1018.

BIBLIOGRAPHY

- [19] Robert Eymard and Raphaèle Herbin. “A staggered finite volume scheme on general meshes for the Navier-Stokes equations in two space dimensions”. In: *Int. J. Finite Volumes* 2.1 (2005).
- [20] Alexey V Fedorov and W Kendall Melville. “Kelvin fronts on the equatorial thermocline”. In: *Journal of physical oceanography* 30.7 (2000), pp. 1692–1705.
- [21] Luigi Fraccarollo and H Capart. “Riemann wave description of erosional dam-break flows”. In: *Journal of Fluid Mechanics* 461 (2002), pp. 183–228. doi: [10.1017/S0022112002008455](https://doi.org/10.1017/S0022112002008455).
- [22] Thierry Gallouët, Jean-Marc Hérard, and Nicolas Seguin. “Some approximate Godunov schemes to compute shallow-water equations with topography”. In: *Computers & Fluids* 32.4 (2003), pp. 479–513.
- [23] Jean-Frédéric Gerbeau, Benoît Perthame, et al. “Derivation of viscous Saint-Venant system for laminar shallow water; numerical validation”. In: *Research Report/ RR-4084* (2000).
- [24] Anthony J Grass. *Sediment transport by waves and currents*. University College, London, Dept. of Civil Engineering, 1981.
- [25] Raphaèle Herbin, Walid Kheriji, and Jean-Claude Latché. “On some implicit and semi-implicit staggered schemes for the shallow water and Euler equations”. In: *ESAIM: Mathematical Modelling and Numerical Analysis* eFirst (Apr. 2014), pp. 1290–3841.
- [26] Raphaèle Herbin, J C Latché, and Trung Tan Nguyen. “Explicit staggered schemes for the compressible euler equations”. In: *ESAIM: Proceedings*. Vol. 40. EDP Sciences. 2013, pp. 83–102. doi: [10.1051/proc/201340006](https://doi.org/10.1051/proc/201340006).
- [27] Antonio Huerta and Wing Kam Liu. “Viscous flow with large free surface motion”. In: *Computer Methods in Applied Mechanics and Engineering* 69.3 (1988), pp. 277–324.
- [28] Jochen Kampf. *Ocean Modelling for Beginners: Using Open-source Software*. Springer, 2009.
- [29] Stephan C Kramer and Guus S Stelling. “A conservative unstructured scheme for rapidly varied flows”. In: *International journal for numerical methods in fluids* 58.2 (2008), pp. 183–212.

BIBLIOGRAPHY

- [30] Randall J LeVeque. *Finite volume methods for hyperbolic problems*. Vol. 31. Cambridge university press, 2002.
- [31] Eugen Meyer-Peter and R Müller. “Formulas for bed-load transport”. In: *Proceedings of the 2nd Meeting of the International Association for Hydraulic Structures Research*. International Association of Hydraulic Research Delft. 1948, pp. 39–64.
- [32] Trung Tan Nguyen. “Explicit staggered numerical schemes for compressible flows”. PhD thesis. Université d’Aix-Marseille, 2013.
- [33] Benoît Perthame and Chiara Simeoni. “A kinetic scheme for the Saint-Venant system with a source term”. In: *Calcolo* 38.4 (2001), pp. 201–231.
- [34] Sri Redjeki Pudjaprasetya and Ikha Magdalena. “Momentum Conservative Scheme for Shallow Water Flows”. In: *East Asian Journal on Applied Mathematics (EAJAM)* 4.2 (2014), pp. 152–165.
- [35] Sri Redjeki Pudjaprasetya and Ikha Magdalena. “Wave Energy Dissipation in Porous Media, Applied Mathematical Sciences”. In: *Applied Mathematical Sciences* 7.59 (2013), pp. 2925–2937.
- [36] Yin-Tik Que and Kun Xu. “The numerical study of roll-waves in inclined open channels and solitary wave run-up”. In: *International journal for numerical methods in fluids* 50.9 (2006), pp. 1003–1027.
- [37] GL Richard and Sergey L Gavrilyuk. “A new model of roll waves: comparison with Brock’s experiments”. In: *Journal of Fluid Mechanics* 698 (2012), pp. 374–405.
- [38] GL Richard and Sergey L Gavrilyuk. “The classical hydraulic jump in a model of shear shallow-water flows”. In: *Journal of Fluid Mechanics* 725 (2013), pp. 492–521.
- [39] Leo C van Rijn. “Sediment transport, Part II: Suspended load transport”. In: *Journal of Hydraulic Engineering* 110.11 (1984), pp. 1613–1641. DOI: 10.1061/(ASCE)0733-9429(1984)110:11(1613).
- [40] Guy Simpson and Sébastien Castelltort. “Coupled model of surface water flow, sediment transport and morphological evolution”. In: *Computers & Geosciences* 32.10 (2006), pp. 1600–1614. DOI: 10.1016/j.cageo.2006.02.020.

BIBLIOGRAPHY

- [41] Guss S Stelling and S P Alex Duinmeijer. “A staggered conservative scheme for every Froude number in rapidly varied shallow water flows”. In: *International Journal for Numerical Methods in Fluids* 43.12 (2003), pp. 1329–1354.
- [42] Guus S Stelling and Marcel Zijlema. “An accurate and efficient finite-difference algorithm for non-hydrostatic free-surface flow with application to wave propagation”. In: *International Journal for Numerical Methods in Fluids* 43.1 (2003), pp. 1–23.
- [43] Costas Emmanuel Synolakis. “The runup of solitary waves”. In: *Journal of Fluid Mechanics* 185 (1987), pp. 523–545.
- [44] William Carlisle Thacker. “Some exact solutions to the nonlinear shallow-water wave equations”. In: *Journal of Fluid Mechanics* 107 (1981), pp. 499–508.
- [45] Eleuterio F Toro. *Riemann solvers and numerical methods for fluid dynamics: a practical introduction*. Springer, 2009.
- [46] Fjordholm Ulrik Skre. “Structure preserving finite volume methods for the shallow water equations”. MA thesis. Denmark: University of Oslo, 2009.
- [47] Leo C Van Rijn. “Sediment transport, part I: bed load transport”. In: *Journal of hydraulic engineering* 110.10 (1984), pp. 1431–1456. DOI: [10.1061/\(ASCE\)0733-9429\(1984\)110:10\(1431\)](https://doi.org/10.1061/(ASCE)0733-9429(1984)110:10(1431)).
- [48] Cornelis Boudewijn Vreugdenhil. *Numerical methods for shallow-water flow*. Vol. 13. Springer, 1994.
- [49] Bas Wols. “Undular hydraulic jumps”. MA thesis. Netherlands: Delft University of Technology, Faculty of Civil Engineering and Geosciences, Section of Environmental Fluid Mechanics, 2005.
- [50] Weiming Wu and Sam S Wang. “One-dimensional modeling of dam-break flow over movable beds”. In: *Journal of hydraulic engineering* 133.1 (2007), pp. 48–58. DOI: [10.1061/\(ASCE\)0733-9429\(2007\)133:1\(48\)](https://doi.org/10.1061/(ASCE)0733-9429(2007)133:1(48)).
- [51] Vladimir Zeitlin. *Nonlinear Dynamics of Rotating Shallow Water: Methods and Advances: Methods and Advances*. Vol. 2. Elsevier, 2007.

BIBLIOGRAPHY
